UNIVERSITY OF
LIVERPOOL

Proton Induced Quasi-free Scattering with Inverse Kinematics

Thesis submitted in accordance with the requirements of the University of Liverpool for the degree of Doctor in Philosophy

by

Jonathan T. Taylor

Oliver Lodge Laboratory

September 2011

"But how can the characters in a play guess the plot? We are not the playwright, we are not the producer, we are not even the audience. We are on the stage. To play well the scenes in which we are 'on' concerns us much more than to guess about the scenes that follow it."

— C. S. Lewis, The World's Last Night (1952)

"When the perishable has been clothed with the imperishable, and the mortal with immortality, then the saying that is written will come true: 'Death has been swallowed up in victory.' "

— St. Paul, First letter to the Corinthians (c. 53 AD)

Acknowledgements

I'd like to use the next few paragraphs to say thank you and to dedicate this work to the people who have helped to make it possible. Listed below are not just those who contributed to the work itself but also those who supported me as I endeavoured to complete it.

First of all I would like to thank my supervisors Marielle Chartier and Roy Lemmon for introducing me to this field of research and giving me the opportunity to do this work, and also for their help understanding the physics that lay behind it all. Thank you for the feedback you gave me on the drafts of this thesis that helped me to make it a much more presentable document and also for your support in my job applications, all of this is much appreciated.

Thank you to Marc Labiche for help understanding the physics during the long Tuesday morning videoconferences and particularly for help understanding the GEANT4 simulation work and the proofreading of that chapter in this thesis.

Thank you to the Nuclear Structure group at Liverpool, the staff for their teaching and the students for lots of good nights out in Liverpool and Scotland! I'm grateful to the students who didn't laugh too hard that time when I walked into a lamppost in Glasgow - after all, these things happen to the best of us ☺

Thank you to Philippos Papadakis for his company, interesting conversation and good sense of humour as well as his unwavering commitment to the conversion electron. Your dedication is an example to all of us! Thanks also to Pete Wu for being a lively and entertaining office colleague and for having such a comical and contagious laugh!

Thank you to Janet Sampson for proofreading and help typesetting this thesis, it looked a lot better afterwards. Thanks also to Lola from Santiago for proofreading the results and simulation chapters and for the useful feedback you gave me.

I should also thank Mark Zuckerberg, the founder of facebook for providing me with an endless (and much needed) source of procrastination.. and also Jed Bartlet & the cast of the West Wing. Another welcome source of distraction especially during those late evenings and weekends in the office when I really needed a break. I learnt lots about American politics and have followed it with a keen interest ever since.

Abstract

Quasi-free scattering reactions represent a direct way to learn about the properties of a nucleon inside the atomic nucleus. In such a nuclear reaction, a high energy particle knocks a bound nucleon directly out of a nucleus without any further violent interaction between the nucleus and the incident, or the nucleus and the two outgoing particles. Quasi-free scattering reactions are thus an ideal way to study the single-particle structure of nuclei and also how the nucleon-nucleon interaction is modified inside nuclear matter. With the availability of high-energy radioactive ion beams, it is now possible for the first time, to use quasi-free scattering reactions to study how such properties are modified inside isospin asymmetric nuclei and nuclear matter. In a recent pilot experiment at the GSI laboratory in Germany, proton induced quasi-free scattering was performed using the LAND/R^{3}B setup in Cave C. This kinematically complete setup is acting as a prototype for the future full R^{3}B (Reactions with Relativistic Radioactive Beams) experiment and is based on an array of Si micro-strip detectors for tracking, and thick NaI scintillators for energy measurements. This allows for the detection of light recoil particles in coincidence with the detection of both charged particles, neutron and γ rays such that quasi-free reactions of the type $(p, 2p)$,(p, pn) and $(p, p\alpha)$ can be observed. The benchmark experiment was carried out using inverse kinematics with a ^{12}C beam, at 400 A.MeV and since the structure of ^{12}C is well known, and has been investigated with proton as well as electron knockout reactions, comparisons can be made with these measurements. This thesis will report on the results that have been achieved for the population of both bound and unbound states using the proton induced quasi-free reaction: ^{12}C$(p, 2p)X$ as well as describing how the experimental setup is to be extended for future experiments with higher energy radioactive ion beams at the FAIR facility.

Contents

List of Figures

List of Tables

Chapter 1

Introduction

One hundred years ago Ernest Rutherford discovered the atomic nucleus [1]; an event that marked the birth of the field of Nuclear Physics. Over the last century, the atomic nucleus has proved to be a fascinating field for scientific research displaying a rich variety of quantum phenomena. Many of the features exhibited by nucleons within the nucleus have a striking similarity to the structure and behaviour of atomic electrons in the atom, and thus similar descriptions for energy levels and shells, spins and angular momentum have emerged. However, when describing the forces and potentials experienced by the nucleons within the nucleus, there are some marked differences. Firstly, the dominating force inside the nucleus is the strong force rather than the electromagnetic one. Secondly, since the strong force is short range and attractive, the potential in which the nucleons exist is created by all the other nucleons in contrast to the force between the atomic electrons and the spatially separated positive charge of the nucleus. The liquid-drop model was proposed by Bethe and Bacher in 1936 [2] as a means of understanding nuclear structure. In this model, nucleons were strongly interacting particles that make up the nucleus, which in turn was considered to be a like a drop of charged incompressible nuclear liquid. However early research into nuclear ground state properties such as masses, magnetic moments, spins and parities, led to the conclusion that certain combinations of protons and neutrons formed more tightly bound nuclei than others [3, 4], a conclusion that could not be explained by the liquid drop model. The numbers of protons or neutrons that form these optimal combinations are: 2, 8, 20, 28, 50, 82, 126 and they became known as the 'magic numbers', with nuclei that possessed magic numbers of both protons and neutrons known as doubly magic. In this way, nuclei can be thought of as having shell structure analogous to the atomic energy levels that had already been observed for electrons. When a shell contains a magic number of protons or neutrons it is said to be closed and the separation energy for removing a nucleon from this closed shell is larger than if the shell were not closed. In the shell model [3, 4], the nucleon-nucleon potential created by the strong

force can be thought of as creating a mean field in which each nucleon of the nucleus moves independently experiencing a potential created by all the other nucleons. This mean field is a central potential that can be modelled using a simple harmonic oscillator (SHO) potential with some modifications [5].

Several factors emerge when a nucleon is described as moving within the SHO potential. Firstly, because each nucleon is confined in space it will always have a minimum energy given by the uncertainty principle and known as the zero-point energy. Secondly, because the nucleons are described by a wave function confined within the boundaries of the potential, the energy states that it can occupy become quantised. Energy levels become degenerate due to the different possible values of n and ℓ (the quantum numbers describing energy and angular momentum respectively). Adding an additional ℓ^2 term to the SHO potential creates a more attractive potential at larger radii where the nucleons are further from the centre of the nucleus and have the greatest angular momentum. This has the effect of flattening out the SHO potential making it similar to the more commonly used Woods-Saxon potential [6].

When the coupling between the angular momentum of a nucleon and its spin is taken into account, the force felt by the nucleon is dependent on the orientation of its spin relative to the angular momentum, an effect known as the spin-orbit coupling. The addition of a spin-orbit term to the Woods-Saxon or modified SHO potential allows a realistic shell-model potential to be achieved which is capable of reproducing all of the magic numbers. Nucleons fill the shells of the nucleus according to the Pauli principle which limits the number of available spaces for nucleons according to their quantum numbers. Since the placing of a nucleon into the next shell will result in it being in a less bound orbit, it follows that the separation energy of the nucleon is seen to drop immediately after a closed shell [5]. This model describes well the nuclei at closed shells around the valley of stability. For stable nuclei that are between closed shells, corrections can be applied that treat the additional nucleons outside the closed shell as valence configurations. Residual interactions that account for additional forces, and correlations between nuclei that are left out of the mean field approach can also be applied. Far from stability, exotic nuclei at the extremes of mass, isospin and angular momentum display a structure that is modified beyond the mean field picture that the shell model gives. This changing structure is depicted alongside the structure for stable nuclei in Fig. 1.1.

1.1   Exotic Nuclei

As nuclei become more neutron-rich, the nuclear surface becomes more diffuse and the nuclear density decreases. This generates phenomena such as neutron halos and

h$_{9/2}$
f$_{5/2}$
p$_{1/2}$
p$_{3/2}$
f$_{7/2}$
h$_{11/2}$

g$_{7/2}$
d$_{3/2}$
s$_{1/2}$
d$_{5/2}$

g$_{9/2}$

N=5

N=4

3p
2f

1h

3s
2d

1g

126

82

50

p$_{1/2}$
f$_{5/2}$
i$_{11/2}$
p$_{3/2}$
h$_{9/2}$
f$_{7/2}$

d$_{3/2}$
h$_{11/2}$
s$_{1/2}$
g$_{7/2}$
d$_{5/2}$

g$_{9/2}$

very diffuse
surface
neutron drip line

harmonic
oscillator

no spin
orbit
exotic nuclei/
hypernuclei

around the
valley of
β-stability
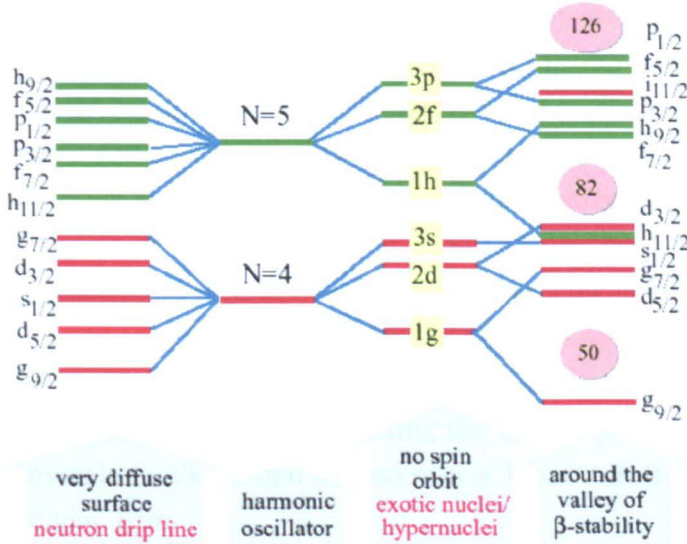
Figure 1.1: Schematic of single-particle levels for nuclei are shown for various potentials representing both stability and the drip line. Orbitals are labelled using their spherical quantum numbers. Magic numbers indicated on the right side of the figure representing the nuclear potential at stability, disappear as the neutron drip line is approached (see left of the figure) and the nuclear surface becomes more diffuse. Figure modified from [7].

skins where the neutron matter in a nucleus can separate itself spatially from a core of remaining nuclear matter. In the case of nuclear halos, this can increase the interaction radius of the nucleus to a value many times larger than is typical for its mass (see Eqn. 2.1). Neutron skins represent a form of nuclear matter expected to exist only in neutron stars. In the laboratory, they can be observed in scattering experiments to determine nuclear radii, or by the collective excitation known as the 'Pygmy Dipole Resonance' in which a neutron skin oscillates against an isospin saturated core. Attempts to measure the neutron skin thickness for very neutron rich nuclei have taken place using both these methods at the GSI laboratory and are reported on here [8–10]. Neutron skins can also been seen in elastic scattering experiments. In addition, the magic numbers observed and predicted by the shell model for stable nuclei can become quenched and in some cases new ones can appear. This has been the case with the neutron shells $N = 8, 20$ for stable nuclei, which disappear for very neutron rich nuclei and are replaced with $N = 6, 16$ shells [11]. This shell quenching is predicted for neutron numbers all the way up to the $N = 82$ shell closure, while for protons it appears to stop much sooner ($Z = 28$). This is because the Coulomb force prevents the descent of higher energy orbitals from the continuum approaching the bound states [12], a process that is often linked to shell quenching. Observation of $N = 82$ shell quenching, would shed light on the astrophysical r-process by allowing a better fit of the data we have for element

abundances [13]. Elements of the nucleon-nucleon interaction and correlations between nucleons are thought to be responsible for this quenching, an example being the tensor force in which the occupancy of specific proton and neutron orbitals can be expected to significantly alter their energy [11,14]. Investigation of these effects has been carried out for exotic nuclei using the transfer reaction method (discussed further in the next chapter), and confirmation of changing shell structure has been confirmed [15]. Some of the experimental methods and results that confirmed changing shell gaps and nuclear halo states are discussed in the next chapter. The quest to obtain a model that will adequately describe the nucleus in all areas of stability, as well as at the extremes of nuclear existence is one that has been motivating the last 50 years of nuclear physics and is playing a key role in the design of major new laboratories such as the FAIR facility to which we now turn.

1.2 The FAIR Facility

In the next few years, a new international accelerator known as the Facility for Anti-proton and Ion Research (FAIR), will be built at the GSI[1] laboratory in Germany. At FAIR, an enormous variety of experiments will be possible allowing physicists from all around the world to gain new insights into the structure of matter and the evolution of the universe from the Big Bang to the present [16]. The FAIR accelerator complex will deliver beams of anti-protons and ions with unprecedented intensity and quality using new linear accelerators and synchrotrons. When the final stages of construction are complete, FAIR will consist of eight ring colliders with a circumference of up to 1,100 meters, two linear accelerators, and about 3.5 kilometers of beam control tubes. The existing linear accelerator and synchrotron at GSI will be redirected and used as injectors for the new FAIR complex [17]. The areas of physics open to exploration by FAIR can be summarised under the following headings:

- Nuclear structure far from stability and its relevance to astrophysical processes

- Hadron spectroscopy and hadronic matter

- Compressed nuclear matter

- High energy density in bulk matter

- Quantum electrodynamics, strong fields and ion-matter interactions

The ion beams available will range from hydrogen to uranium where the highest possible energies will be close to 35 GeV.A for a beam of fully stripped uranium ions,

---

[1] Gesellschaft für Schwerionenforschung

delivered at an intensity close to 1.5×10^{10} ions per spill. Greater intensities of up to 3×10^{11} ions/s will be available by lowering the beam energy to 1 GeV.A [18].

In order to address the areas of physics outlined above, FAIR is split into four different experimental collaborations. One of these experimental collaborations is the group of experiments collectively known as the: Nuclear Structure, Astrophysics and Reactions (NuSTAR) collaboration. This collaboration will focus on the first topic outlined above by studying short-lived radioactive beams from stability all the way up to and in some cases, beyond the drip lines. This will allow scientists to examine how nuclear models apply at the extremes of isospin, whilst also enabling direct studies of the nuclei that are involved in the processes of energy production and element synthesis in stellar environments, in particular the r-process [19]. In order to make these short-lived nuclei at the highest possible intensities (for the in-flight method), it is necessary to have very high energy primary beams and a good transport efficiency especially for the heavier ions such as uranium that are often used for the production of the secondary beams. The new fragment separator for FAIR known as the Super-FRS will replace the current one, giving a much greater transport efficiency, and delivering secondary radioactive beams with an intensity that is increased by more than three orders of magnitude in comparison to the current FRS at GSI [20].

At the high energy branch of NuSTAR will be the R^3B (Reactions with Radioactive Relativistic Beams) setup. This setup is being designed to take full advantage of the high transmission rate, operating with the high energy and high intensity beams that will be delivered straight from the Super-FRS. This has several advantages, firstly measurements can be made using thick targets of the order of g/cm^2. Secondly nuclear reactions will generate strongly forward-focused reaction products. This will make full acceptance measurements possible using reasonably sized detectors which in turn makes investigation of very exotic nuclei with very low production rates still feasible. Thirdly, it allows approximations to be applied that make the separation of structural information and a quantitative description of the reaction mechanism a great deal easier [20, 21]. The detectors employed in the R^3B setup will be a substantial upgrade to an existing prototype setup previously known as the LAND or LAND/ALADIN setup but now increasingly called the LAND/R^3B setup as it is gradually upgraded to be more like the future R^3B setup.

One of the main experimental probes of exotic nuclei at R^3B is the quasi-free scattering reaction, a summary of which is given in the next chapter. This reaction will allow single-particle properties and in-medium effects such as the nucleon-nucleon interaction inside nuclear matter to be investigated systematically. The first stage of this programme will make use of quasi-free scattering processes such as $(p, 2p)$ and (p, pn) to explore the single-particle properties and shell structure up to, and beyond,

the drip line for medium mass isotopic chains. This will allow systematic measurements of nuclear structure variables to be made as a function of changing isospin and nuclear density. Further to this, quasi-free processes such as $(p, 3p)$ or $(p, 2pn)$ could be used to investigate the nucleon-nucleon interaction within nuclear matter. Close to the neutron drip line, many nuclei are predicted to exhibit cluster structures as a means of dealing with their excess neutrons and optimising their binding energy. This cluster structure could be investigated with the aid of quasi-free scattering reactions such as $(p, p\alpha)$ [22].

At a later stage in the programme, polarised quasi-free scattering is proposed in order to measure single-particle properties and shell structure as a function of spin as well as isospin. Previous work has indicated a relationship between cross sections measured in polarised quasi-free scattering experiments and the nucleon-nucleon correlations [22]. This is technically challenging since it will require the development of a polarised hydrogen target. In addition to this, the polarised target will lower the quasi-free scattering cross section significantly, however the high beam intensities at FAIR are hoped to counter this problem.

1.3   Author's Contribution and Thesis Overview

This thesis will concentrate on an experiment that was performed using the current prototype LAND/R^{3}B setup with a stable beam of ^{12}C. The aim of this experiment was to obtain a benchmark data set that would allow a better understanding of the quasi-free scattering reactions and the ability of the current detectors to observe and reconstruct them. This information is important for future experiments with lower intensity radioactive beams and the information and results from the analysis reported on here can be used to inform the design and optimisation of future detectors, as well as the analysis procedures required for when the future full R^{3}B setup comes online at the FAIR facility.

In an experiment of this magnitude, it is not possible for one person to carry out all of the work that is necessary to produce the relevant results. It is therefore appropriate to outline the main contributions of the author of this thesis to the calibration and analysis work that has taken place as well as to acknowledge the contribution of colleagues with whom the author has worked closely. The author would like to extend special thanks to fellow students: Valerii Panin and Felix Wamers for the work that they carried out in parallel with his (on the experiment reported here and another similar experiment [23]), as well as their comments and appraisal of his own work. In terms of calibration, initially the author focused mainly on the tracking of the beam onto the target where it was found that a successful calibration of the beam tracking detectors was not possible due to the low energy loss of the ^{12}C ions in these detectors (see section 3.2.2). Next, the

author began to focus on the scintillator-based detectors or time-of-flight walls that are positioned after the target and magnetic spectrometer (see sections 3.4.1, 3.4.2 and 3.4.3). A good calibration of these detectors was necessary in order to extract the charge, mass and momentum of particles produced in nuclear reactions with the target, and in order to get the best possible selection of the relevant reaction channels. Alongside this work the author helped develop other tools and techniques related to the tracking of particles which make use of the time-of-flight walls along with other detectors in order to extract the mass momentum and/or mass of reaction products after they had passed through the magnetic spectrometer (see section 4.5.2). A first attempt at observing the angular correlations of scattered nucleons seen in previous work for this experiment was carried out with Valerii Panin who went on, with Felix Wamers to develop and refine the algorithm, improving the resolution and event selection a great deal. The author also developed a realistic event generator and carried out supplementary work on the geometry of the GEANT4 simulations and subsequent event construction for the analysis with experimental algorithms. The simulated data were passed through the algorithms developed by co-workers and analysed by Valerii Panin in order to determine the response of the detectors surrounding the target to the reactions of interest (see chapter 6). Additionally, the author also focused on the application of a background subtraction method (first used by Felix Wamers) to the data set from the experiment detailed in this thesis in order to obtain accurate cross section measurements with both carbon and hydrogen targets. Finally, the author has made use of the invariant-mass method in order to reconstruct the excitation of unbound systems that undergo two-body decay (see chapter 5).

Chapter 2

Direct Reactions as Spectroscopic Tools

The first direct nuclear reactions were observed at the Liverpool Cyclotron in the 1940s when proton and deuteron beams were used to carry out nuclear breakup and elastic scattering experiments on light gaseous targets [24–26]. Since then, direct reactions have been developed both theoretically and experimentally, and have proved to be a powerful tool for probing the single-particle components of the nuclear wave function. This is due to their ability to excite a minimal number of nucleonic degrees of freedom allowing precise measurements of quantities like single-particle orbitals, their excitation energy and their occupation probabilities [27,28]. In the past, direct reactions such as nucleon transfer and quasi-free scattering reactions (mainly of the type $(p, 2p)$ using proton beams, and $(e, e'p)$ using electron beams) were used to examine stable nuclei in normal kinematics.

More recently however, transfer reations have been applied to radioactive beams alongside newer reaction mechanisms such as one-nucleon knockout[1] and Coulomb breakup [30]. These reactions using radioactive beams all take place using inverse kinematics where for obvious reasons the nucleus of interest becomes the beam rather than the target. Data from transfer, knockout and quasi-free scattering reactions are presented in Fig. 2.1 where the expected cross sections deduced from experiments are compared to the theoretical ones predicted from the shell model. Their ratio (R_s) is plotted as a function of the difference between the separation energies of the deficient and excess nucleons in that system (ΔS). The value of ΔS takes on large negative values for reactions where a weakly bound nucleon of the excess species is removed and large positive values for reactions that remove a strongly bound nucleon of the

---

[1]The term 'knockout' is used throughout this thesis to refer to nucleon removal reactions carried out with a light target such as carbon or beryllium.
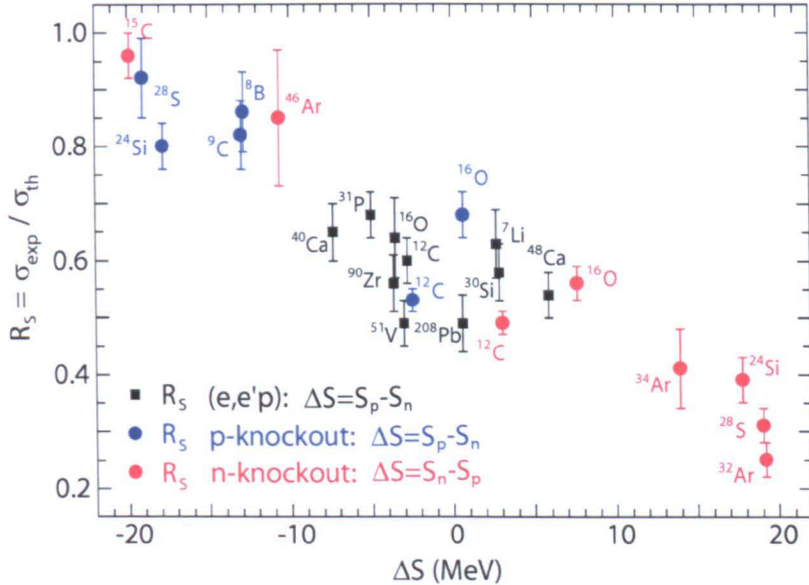
Figure 2.1: Spectroscopic strength as a function of separation energy difference. The reduction of the measured nucleon removal cross sections relative to their theoretical values (Spectroscopic strength, R_s) is plotted as a function of the difference between the neutron and proton separation energies (ΔS). Data points for stable and exotic nuclei are shown. Figure taken from [29]

deficient species. For stable nuclei, $\Delta S \sim 0$ and $R_s \sim$ 0.5-0.7, with agreement between the knockout and quasi-free reactions used to obtain the data. Cross sections that differ most from shell model predictions are seen for the large positive values of ΔS when a nucleon of the deficient species is removed giving $R_s \sim$ 0.25-0.4, and the best agreement with shell model cross sections is seen when nucleons are removed from the excess species yielding $R_s \sim$ 0.8-1.0. The suggested cause of these reduced cross sections in comparison to the shell model are nucleon-nucleon correlation effects that are not accounted for by the shell model. These correlation effects seem to be enhanced for strongly bound valence nucleons of the deficient type and weakened for loosely bound valence nucleons of the excess type [29]. This chapter will discuss the limitations and strengths of various reactions to probe both the nuclear structure that reveals this discrepancy with the shell model, as well as the nucleon-nucleon correlations that are suggested to be the cause.

2.1 Transfer Reactions

Single-particle properties in stable nuclei have been studied extensively using transfer reactions. The two most common forms of transfer reaction are the so called one nucleon 'stripping' and 'pickup' reactions of the type: $^AX(d,p)^{A+1}X$ and $^AX(p,d)^{A-1}X$

respectively, although cluster transfer reactions using t and α-particles for example, have also been carried out. Data extracted from transfer reaction experiments have typically been interpreted using Distorted Wave Born Approximation (DWBA) models, where two-body descriptions for both the entrance and exit channels are used and potentials are created from stable nuclei within certain mass and energy regions [31]. These models have also been extended to include the effect of the breakup of the deuteron after a transfer reaction [32, 33] and have recently been adapted to describe transfer reactions with halo nuclei [34]. Using the DWBA models, ℓ-values can be deduced from the measured angular distributions of the transferred nucleon allowing single-particle configurations to be determined (see Fig. 2.2). Partial cross sections to given states allow spectroscopic factors to be deduced as a measure of the overlap between the initial and final state many-body wave functions. This in turn can lead to information about the single-particle occupancies in the nuclear wave function [27]. Due to the high sensitivity of transfer reactions to the single-particle components in the nuclear wave function, the momentum transfer of the beam must be precisely matched to the momentum of the valence nucleons in the nuclear surface. Thus the ideal energy range for beams used in transfer reactions is $\sim$10$-$20 MeV.A which corresponds to a momentum transfer of $\sim$100$-$200 MeV/c [30]. For transfer reactions to be applied to short-lived radioactive nuclei, the reaction must take place using inverse kinematics with beam energies in the above energy range impinging on light targets. Experimental challenges arise from a number of factors. Firstly, very thin targets are needed to obtain good energy resolution, and hence high beam intensities ($\sim$10^4 s^{-1}) must be achieved in order to collect enough events in a reasonable amount of time. Secondly, detectors with high enough acceptance and energy resolution are required to accurately reconstruct the transfer reactions that have taken place. This is particularly important for stripping reactions where the ejectiles can appear at backwards angles in the laboratory frame [35].

Results from transfer experiments on radioactive nuclei have been reported for a number of years, with both light and heavier nuclei. The transfer reaction ^{56}Ni$(d,p)^{57}$Ni reported in ref. [37] was carried out at the Argonne National Laboratory (ANL) in Chicago, USA using inverse kinematics with an average beam intensity of 2.5$\times$10^4 s^{-1} impinging on a target of 500μg/cm^2 CD$_2$. In order to detect the protons emerging at backwards angles from the target, a large silicon detector array was used and unwanted background reactions were eliminated by measuring the mass and charge of the forward emitted reaction products. More recently, new detectors such as the Transfer and Inelastic All-angles Reaction Array (TIARA) [38] at the GANIL laboratory in Caen, France and the HELIcal Orbit Spectrometer (HELIOS) [39] at ANL, have been developed and commissioned and new experimental setups designed (Fig.2.3) to cope with the aforementioned experimental challenges. Results have been obtained
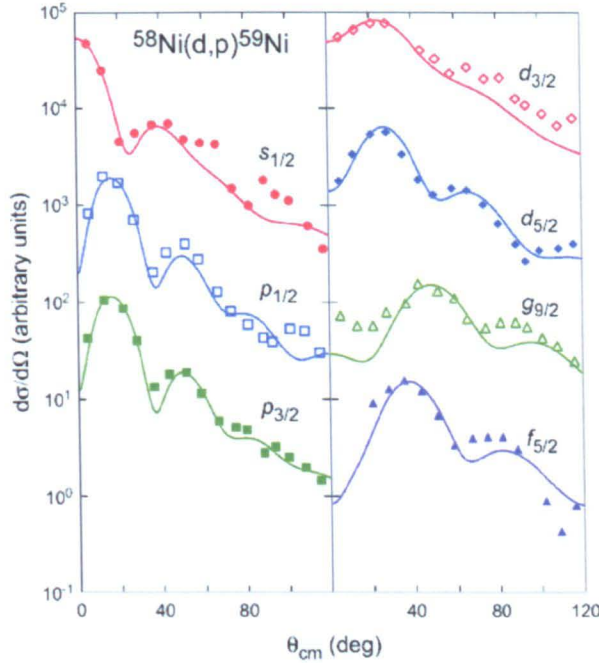
Figure 2.2: The angular distribution of protons after the transfer reaction ^{58}Ni$(d, p)^{59}$Ni selected states are shown which have been fitted using calculations from the DWBA model. Figure taken from [28], modified from [36].

at the GANIL laboratory for the ^{24}Ne$(d, p)^{25}$Ne transfer reaction with the TIARA array [40] where it was possible to make tentative spin assignments of the populated states by combining γ-ray detection with the angular distribution of the ejectiles. Transfer reactions approaching the neutron drip line have been carried out successfully for ^{21}O [41] and also for lighter systems such as the possible halo nucleus ^{12}Be [42] and even the unbound nucleus ^{7}He [43].

In the near future, one particular area that could be investigated with the aid of transfer reactions in inverse kinematics is the Z = 28 nickel isotopic chain. Calculations aimed at studying the role of the tensor force in exotic nuclei predict a descent of proton intruder states between ^{68}Ni and ^{78}Ni [14]. In the next few years it is likely that transfer reactions will build upon the work discussed above for ^{56}Ni$(d, p)^{57}$Ni and shown for ^{58}Ni$(d, p)^{59}$Ni in Fig.2.2 so that heavier isotopes of nickel can be investigated out to the neutron drip line. Neutron transfer reactions at the $N = 50$ shell closure have already been completed for other nuclei such as ^{82}Ge [44], and a clear signature of magicity obtained for the exotic neutron-rich nucleus ^{132}Sn [45].
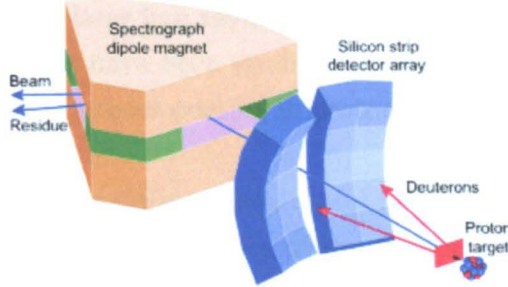
Figure 2.3: Schematic of a proposed experimental setup for observing 'pickup' transfer reactions using inverse kinematics at the upgraded NSCL facility in Michigan State University (MSU). Rare isotope beams impinge upon a proton target after which deuterons are collected in a silicon array at forward angles and fragments from the reaction are detected with a magnetic spectrometer. Figure taken from [28].

2.2 Knockout Reactions

Knockout reactions are complementary to the transfer stripping reaction since they involve the removal of a nucleon rather than its addition, and thus probe the 'hole'-structure of nuclei rather than the particle-structure. Ever since the first production and identification of radioactive relativistic beams occurred over thirty years ago, knockout reactions have played a large part in their study. These first experiments were carried out at the Bevalac accelerator in Berkeley by fragmentation of the primary beams ^{40}Ar and ^{48}Ca and were concerned with the production of new neutron-rich isotopes and their associated production cross sections [46,47]. This emergence of fast radioactive beams from the fragmentation of heavier ions then became of major importance to the field of nuclear physics because of its ability to be a systematic tool for the study of unstable nuclei. Further study at Berkeley revealed that when radioactive neutron-rich beams of ∼800 MeV.A were produced, and the interaction cross sections of light isotopes of lithium and beryllium were measured, they exhibited a much larger radii than was predicted for stable nuclei via the empirical relation:

$$R = r_0 A^{1/3} \tag{2.1}$$

where R is the radius of the nucleus, A the atomic mass number and r_0 ∼1.2 fm. In this equation, the constant r_0 arises because the number of nucleons per unit volume is roughly constant and independent of the mass [48]. It was found that the strong deviation from this relation was due to a phenomenon known as the nuclear 'halo' where a core of protons and neutrons can appear to be separated from other neutron matter that surrounds it in a halo like structure. Reviews of the work that led to the discovery at Berkeley can be found in refs. [49,50], however the term 'halo' was not applied to

these nuclei until a couple of years later in a review article on neutron-rich nuclei [51]. Since then, many more halo nuclei have been studied and predicted both for larger masses and halo sizes, with some examples existing in proton-rich nuclei although these halos are usually less pronounced [52].

Single nucleon knockout reactions have also proven useful for other structure investigations in nuclei such as, observing the breakdown of the $N = 8$ shell gap e.g. in the neutron-rich ^{12}Be [53] along with other investigations into the breakdown of known shell gaps and the emergence of new ones in the so called 'island of inversion' [54]. A schematic of such a reaction is shown in Fig. 2.4.
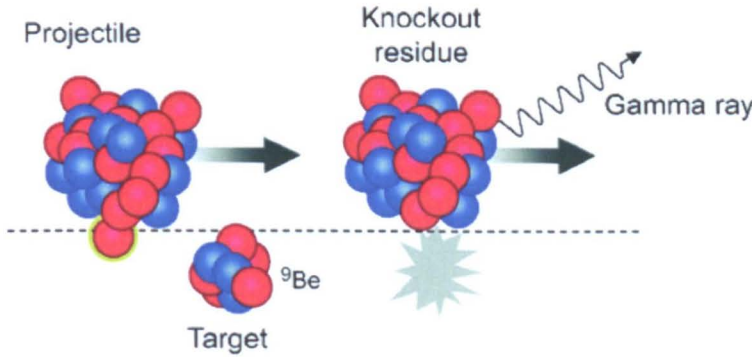
Figure 2.4: Schematic showing a knockout reaction occurring via the stripping process. Figure taken from [28].

The ability of nucleon knockout reactions to investigate the nuclear structure phenomena discussed is contingent on various approximations that must be made in order for the observables of an experiment to yield reliable physical quantities. The first approximation is known as the 'sudden' or adiabatic approximation and it entails that the nuclear reaction occurs at a much greater speed than the internal motion of the nucleons so that they can be considered 'frozen' when a reaction takes place [32, 55]. This approximation allows the momentum of the residual fragment or core in a knockout reaction to be treated as equal and opposite to the momentum of the knocked out nucleon in the rest frame of the projectile. Thus, the momentum distribution of the core can give a direct measurement of the wavefunction of the removed nucleon. However, applying as a condition for the observation of a knockout reaction the survival of the core will mean that the reaction probability peaks at the surface of the projectile allowing only a part of the wavefunction to be sampled. An example of spectroscopy using momentum distributions is given in Fig. 2.5 which demonstrates the sensitivity of knockout reactions to probe nuclear structure. This systematic study of increasingly neutron-rich isotopes for various nuclei was made at the GANIL laboratory using a

primary beam of ^{40}Ar at an energy of 70 MeV.A producing secondary fragments in the energy range: 43−71 MeV.A. The longitudinal momentum distributions of the residual fragments after neutron removal are shown with their theoretical distributions. The shape and width of the momentum distributions change dramatically when crossing the $N = 8$ shell and $N = 14$ sub-shell closures. Halo states are recognised by the low separation energy of a valence neutron along with a characteristically narrow momentum distribution that describes nucleon removal from an s-wave state, i.e. ^{15}C and ^{14}B which also have enhanced neutron removal cross sections compared to their neighbouring isotopes [56]. The ℓ-value of the knocked-out nucleon can be obtained from the shape of its momentum distribution which can be reproduced with Glauber model calculations that make use of the separation energy of the nucleon and are shown along with the data. It has also been suggested that additional nuclear structure information relating to the deformation of nuclei produced far from stability, could be extracted from the momentum distributions of the residual fragments of a knockout reaction [57].
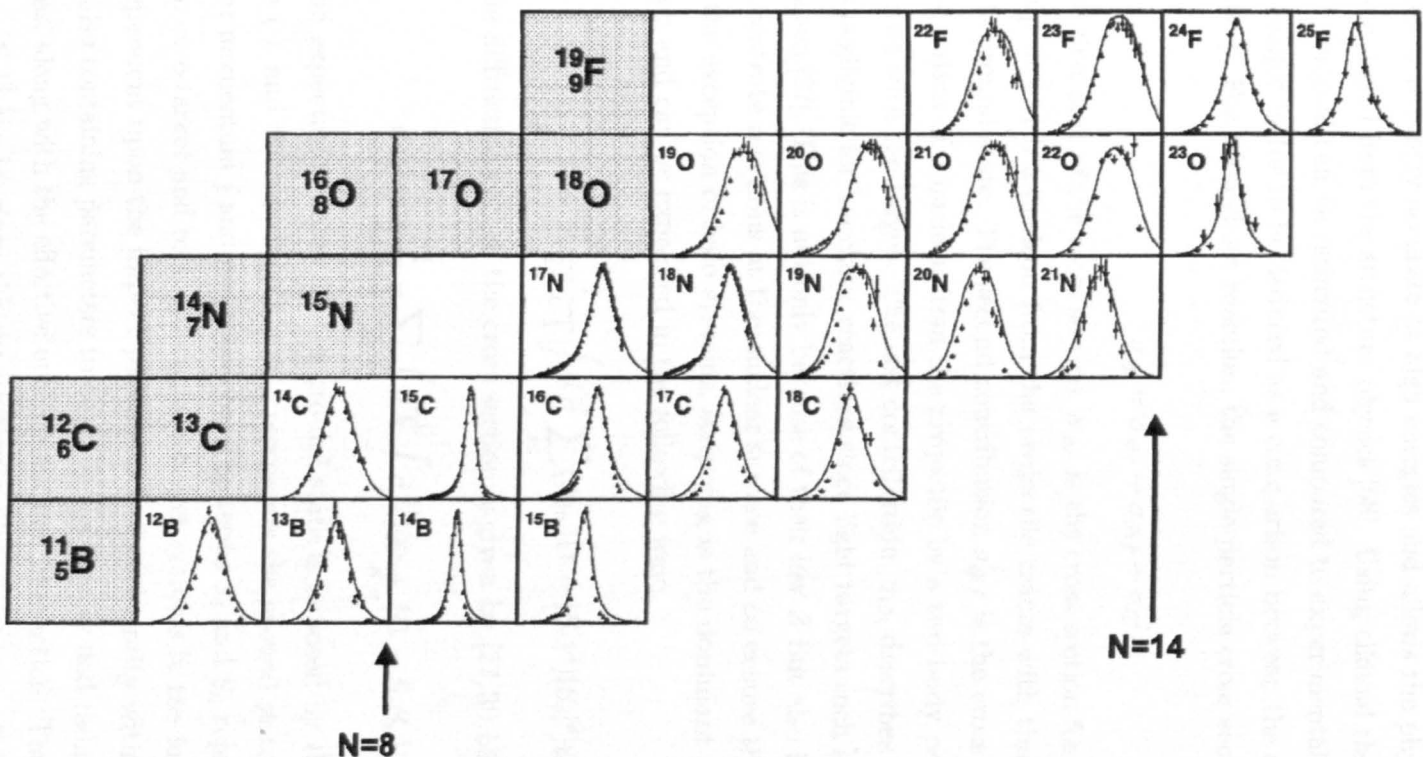
Figure 2.5: Inclusive longitudinal momentum distributions for $1n$ removal from light neutron-rich isotopes on a 490 mg/cm^2 C target. Fragments were produced with a primary beam of 70 MeV.A ^{40}Ar which was used to generate fragments from ^{12}B - ^{25}F in the energy range: 43-71 MeV.A. The solid lines correspond to Glauber model calculations which can be used to extract the ℓ-value of the removed nucleon. Figure taken from [56].

In addition to the adiabatic approximation, the eikonal approximation is also assumed. This requires that the nucleon involved in the reaction with the target undergoes no deflection and that the reaction be concentrated at forward angles. This approximation becomes increasingly accurate at high energies and allows the physics of the reaction to be disentangled from the structure physics [58]. Using eikonal theory, cross sections for nucleon removal can be estimated and compared to experimental results. This allows a spectroscopic factor to be deduced as a comparison between the experimental data and the theory. For a knockout reaction, the single-particle cross section is given by:

$$\sigma_{sp} = \sigma_{str} + \sigma_{dif} + \sigma_C \qquad (2.2)$$

The first part of the cross section, σ_{str} is the cross section for 'stripping' or inelastic breakup in which a nucleon from the projectile reacts with the target and is excited from its ground state. The second contribution σ_{dif} is the cross section for diffraction or dissociation of a nucleon from the projectile by a two-body process involving elastic scattering with the target. The last contribution, σ_C, describes Coulomb dissociation and is negligible for knockout reactions since light targets such as beryllium or carbon are chosen [27]. This is not only because of their low Z but also because of their ability to concentrate reactions at the nuclear surface and so ensure the survival of the core. With the exception of halo systems, stripping is the dominant process in a knockout reaction and can be expressed in the following way:

$$\sigma_{str} = \frac{1}{2j+1} \int d\vec{b} \sum_m \langle \psi_{jm} | (1 - |S_n|^2)|S_c|^2 | \psi_{jm} \rangle \qquad (2.3)$$

The diffractive part of the cross section is given by [27,30,55]:

$$\sigma_{dif} = \frac{1}{2j+1} \sum_{\sigma,m} \int d\vec{k} \int d\vec{b} | \langle \psi_{\vec{k}\sigma} | (1 - S_c S_n) | \psi_{jm} \rangle |^2 \qquad (2.4)$$

The expectation value for the ground state is denoted by the quantity contained within $\langle \; \rangle$, and the wavefunction ψ_{jm} represents the ground state of the projectile with angular momentum j and projection m. The terms S_c and S_n represent profile functions for the core-target and removed-nucleon-target systems in the form of matrices. These are dependent upon the impact parameter b of each entity with respect to the target, while also containing parameters to describe the density and radii of the core and target systems, along with the effective nucleon-nucleon interaction. Thus, the quantities $|S_c|^2$ and $1 - |S_n|^2$ can be given the simple physical interpretation of the probability that the core scatters elastically from the target and the reaction probability that the nucleon is removed by the target, respectively. Eqn. 2.3 and Eqn. 2.4 give the probabilities of these two reactions contributing to the nucleon knockout cross section by summing the

above quantities over all projections and impact parameters. The partial theoretical cross sections for knockout to particular core states (I_c^π) are then given by:

$$\sigma_{state}(I_c^\pi) = \sum_{nlj} C^2 S(I_c^\pi, nlj)\sigma_{sp}(I_c^\pi, nlj) \qquad (2.5)$$

where the single-particle occupancy of a state based upon shell model predictions is given by the spectroscopic factor or C^2S for that particular state. The single-particle cross section for removing a nucleon from that state is given by σ_{sp} and derived from eikonal theory as discussed above (Eqn. 2.2). By measuring the core after a knockout reaction has occurred and determining its state, then dividing by the single-particle cross section, the experimental spectroscopic factor can be determined and structural information about the nucleus extracted and compared to the shell model predictions. Summing the partial cross sections over all possible bound states in the core gives the total inclusive cross section for nucleon removal via a knockout reaction [27, 30, 55].
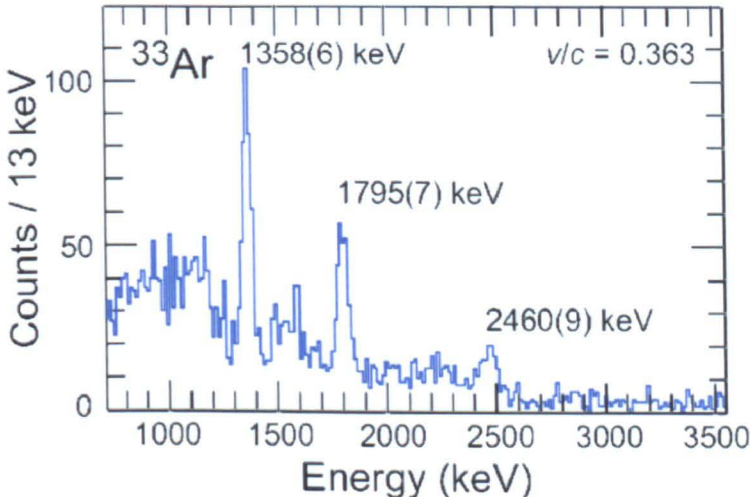
Figure 2.6: A γ-ray spectrum measured using a segmented Ge detector array for ^{33}Ar produced in a one neutron removal reaction at 70 MeV.A on a ^{9}Be target. Figure taken from [28], modified from [59].

In order to determine which states are populated during a knockout reaction, γ rays can be measured in coincidence with the forward fragments in the reaction. An example of such a spectrum is shown in Fig. 2.6 for neutron knockout from the proton-rich ^{33}Ar measured at the current National Superconducting Cyclotron Laboratory at MSU [59]. Selecting different transitions in the γ-ray spectrum allows exclusive cross sections and momentum distributions to be measured and determination of the different single-particle components to the reaction to be made for comparisons with shell model

predictions as discussed above. Exclusive momentum distributions for ^{33}Ar are shown in Fig. 2.7.
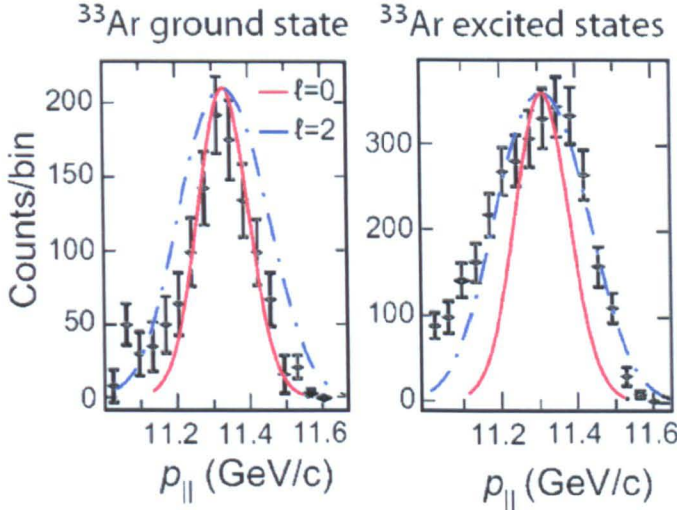
Figure 2.7: Exclusive longitudinal momentum distributions for ^{33}Ar created using a neutron knockout reaction measured in coincidence with the ground and excited states in the γ-ray spectrum shown in Fig. 2.6. Fits for two different ℓ values are shown. This figure is also taken from [28], modified from [59].

Fragments emerging from a knockout reaction will continue to travel at a velocity roughly equal to the projectile velocity. Therefore, γ rays emitted from the fragment will require an event-by-event Doppler correction in order for their energy in the rest frame of the projectile to be reconstructed. Doppler broadening due to the finite opening angle of the detectors cannot be corrected for, however, and will contribute to the final resolution of the γ-ray spectrum. For halo systems, knockout reactions will populate unbound states where the nucleus will promptly break up into its constituent parts. If all fragments can be detected at forward angles the invariant-mass method can be used instead of γ rays to determine the states that are populated in the daughter nucleus.

The formalism for single nucleon knockout reactions is being adapted to describe two nucleon knockout, which is of experimental interest for a number of reasons. Firstly, two neutron knockout from proton rich projectiles and two proton knockout from neutron rich projectiles allow production of the most exotic nuclei at the neutron and proton drip lines by a direct reaction [60]. Such nuclei may not be feasibly produced by standard production methods with sufficiently high statistics until the next generation of rare isotope facilities are operational. An example case would be ^{36}Mg (the most neutron

rich isotope with $Z = 12$) successfully produced for in-flight γ-ray spectroscopy using the two proton knockout reaction: $^9\text{Be}(^{38}\text{Si}, {}^{36}\text{Mg} + \gamma)\text{X}$ [61]. Secondly, the correlation effects between *pp*, *nn* and *np* pairs can be investigated by determining the inclusive and exclusive cross sections for each of their corresponding channels and comparing these to shell model predictions. Indeed, such cross sections for stable nuclei such as ^{12}C are needed to constrain recent predictions from theoretical calculations [62].

2.3 Quasi-free Scattering Reactions

Quasi-free scattering reactions occur when a high energy projectile (usually $\gtrsim 100$ MeV.A) knocks a nucleon out of a nucleus and no further violent interaction occurs between the nucleus and the incident or the two outgoing particles [63]. These are the ideal reactions to overcome the surface localisation that dominates both transfer and knockout processes. The first quasi-free reactions were observed at Berkeley in 1952 when a 350 MeV proton beam was used to bombard a lithium target. Pairs of protons emerging from the target were observed to have a strong angular correlation and an opening angle between the pair of $\sim 90°$ [64], a result that was expected from multiple scattering theory and the impulse approximation [65]. Following this discovery, a theoretical framework was developed to describe the process as one similar to nucleon-nucleon scattering with deviations from this picture attributed to the fact that the reaction takes place in the presence of nuclear matter where the proton is not at rest but has a momentum distribution [66]. In addition, the impulse approximation was applied (as outlined above for knockout reactions) so that the momentum of the removed nucleon can be described as shown in Fig. 2.8 where $\vec{k}_0$, $\vec{k}_1$, $\vec{k}_2$ and $\vec{k}_{A-1}$ are the momentum vectors of the incoming projectile (p), the knocked-out nucleon (N), the projectile after the collision (p) and the residual fragment $(A-1)$, respectively.

The same notation is used for the kinetic energy T. Given the impulse approximation, the conservation of momentum and energy gives:

$$\vec{k}_{A-1} = \vec{k}_0 - \vec{k}_1 - \vec{k}_2 = -\vec{k}_3 \qquad (2.6)$$

So that the recoil momentum of the $(A-1)$ fragment is equal and opposite to the momentum of the knocked-out nucleon while it was bound within the nucleus $(\vec{k}_3)$. The separation energy of a nucleon, S is given by:

$$S = T_0 - (T_1 + T_2 + T_{A-1}) \qquad (2.7)$$

Differential cross sections for quasi-free scattering reactions have typically been expressed within the Distorted Wave Impulse Approximation (DWIA) [67] such that
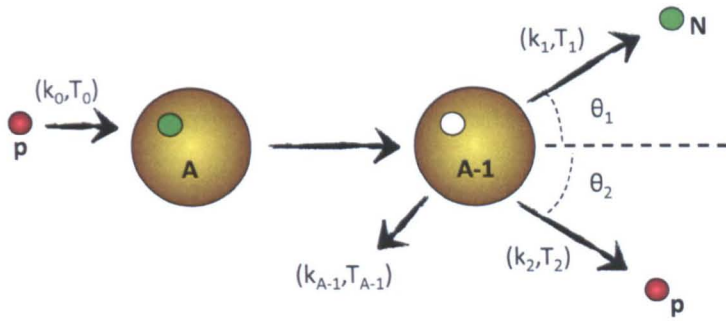
Figure 2.8: Schematic of a (p, pN) quasi-free scattering reaction occurring in normal kinematics.

for $(p, 2p)$ reactions:

$$\frac{d^3\sigma}{d\Omega_1 d\Omega_2 dE_1} = S_p F_k \frac{d\sigma}{d\Omega_{p-p}} G\left(\vec{k_3}\right) \tag{2.8}$$

where S_p is the spectroscopic factor for the bound proton, F_k is a kinematic factor, $\frac{d\sigma}{d\Omega_{p-p}}$ is the free proton-proton scattering cross section and $G\left(\vec{k_3}\right)$ is the distorted momentum distribution of the knocked out proton. This distortion for the outgoing proton is modelled using complex optical potentials with parameters chosen according to the energy and mass range of the experiment [68].

High energies are chosen for quasi-free scattering so that the nucleon-nucleon cross section is at a minimum [30]. This ensures the effects from final state interactions are small. When these final state interactions occur, the incoming, or two outgoing particles, can interact with other nucleons before or after the quasi-free process, causing more than one nucleon to be removed or causing further excitations that distort the information that can be obtained from the actual quasi-free event. It was found that although these interactions were estimated to occur frequently (due to the mean free path of projectiles such as protons being less than the nuclear size), by ensuring a sufficiently high momentum transfer from the projectile to the knocked-out nucleon, distortion of momentum and angular correlations could be minimised and these processes form a smooth background on top of which energy and momentum peaks from the nuclear structure could appear [69]. For protons, an incoming energy of 400 MeV.A was considered to be optimal and deeply bound states could be observed in light nuclei [69]. In order to reduce further distortion from unwanted reactions within the nucleus and to determine whether deeply bound states could be observed in heaver nuclei such as

^{40}Ca, electrons were chosen as a probe, rather than protons, since they have a much longer mean free path in nuclear matter thus reducing the distortion to just one of the outgoing particles. These ideas were put forward by Jacob and Maris in 1962 [70,71] and later confirmed in the experiments discussed in the next section.

2.3.1 Electron Induced Quasi-free Scattering

In order to confirm the predictions of Jacob and Maris concerning electron quasi-free scattering, experiments of this sort were carried out in 1964 at the Frascati synchrotron in Rome [72]. An electron beam of $\sim$550 MeV was scattered from ^{12}C and measured at a fixed angle of 51° in the reaction ^{12}C$(e, e'p)X$ and comparisons made to the existing data for ^{12}C$(p, 2p)X$. Additionally, the reaction ^{27}Al$(e, e'p)X$ was carried out under the same conditions and evidence of deeply-bound states was observed as with ^{12}C. This confirmed the role of final-state interactions since previously deeply-bound structures had not been visible beyond ^{16}O using $(p, 2p)$ reactions and thus electrons were confirmed as a better probe for gathering data on the single-particle degrees of freedom in stable nuclei [72]. Taking advantage of this new probe, $(e, e'p)$ reactions were carried out on a large range of masses from ^{2}H to ^{208}Pb at the NIKHEF-K facility in the Netherlands [73], providing a wealth of information concerning the shell structure of these stable nuclei [74]. As well as their transparency to nuclear matter, electrons being point-like particles, provide high-resolution energy measurements ($\sim$100 keV was achieved at NIKHEF-K) which allows the separation of states that are close in energy, e.g. the $3s_{1/2}$ and $2d_{3/2}$ states shown in Fig. 2.9.

The data obtained from $(e, e'p)$ reactions can be expressed in the form of a spectral function: $S(E, p)$, as with Fig. 2.9. This describes the probability of finding a proton with energy E and momentum p in the nucleus of interest. Data produced by $(e, e'p)$ reactions on stable nuclei confirmed aspects of the shell model, in particular the existence of shell structure even for the most deeply bound nucleons. However, the data also showed considerable quenching of the single-particle strength in the valence states compared to the shell model predictions (Fig. 2.10). When this quenching was compared to theoretical models that account for nucleon-nucleon correlations, it was found to be consistent [74,76].

More recently, efforts have been made towards understanding these correlations within nuclei using $(e, e'p)$ reactions in laboratories such as JLab (Virginia, USA). This was made possible by the availability of spectrometers with a high resolving power and the ability to carry out measurements with high energy and large momentum transfer reactions. Using electron beams of several GeV the presence and abundance of np and
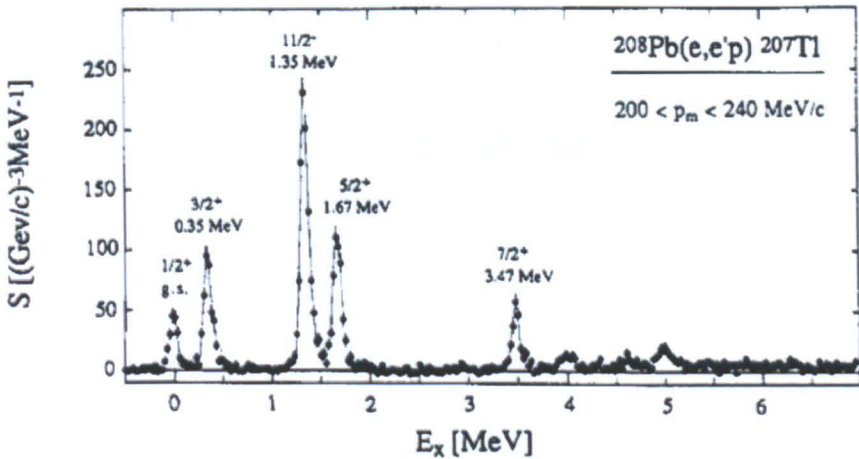
Figure 2.9: The spectral function for the ^{208}Pb$(e, e'p)^{207}$Tl reaction integrated across the momentum range: 200−240 MeV/c. Electrons of 450 MeV impinge upon the Pb target transferring an energy of ∼100 MeV to the knocked out proton. Image taken from [75].

pp pairs have been measured in stable nuclei such as ^{12}C. It was found that *np* pairs were far more common than *pp* ones as depicted in Fig. 2.11 [78,79].

In the future, experiments such as The ELectron Ion Scattering experiment (ELISe) [80] will measure the scattering of electrons off radioactive nuclei at the FAIR facility in Darmstadt. This presents significant technical challenges since neither the electrons nor the radioactive nuclei can exist as targets but have to collide as two beams at high energy. In order to achieve this, two storage rings need to be used and the ELISe spectrometer will be placed between them. The luminosities used for experiments with ELISe are expected to be of the order $10^{26}-10^{28}$ cm^{-2}s^{-1} which will be lower than those used for previous electron scattering experiments with fixed targets, However, the spectrometer is foreseen to cover a larger solid angle $(50°-100°)$ with the aim of capturing a large fraction of the reaction cone of the colliding beams. Elastic scattering reactions (e, e') to measure the charge distribution of exotic nuclei will be possible and potentially quasi-free proton, neutron and cluster knockout. Two nucleon knockout reactions such as $(e, e'2N)$ may also be possible as complementary studies to those discussed above for knockout reactions with radioactive beams and light fixed targets, as well as the same reactions carried out currently on stable nuclei at JLab [81].

2.3.2   Proton Induced Quasi-free Scattering

Given the difficulties presented in the last section for using $(e, e'p)$ reactions to investigate radioactive nuclei, the alternative approach is to revert to using proton induced
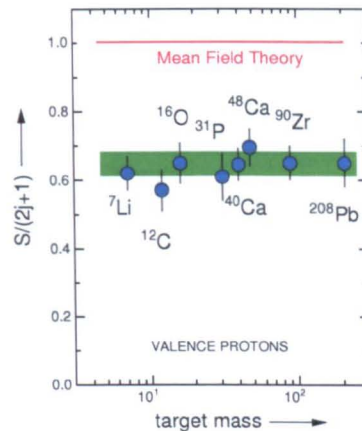
Figure 2.10: Spectroscopic factors obtained from $(e, e'p)$ data as a function of the target mass. A significant departure from the mean field theory (upon which the shell model is based) of $\sim 35\%$ can be seen. This is consistent with Fig. 2.1. Image taken from [77], modified from [76].

quasi-free scattering in inverse kinematics. For example, $(p, 2p)$ reactions where the radioactive beam is directed onto an extended proton target such as liquid H_2 or a fixed proton rich target such as CH_2. Such a reaction is depicted for a stable beam of ^{12}C in Fig. 2.12 and will be discussed as the topic of this thesis.

Using inverse kinematics has the advantages already discussed in section 2.2, namely coincident measurements of the $A - 1$ core and its emitted γ-rays. Additionally, for quasi-free reactions, the opportunity to understand better the nature of final state interactions arises by comparing the measurements of the knocked out nucleon and the $A - 1$ core. For light nuclei, it has been shown that $(p, 2p)$ reactions have comparable efficiency for probing the nucleus' inner region when compared to $(e, e'p)$, and only for heavy nuclei such as ^{208}Pb does the $(e, e'p)$ reaction become much more preferable [82]. However since quasi-free reactions have traditionally been carried out on stable nuclei in normal kinematics, work is needed to establish the method using inverse kinematics for radioactive beams. Promising results have been obtained at the HIMAC facility in Chiba, Japan for the stable and radioactive isotopes $^{9-16}$C [83]. In this experiment, the carbon beams of 250 MeV.A were directed onto a solid 44 mg/cm^2 H_2 target after which proton pairs were detected in two NaI telescopes placed at fixed angles of 39° with an acceptance of $\pm 9°$ in both the horizontal and vertical dimensions in order to capture as many $(p, 2p)$ reactions as possible. Forward fragments were separated in a magnetic spectrometer and their energy loss and measured in a plastic scintillator detector. Limitations of this work stem from the maximum available beam energies and lack of γ-ray measurements resulting in poorer resolution for the final energy spectrum.
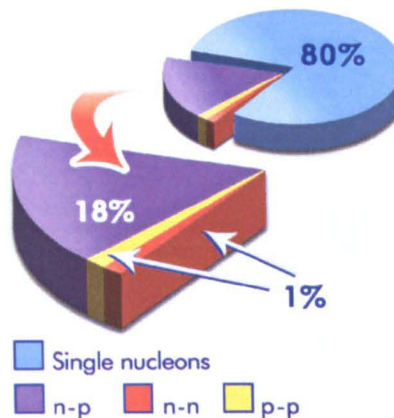
Figure 2.11: The average fraction of nucleons in correlated high momentum pairs in ^{12}C. Most of the nucleons: $(80\pm5)\%$ are low momentum independent or long range correlated nucleons, $(18\pm5)\%$ are np short range correlated pairs and $(1\pm0.3)\%$ are pp or nn short range correlated pairs. Image taken from [79].

The method of proton induced quasi-free scattering using inverse kinematics has also been employed for radioactive beams at the GSI Laboratory in Darmstadt [84]. The experiment consisted of directing a high energy beam ($\sim$700 MeV.A) of radioactive neutron-rich $^{6-8}$He onto an extended liquid H_2 target of 708 mg/cm^2. Time of flight (TOF), energy loss and position measurements were made in order to select the species of the ion and its trajectory onto the target. Recoiling protons were also tracked and identified as they emerged at large angles from one side of the target in coincidence with the residual fragments that were identified at forward angles by measurements made before and after the magnetic spectrometer ALADIN (see Fig. 2.13). Using this technique, the reactions (p,pn), $(p,p\alpha)$ and remarkably (p,p^6He) were observed, and transverse momentum distributions of knocked out α-clusters and neutrons were measured, along with their spectroscopic factors from which the cluster structure of these drip-line nuclei could be deduced.

Building on this earlier work using radioactive neutron-rich beams, additional investigations of the $(p,2p)$ and (p,pn) reactions have been made using ^{57}Ni and a modified version of the LAND-ALADIN setup at GSI [85]. Modifications included additional detectors for larger angular coverage around the target, as well as the full LAND detector and a CH$_2$ target rather than liquid H_2. Angular correlations indicative of quasi-free reactions were observed. Currently, the setup has been upgraded further to begin acting as a prototype for the future R^{3}B setup at the FAIR facility. Both the current and future setup are discussed in more detail in chapter 3. The current
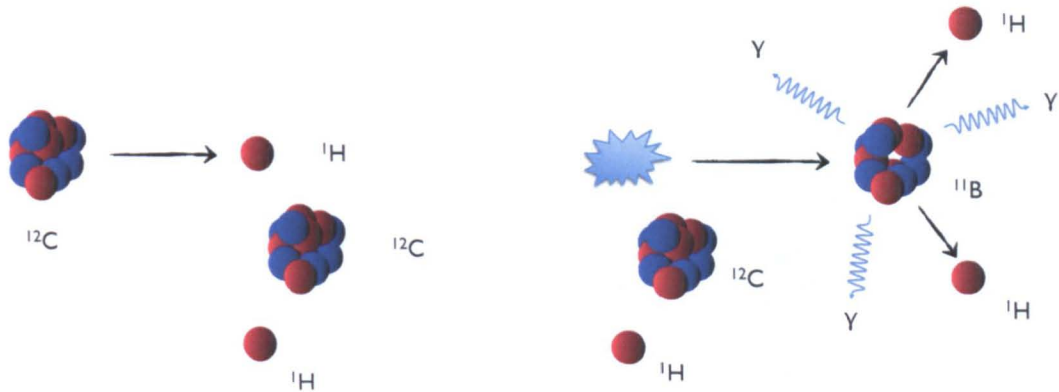
Figure 2.12: Schematic of a ^{12}C ion incident on a CH$_2$ target undergoing a ^{12}C$(p, 2p)^{11}$B reaction. After the reaction, one proton from the target and another from projectile are emitted at large angles and the ^{11}B fragment can be left in an excited state that decays via γ ray or particle emission.

upgraded setup allows proton induced quasi-free scattering reactions to be measured in complete kinematics such that all interactions in the target can be reconstructed providing much more information than previous quasi-free scattering experiments using inverse kinematics.

2.4 Summary

Direct reactions have a long history and have proved to be a valuable tool for carrying out nuclear spectroscopy. Both transfer and knockout reactions have led to a better understanding of the structure of the nucleus but with the limitation that the reaction mechanisms themselves are surface dominated. Thus they are not able to probe the bulk nuclear matter containing more deeply bound nucleons or shed light on the nature of the nucleon-nucleon interaction inside nuclear matter. In contrast to this, quasi-free reactions especially the $(e, e'p)$ variety have proved to be a powerful tool in probing both the valence and the deeply bound states in nuclear matter, as well as successfully operating over a large range of masses in stable nuclei. The nature of final state interactions and the nucleon-nucleon interaction are also open to investigation by the comparison of measurements on the knocked out nucleon with its residual core. Although electrons are the ideal probe for these kind of investigations, protons have the advantage of being much easier to use for investigations of radioactive nuclei because of their ability to exist as a target. By building on the techniques established for knockout reactions, and using facilities at the GSI laboratory, proton induced quasi-free scattering has been
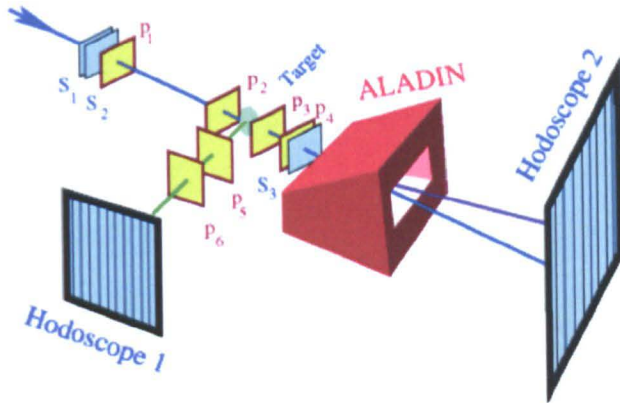
Figure 2.13: The setup used by Chulkov *et al.* [84] to observe the quasi-free scattering reactions: (p, pn), $(p, p\alpha)$ and $(p, p^6 He)$ on the exotic nuclei $^{6-8}$He. TOF measurements are made by the scintillators (S) and hodoscopes. Tracking of the incoming radioactive beam and reaction products is done using multi-wire proportional counters (P).

performed using inverse kinematics and measured using a kinematically complete setup. Measurements have been made on the stable ^{12}C nucleus with the aim of reconstructing quantities such as the energy and momentum of removed nucleons as well as the cross section of the reaction process itself. It was hoped that these quantities could be obtained from both the scattered protons and the forward emitted fragment allowing conclusions about the role of final state interactions to be drawn. However, for reasons outlined in the later chapters, only precise measurements with the residual core have been possible. These are presented alongside a comparison with previous work obtained using normal kinematics and conclusions are drawn concerning further work on radioactive beams that will be carried out both with the current LAND/R^{3}B setup and the future complete R^{3}B setup at the FAIR facility.

Chapter 3

Experimental Apparatus

This chapter describes the apparatus used for the production, identification and acceleration of the beam, as well as the guiding of the beam onto the target where the reactions between the beam and a target are measured using the LAND/R^3B setup. This setup is acting as a prototype for the future R^3B setup at the FAIR facility.
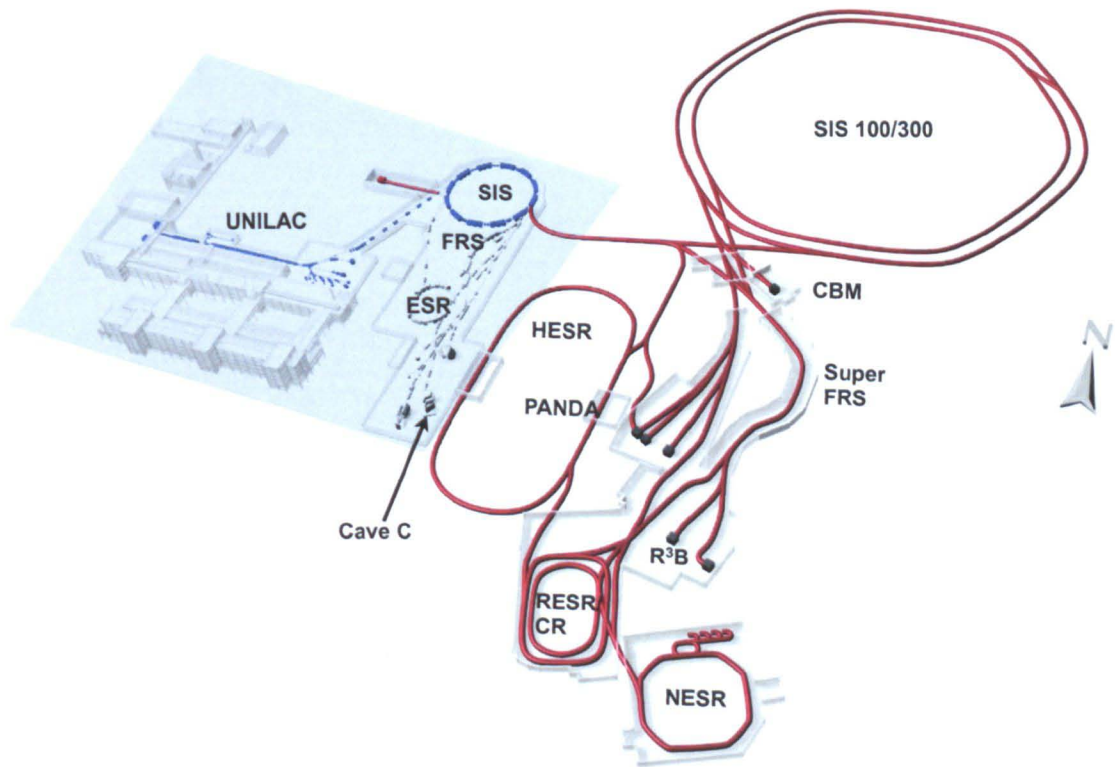
Figure 3.1: The current GSI Laboratory with the proposed FAIR extension. The GSI Laboratory (highlighted in grey) contains the beam line shown in blue and the proposed FAIR facility is shown in red with experimental areas indicated.

3.1   The GSI Accelerator System

The primary beam consists of ions that are generated from ion sources located at the beginning of the beam path. The UNIversal Linear ACcelerator (UNILAC) is then responsible for pre-accelerating these ions up to energies of 18 MeV.A and injecting them into the Heavy Ion Synchrotron (SIS) where further acceleration takes place (Fig. 3.1). The maximum energies that the SIS can deliver are defined by its maximum magnetic bending power of 18 Tm. With such magnetic bending power a maximum energy of 1−4.5 GeV.A can be reached depending on the ion species. The accelerator complex can accelerate all stable ions from hydrogen to uranium, delivering high quality stable beams which can be used for in-flight production of secondary radioactive beams by allowing them to impinge upon a production target at the exit of the SIS. However during the experiment discussed in this thesis[1], only a stable ^{12}C beam was used, allowing the primary beam accelerated in the SIS to be sent directly to Cave C (see Fig 3.2) without the need for the production of a secondary beam and the use of the FRagment Separator (FRS).

---

[1]The experiment (known as s296) used a beam intensity for the production runs of $\sim 10^4$ ions/s and a beam directly from the SIS with an energy of 400 A.MeV. During the calibration runs at the start of the experiment these values were varied slightly.
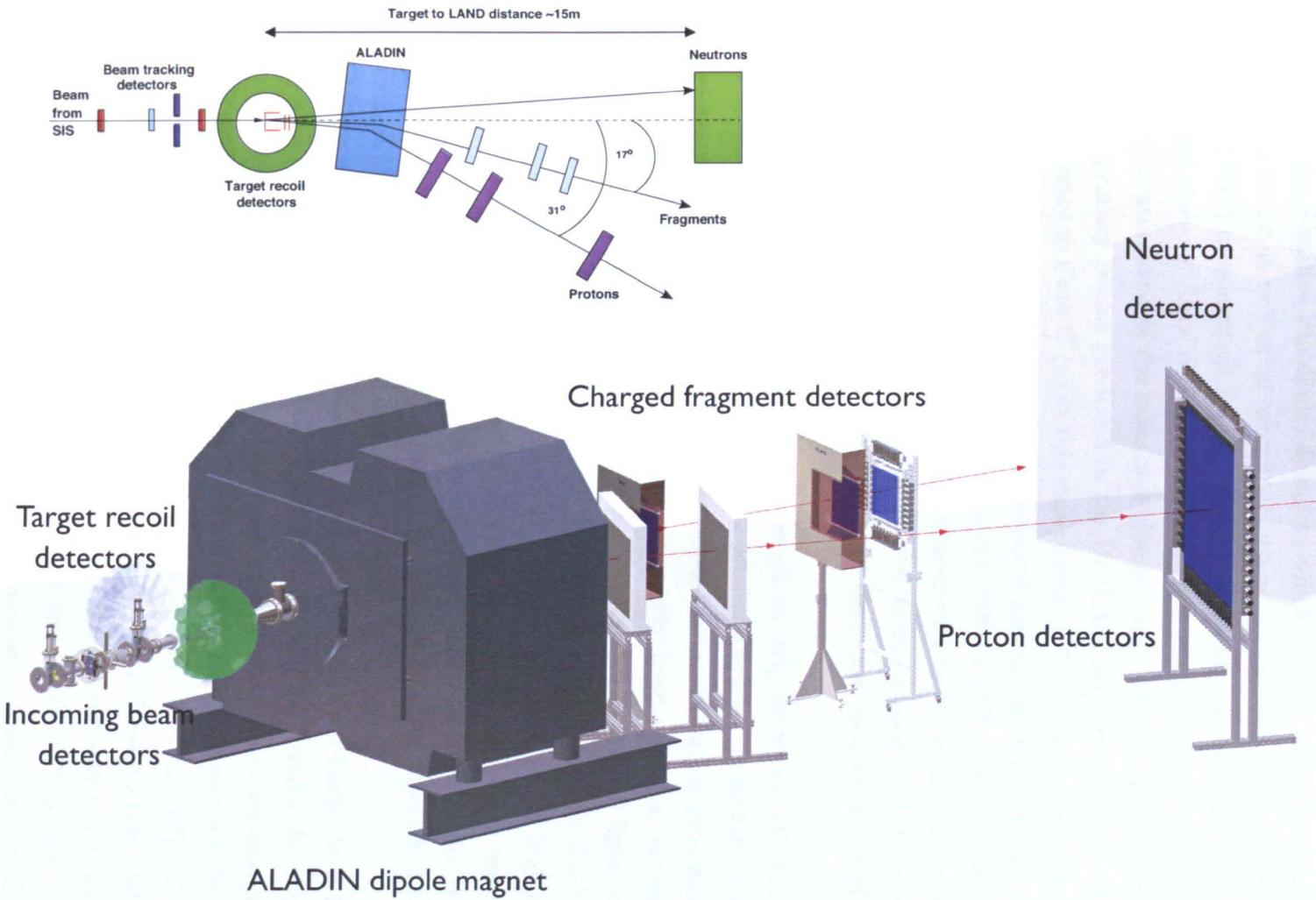
Figure 3.2: The LAND/R³B setup based in Cave C at GSI. The target-recoil detectors (DSSSDs and NaI calorimeter) together with the detectors after the ALADIN dipole magnet provide a kinematically complete measurement of all participants in a nuclear reaction. The inset shows a schematic of the setup to give the reader an idea of the scale.

3.1.1 The LAND/R³B Setup in Cave C

The beam travelling from the SIS or the FRS is identified upon entering Cave C using the PSP (Position Sensitive Pin diode) detectors which give the position of the beam on the reaction target as well as an energy loss measurement. When combined with a time-of-flight (TOF) measurement made between the scintillator detectors in the FRS (S2 and S8) and the scintillator detector POS[2], situated at the entrance to Cave C, an event-by-event measurement of the mass over charge (A/Z) ratio of incoming ions can be made. For primary beams produced in the UNILAC, accelerated in the SIS and transported directly to Cave C (as in this experiment) a TOF measurement between the FRS and Cave C is not possible. Verification of the incoming ion species can be carried out using energy loss measurements in the POS or PSP detectors before the target. Without accurate position and TOF measurements before the target only a rough measurement of the Z of the incoming ion can be made using POS, however, if a light stable beam is used the purity will be high so that these measurements of Z are not necessary.

Immediately after the target are six double-sided silicon strip detectors (DSSSDs) that form the tracking component of the target-recoil detection system. In addition to measuring the angular distribution and energy loss of the scattered reaction products, they are also used to track the forward fragments and unreacted beam particles. Surrounding the DSSSDs and the target is a 4π array of NaI crystals for γ ray and light particle detection known as the Crystal Ball (XB) [86]. In addition to the γ-readout, the forward crystals (2π) of the Crystal Ball also have readouts for the detection of high energy protons, neutrons and charged fragments. Individual crystals have been tested and found to absorb protons with energies up to $\sim$270 MeV [23]. The detectors for tracking the beam onto the target and the target-recoil detectors are depicted together in Fig. 3.3 and discussed in more detail in the following sections.

Situated after the detectors surrounding the target is ALADIN (A Large Area DIpole magNet). All reaction fragments that travel forward will pass through the magnetic field allowing the separation of the reaction products by their mass-over-charge ratio (A/Z) (see Eqn. 3.1). The setup of Cave C after ALADIN has three sections. Neutrons are detected around 0° by the Large Area Neutron Detector (LAND) [87] . Charged fragments are measured around 16.7° firstly in the two GFI (Grosse FIbre) detectors and finally in the Neue Time of Flight wall (NTF). Protons are measured around 31°, firstly by two drift chambers (PDC), and finally in the large Time of Flight Wall (TFW). These angles are given with respect to the beam axis and are a consequence of Eqn. 3.1.

---

[2]POsition sensitive Scintillator, although it is presently used primarily for timing purposes.

3.2 Detection System for the Incoming Beam

In order to correctly identify the incoming ions, it is usually necessary to measure energy loss, position and TOF. The position measurements allow the magnetic rigidity ($B\rho$) of the particle to be determined, and the TOF measurements can be combined with the $B\rho$ to identify the (A/Z) of each projectile (Eqn. 3.1):

$$B\rho \propto \frac{A}{Z}\beta\gamma \qquad (3.1)$$

where $\beta = v/c$ (c is the speed of light) and γ is the Lorentz factor given by: $\gamma = \sqrt{1/(1-\beta^2)}$. The energy loss of an ion is used to identify the atomic number, Z. This allows the identification of every ion accepted onto the target to be known.
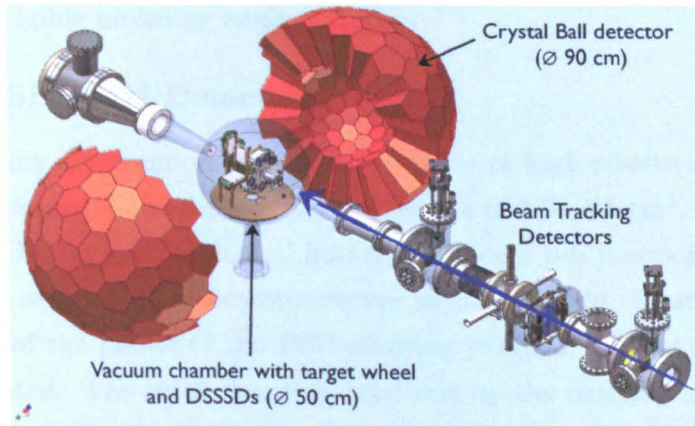
Figure 3.3: The incoming tracking and target-recoil detection systems for the LAND/R^{3}B setup. The direction of the beam is shown by the blue arrow.

3.2.1 Mass and Charge Identification

In order to determine the velocity for each incoming ion, TOF measurements are made between FRS scintillators and the POS detector situated at the entrance to Cave C. However in this experiment the incoming beam is stable and hence its identity is known right up to the target. Calculating the velocity from the energy of the beam is then straightforward, as the energy of the beam emerging from the SIS is known to be 400 A.MeV which can then be corrected for energy loss in the POS and PSP detectors before the target. The 2D-position measurements made by the PSP/Pixel detectors were not possible during this experiment due to the low charge of the beam[3].

---

[3]In a recent similar experiment, the PSP detectors were replaced by two DSSSDs capable of tracking charges as low as $Z = 1$ (see section 3.3.1).

3.2.2 Tracking the Beam onto the Target

Tracking of the beam onto the target is necessary for determining the incoming angle of the ions, and the interaction point within the target. Both of these are regarded as necessary for accurate momentum reconstruction of the forward fragments. Knowing the trajectory of ions onto the target also allows events caused by incoming ions striking the target frame to be discarded. The lack of position measurements for the incoming ions in this experiment has been compensated for by ensuring a low divergence of the beam. This was checked by the ROLU[4] veto situated after the POS detector but before the target, measuring the diameter of the beam to be ~2×2 mm. Tracking of the beam back towards the target using the in-beam DSSSDs was also possible, thus giving an interaction point for the ions in the target. Because the beam is stable with a low divergence, the assumption has been made that the beam strikes the target in a parallel fashion with negligible incoming angle.

3.2.3 The PSP/Pixel Detectors

The PSP detectors are composed of a square piece of high resistivity n-type silicon. They have a thickness of 300 μm and an active area of 4.5×4.5 cm^2. The front side of the detector has boron ions implanted into it, creating a p-n junction that acts as the anode while the reverse of the detector serves as the cathode. Charge is read out by all four corners of the anode of the PSP allowing position information from passing ions to be collected. The total charge is read out by the cathode and it is this that provides the charge identification of each ion. In order to calibrate the position of the PSP detectors a scintillating mask is placed in front of the anode that consists of a grid of 21×21 pixels each 0.5 mm in diameter and spaced 2.5 mm apart. Light produced in the pixels is guided to a PM-tube mounted outside the detector above the beam line. The Pixel detectors are mechanically inserted into the beam line (Fig. 3.4) during calibration runs at the start, middle and end of an experiment.

3.2.4 The POS Detector

The POS detector (originally used for position measurements) shown in Fig. 3.5 is used for timing and is placed ~2 m before the target, it acts as the start detector for all TOF measurements made with the setup. It consists of a 5×5 cm^2 plastic scintillator that is 200 μm thick. Time and energy signals are read out from four PM-tubes situated on each side of the scintillator and can be used to exclude 'pile-up' effects that occur when the intensity of the beam is too high.

---

[4]Rechts, Oben, Unten, Links (see section 3.2.5)
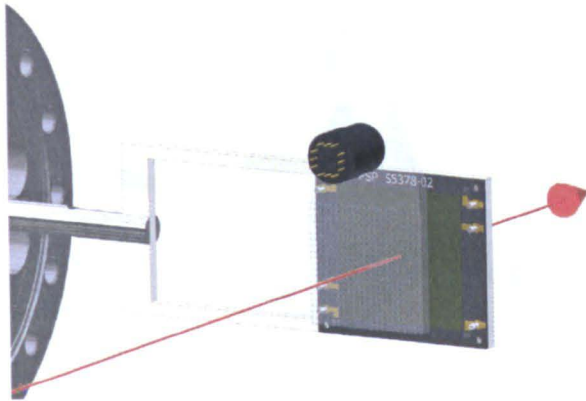
Figure 3.4: The PSP and Pixel detectors with the direction of the beam indicated.

3.2.5 The ROLU Veto

The ROLU veto pictured in Fig. 3.6 is positioned between the first PSP and POS detectors. It has its name taken from the four moveable plastic scintillators that make it up: Rechts, Oben, Unten, Links. The ROLU veto can be used to estimate the beam size and position and permits the veto of any ion that hits these scintillators. When combined with the POS detector, a suitable 'Good Beam' trigger can be defined for accepting events onto the target (see Table 3.2).

3.3 Detection System Surrounding the Target

As discussed in chapter 1, the kinematics of a quasi-free scattering reaction are such that emitted fragments that are not spectators in the reaction such as protons, neutrons or alpha-particles, (from $(p,2p)$,(p,pn) and $(p,p\alpha)$ reactions respectively) will be emitted at large angles relative to the beam axis. Measuring the angular distribution and energy loss of these fragments is necessary in order to determine accurately reactions that have taken place in the target. DSSSDs arranged in a 'box' around the target give angular measurements, while two in-beam DSSSDs allow for Z measurements and tracking of fragments before they pass through the ALADIN dipole magnet. The forward crystals of the Crystal Ball detector can detect neutrons and charged particles as well as γ rays, allowing a measurement of the state from which the particle was removed to be made. A coincidence measurement between events in the DSSSD box and high energy events in the forward hemisphere of the Crystal Ball can be used to create a clean reaction selection for quasi-free scattering events. This is discussed further in chapter 5.
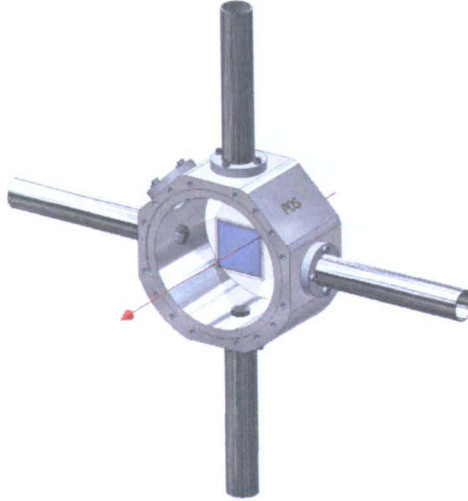
Figure 3.5: The POS Detector with the direction of the beam indicated

3.3.1 AMS DSSSDs

The AMS[5] DSSSDs were originally designed for the AMS-02 experiment on board the international space station (ISS) where they are used for the simultaneous tracking of electrons, protons and nuclei produced by cosmic rays [88–90]. Testing of the DSSSDs has taken place at CERN and GSI where they have been used to track charges from helium up to iron with energies up to 1.5 GeV.A [91, 92]. The DSSSDs were then adapted as an array of detectors for use at the LAND/R^3B setup as a prototype of the R^3B silicon tracker [89]. Each detector is 300 μm thick and has two sides of micro-strips that are perpendicular to each other in order to allow position measurements in x and y thus creating a pixellated detector. The p-side (also known as the S-side) is 72 mm in length, has an implantation pitch of 27.5 μm and a readout pitch of 110 μm. The n-side (also known as the K-side) has a length of 40 mm, and an implantation and readout pitch of 104 μm. The S-side is read out every four strips and has 640 strips in total. The K-side has each strip read out and has 384 strips giving each DSSSD a total of 1024 strips. In this experiment six DSSSDs were used, four arranged in a box like structure surrounding the beam as it emerges from the target, and a further two placed in the beam ∼10 cm and ∼14 cm after the target (see Fig. 3.7). The box structure allows the precise angular information of charged reaction products to be obtained before they deposit their energy in the Crystal Ball. The two in-beam DSSSDs allow a Z measurement ∼10 cm after the target which can be made in coincidence with a Z measurement in the NTF detector after ALADIN. This is useful for removing

---

[5]Alpha Magnetic Spectrometer
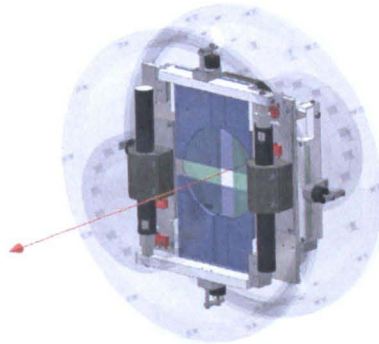
Figure 3.6: The ROLU veto with the direction of the beam indicated. The four scintillators can be individually moved to limit the size of the beam on the target.

unwanted reaction products that have been made after the target due to reactions with the air or other material in the setup. The position measurements of the fragments using the in-beam DSSSDs before the magnet are used together with positions taken after ALADIN for the tracking of the fragments through the magnetic field.

3.3.2 Crystal Ball Detector

The Crystal Ball detector is used for measuring γ rays and scattered particles from quasi-free reactions. It is a 4π array of 162 NaI scintillators, 150 of which have hexagonal geometry and 12 of which are pentagonal. These modules (usually called crystals) create a 'shell' of NaI that is 20 cm thick, and an inner chamber that is 48 cm in diameter, inside which the DSSSDs and target wheel are fixed (see Fig. 3.8). In addition to the readout for γ rays, the crystals in the forward half of the detector (2π) each have an additional high energy readout for the detection of the charged fragments or neutrons that are produced during a quasi-free reaction with the target. The response of the crystals to high energy protons is discussed further in chapters 4 and 6 of this thesis. Detection of neutrons is also possible with the NaI crystals, although a full energy measurement is more challenging due to the fact that they are uncharged and can only be detected by the crystals if a secondary nuclear reaction takes place. Table 3.1 gives an indication of the performance of the Crystal Ball detector taken from [86].

3.4 Detection System after the ALADIN Magnetic Field

After passing through the target chamber, fragments will be strongly forward focused due to the high energy of the beam. Most of the fragments will therefore make it
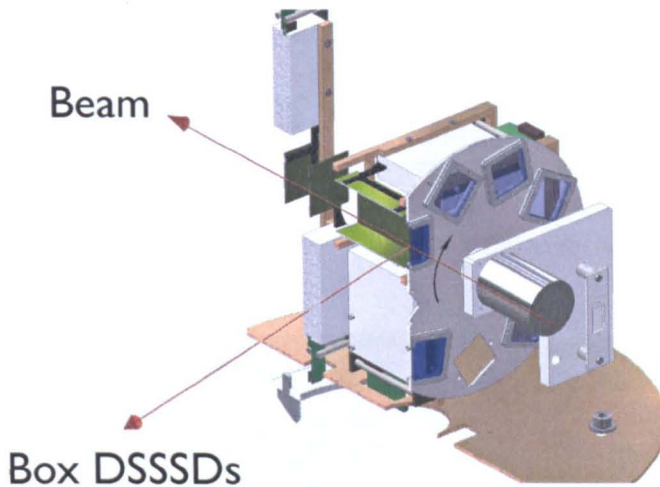
Figure 3.7: The DSSSDs detectors and their electronics with the target wheel and mounting structures.

through the ALADIN magnetic field and be separated by their A/Z ratio, before being detected and tracked in one of the three sections of outgoing detectors.

3.4.1 Neutron Branch

After a reaction with the target, nuclei which are excited into the continuum may decay or break up by emitting neutrons. For decays such as this, the Large Area Neutron detector (LAND), can be used to measure the neutron(s) in coincidence with other decay products. The LAND detector can also act as a trigger allowing the rough identification of reaction channels without needing the position, TOF or energy loss of a neutron (see Table 3.2). The LAND detector is a high efficiency neutron detector capable of detecting neutrons between 100 and 1000 MeV [87] and is placed ∼14.7 m downstream of the target. The detector is composed of 200 scintillating paddles 2 m in length and 10 cm×10 cm in width and depth. Each paddle contains ten sheets of iron, the outer sheets are 2.5 mm thick and the inner ones 5 mm thick. 'Sandwiched' between these are ten 5 mm thick layers of scintillator (see Fig. 3.9), thus the composition of the detector is 50% iron and 50% scintillator.

A high energy neutron produces charged particles in the iron that in turn produce light in the scintillating material that is read out by the two PM-tubes placed at either end of the paddle. Ten paddles are arranged to form a 2×2 m² plane. Ten of these

Total Efficiency	$E_\gamma = 1$ MeV	97%
Total Energy Resolution	$M_\gamma = 20$	18 - 22%
Multiplicity Resolution	$M_\gamma = 20$	25 - 30%
Intrinsic Energy Resolution (single crystal)	$E_\gamma = 662$ keV	7.8%
	$E_\gamma = 1332$ keV	5.5%
Time Resolution (single crystal)	2.8 ns	
Opening angle (single crystal)	14 deg	

Table 3.1: Crystal Ball efficiency and resolution parameters taken from an earlier experiment [86].

Figure 3.8: The Crystal Ball detector opened to allow the positioning of the target chamber.

planes are then stacked together with alternating horizontal and vertical planes forming a detector that is 1 m deep (see Fig. 3.10), with an improved position resolution due to the measurements that can be made in x, y and z. Position information is retrieved by combining the distance of the hit along the paddle given by the time difference between the hits in the PM-tubes, and the absolute position of the paddle in the detector. A neutron impinging on the LAND detector will typically cause several paddles to fire, so all available channels must be synchronised in order to reconstruct the initial position of the neutron hit correctly.
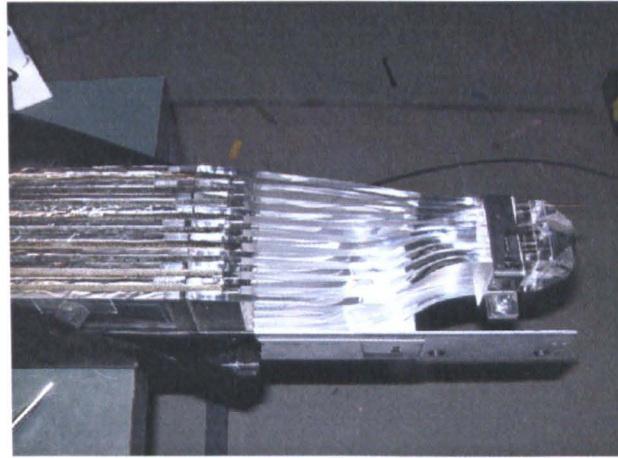
Figure 3.9: The composition of a single paddle of the LAND detector, showing alternate layers of scintillator and iron. Image taken from [93].

3.4.2 Proton Branch

The proton branch of the setup is used in the same way as the neutron branch, to detect protons emitted by decaying fragments produced in the target. The protons are first detected in two drift chambers for position measurements and subsequently in a large TOF wall (TFW) for timing purposes. If nuclei decay by emitting deuterons or tritons, which have the same Z as a proton, they will be detected by the charged fragment arm of the setup since they have an $A/Z \geq 2$. Like the neutron branch the proton branch can also be used as a trigger, allowing the rough identification of the reaction channels that involve proton evaporation with a minimal amount of information.

There are two proton drift chambers (PDC, see Fig. 3.11) each placed in front of the TFW detector. They have an active area of 100×80 cm^2 and are designed to detect protons at 500 MeV.A with a spatial resolution of 200 μm and an efficiency of 95% [94]. Each PDC contains two layers which give position information for x (144 channels) and y (112 channels). The layers are composed of conducting wires arranged in a hexagonal structure, with a so-called 'sense' wire in the centre of each hexagon. Each of the sense wires is surrounded by six 'field' wires that form the hexagonal drift cell. The PDCs are filled with an Argon/CO_2 mixture that allows the protons to ionise atoms of the gas that are then accelerated towards the sense wires by the electric field created by the 'field' wires. The PDCs are only used for measuring the positions of the protons, and in order to obtain good resolution, the position of each PDC in the laboratory must be known precisely along with its tilt angle so that the proton tracks can be reconstructed with the best possible resolution.
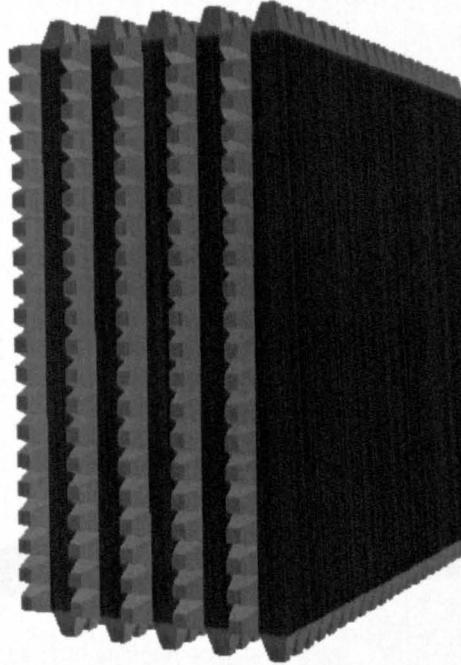
Figure 3.10: The LAND detector without its supporting structure. The active area (depicted by the black paddles only) is 2m×2m in size. Image produced using the R3BRoot Geant4 program (see chapter 6).

The large time of flight wall (TFW) detector is composed of two planes of scintillator paddles, with 14 in the horizontal direction and 18 in the vertical direction (see Fig. 3.12). The horizontal paddles each measure $189 \times 10 \times 0.5$ cm^3 and the vertical ones $147 \times 10 \times 0.5$ cm^3. As with LAND, each paddle is read out by a PM tube fixed at either end. The position of a hit can be found from the time difference between the signals recorded by a paddle. The position resolution of the TFW alone is not sufficient to track the protons and obtain their momentum, so only the timing information is used. TOF information can be taken from the TFW once all paddles and both planes have been synchronised with each other.

3.4.3 Charged Fragment Branch

Performing quasi-free scattering in inverse kinematics provides the possibility of making a measurement of both the recoiling fragment, and the knocked out cluster or nucleon, produced by the reaction. A direct comparison between the recoil momentum of the fragment, and the momentum of the knocked out cluster or nucleon could then be made.

The GFI detectors [95] (Große Fiberdetektor) are composed of scintillating fibres that cover an active area that is 50×50 cm^2 in size (Fig. 3.13). Each GFI consists of

Figure 3.11: The Proton Drift Chamber detectors with their supporting structures and a depiction of a perpendicular proton track. The distance from the base of the structure to the centre of the active area (indicated by the proton track in red) is approximately 2m.

500 optical fibres with a square cross section of 1×1 mm^2. The fibres are placed parallel to each other and are covered in a coating that is added to minimise cross-talk between neighbouring fibres, reducing the total efficiency of each detector to just below 90%. One end of the fibre is connected to a Position Sensitive PhotoMultiplier (PSPM) using a specially designed mask. Fibres are attached to the mask in a sequential way so that each has specific coordinates denoted by (u,v). The PSPM comprises a photocathode, mesh-type dynodes and the anode which consists of 18 wires in the x-direction and 16 wires in the y-direction each separated by a distance of 3.7 mm. Particles passing through the detector and striking the fibres will produce scintillation light that is picked up by the photocathode. The position of the light on the photocathode is correlated with the fibre in which the light was produced and this provides the position of the fragment in x [95]. The reconstruction routine used to obtain the x-coordinate in the laboratory from the (u,v) coordinates in the detector, is discussed in ref. [96] and an example of the output is given in chapter 4. As with the PDCs, the GFI detectors are used exclusively for position information and not for timing purposes.

The NTF (Neue time-of-flight) detector is a smaller version of the TFW detector and is used for the detection of the heavier charged fragments in the reactions. It is
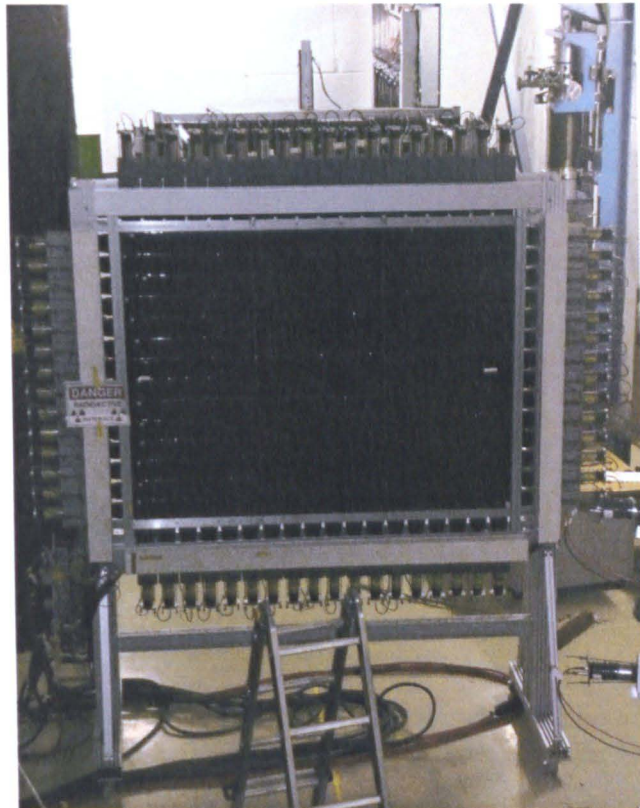
Figure 3.12: The proton TOF wall (TFW) with its supporting structure. The active area is covered to prevent noise and light that is produced by protons escaping or entering neighbouring paddles.

composed of eight horizontal and eight vertical scintillating paddles, each measuring $50 \times 6.25 \times 0.5$ cm^3. Like the proton branch, position information is taken primarily from the GFI detectors in front of the NTF. However, position information from the NTF can be used to supplement this, particularly the position of the ion in the y-direction as this is not supplied by the GFI detectors. Energy loss and TOF measurements can be extracted from the NTF detector for the identification of the ions in A and Z.

3.4.4   Tracking the Beam after the Target

Tracking for charged particles after the target is handled by a separate software program, with a dedicated tracking algorithm for protons and the heavier charged fragments (see section 4.5.2). This algorithm makes use of the positions of a particle before and after passing through the ALADIN magnetic field together with field maps of ALADIN that allow the trajectory of an ion or proton to be precisely calculated. From the positions of a particle in the magnetic field, the $B\rho$ value can be calculated (Eqn. 3.1), and used with TOF information to retrieve its A and momentum (as with the incoming tracking, see section 3.2.2).
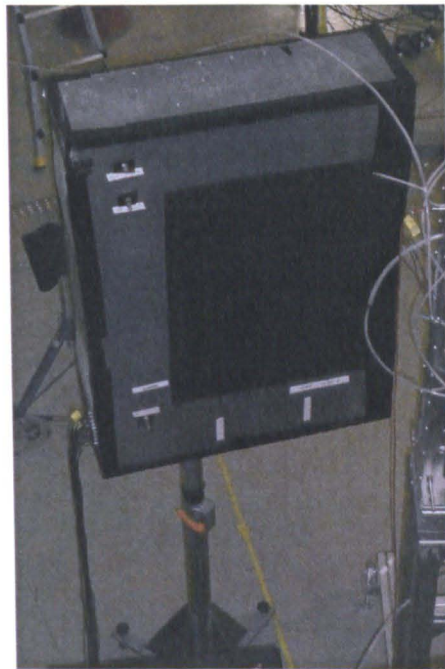
Figure 3.13: A GFI detector with its supporting structure. The active area is covered to prevent noise and light that is produced by fragments escaping.

3.5   Triggers

Logic signals from the detectors in the setup are combined to form trigger patterns that help the Data AcQuisition system (DAQ) decide whether an event should be recorded or not. They can also be used to select events of interest during data analysis. The triggers can be split into two groups, triggers 1 - 8 in Table 3.2 are the onspill or 'physics' triggers. And triggers 9 -16 are the 'offspill' or calibration triggers. Certain triggers, e.g. the minimum bias trigger that are expected to fire most often, are given a down-scale factor (DSF) so that the DAQ can process signals that are more likely to come from reactions of interest. The DSF is set by the hardware but can be checked experimentally by calculating the ratio of events with a non-down-scaled trigger, to events containing the same non-down-scaled trigger plus a downscaled one. Throughout this experiment, the minimum bias trigger had a DSF of 2^9 which was checked by calculating its ratio with events containing the non-downscaled neutron trigger: $N_{Tpat\&128}$.

$$DSF = \frac{N_{Tpat\&128}}{N_{Tpat\&129}} \sim 512 \tag{3.2}$$

Trigger bit (n)	Trigger pattern (2^{n-1}).	Trigger Name	Description
1	1	Minimum bias	Good Beam (required for accepting a physics event)
2	2	Fragment	Fragment detected in the NTF
3	4	Crystal Ball or	Single Crystal high energy threshold
4	8	Crystal Ball Sum	Crystal Ball high energy threshold
5	16	Proton	Hit in TFW
6	32	Good Beam - Pileup	Used for removing events where pile-up occurs
7	64	Pix	Hit in the pixel detector (only for pixel runs)
8	128	Neutron	Hit in LAND
9	256	Crystal Ball Muon	Offspill trigger for detector calibration
10	512	LAND Cosmic	Offspill trigger for detector calibration
11	1024	TFW Cosmic	Offspill trigger for detector calibration
12	2048	Crystal Ball Gamma	Gamma ray threshold
13	4096	Clock	Used for determining the pedestals in the QDCs
14	8192	Time Calibrator	Used for calibrating the TDCs
15	16384	Begin of Spill	Given by the accelerator
16	32768	End of Spill	Given by the accelerator

Table 3.2: A summary of the hardware triggers used for the s296 experiment.

Chapter 4

Calibrating the Setup

This chapter describes the procedures used to calibrate the various detectors in the LAND/R^{3}B setup so that measurements for a particular reaction channel can be made. Precise internal calibration and synchronisation of detectors with others in the setup is necessary for the tracking of particle trajectories through the setup and the extraction of physical quantities such as Z, A and momentum. The main stages of calibration are carried out within the *land02* framework [97] which has been successfully used to analyse several experiments with the LAND/R^{3}B setup. Stages of reconstruction that are not yet available within this framework are carried out using separate algorithms and the ROOT data analysis program [98]. ROOT is also used for the final reconstruction of some physical quantities and for producing graphical outputs.

4.1 Calibration levels within the *land02* Framework

Reconstruction is carried out on an event-by-event basis beginning with the electrical signals received by the Data Acquisition system (DAQ) from the various detector modules before moving towards TOF, ΔE and (x, y, z) measurements for each particle as it passes through the setup. Fig. 4.1 gives an overview of how events are reconstructed by the *land02* framework. Data files can be 'unpacked' for two different reconstruction levels at the same time, allowing the user to check the calibration and reconstruction procedures carried out by the program.

4.1.1 The RAW Level

The *land02* analysis framework begins by accepting raw data from detectors before beginning any reconstruction. These data consist of the electrical signals read out from modules with appropriate time delays that are then recorded by the DAQ for each accepted event. These electrical signals are mapped onto their appropriate detectors and stored as integers.
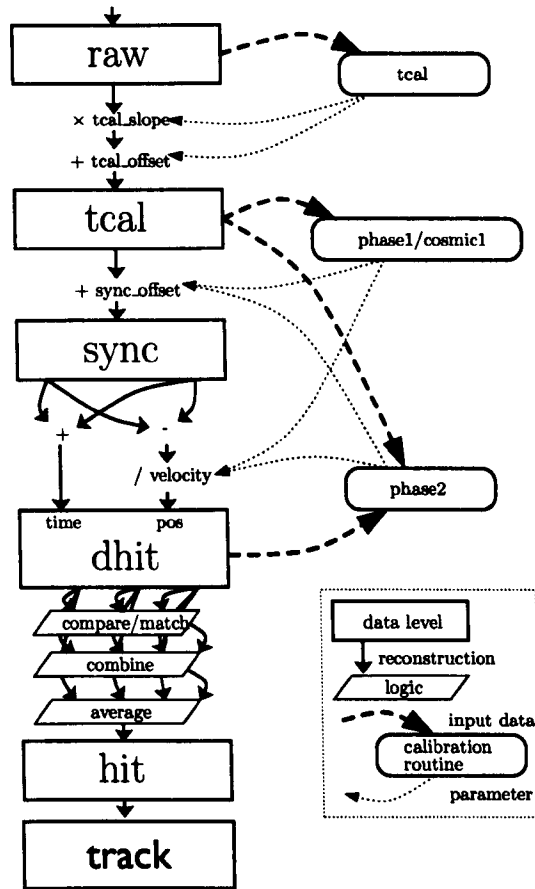
Figure 4.1: Calibration levels within the *land*02 framework. In order to move from the *hit* to the *track* level of calibration, detectors must be synchronised with each other as discussed in section 4.4. Figure adapted from [99].

4.1.2 The TCAL Level

To move from the RAW level to the TCAL[1] level, some adjustment of the times and energies received from each hit is needed. Firstly the TDC that is used to provide a constant clock signal throughout the experiment is used to calibrate the time signals relative to this scale so that all time signals are in *ns*. Secondly the 'pedestal' (see section 4.2) that is recorded by the QDC along with every energy loss signal is subtracted, so that all energy signals have their zero value appearing at zero on the energy scale which is given in channels. Each event is now in floating point form.

---

[1]The TCAL level takes its name from the time calibration procedure that it performs, however, it is important to remember that pedestal subtraction (energy) is also carried out.

4.1.3 The SYNC Level

The SYNC level is used by detectors that are modular. This enables all of the modules (e.g. crystals of the Crystal Ball) within a detector to sychronise with each other so that they deliver consistent information for an event that can be correlated with information from other detectors in the setup. Gain factors for each module are used to gain match energy signals, so that the detector can deliver energy loss signals in MeV, and offsets are applied to ensure that all time signals will have a common zero.

4.1.4 The DHIT Level

At the DHIT level, the positions of hits are calculated from the energy loss and time signals of a particle as it passes through the detector. These positions are given in detector specific coordinates (e.g. strip no. for the DSSSDs) rather than in laboratory coordinates. A translation from these DHIT coordinates to the laboratory coordinates will not always be a linear transformation (e.g. PSP Silicon Detectors [85]). From this point on in the reconstruction most of the quantities have an associated error reflecting the precision with which the position of the hit is known.

4.1.5 The HIT Level

Events reconstructed to the HIT level now have their positions given in a standard right-handed coordinate system which has the centre of the active area of a detector as its origin. Each event has energy loss in MeV, time in ns and positions in cm. The event information is delivered in this way so that the tracking routines can operate without detector dependence.

4.1.6 The TRACK Level

The TRACK level of calibration is where the measurements made for each event by the individual detectors are linked up into tracks that describe the trajectory of a particle passing through the setup, without reference to the detectors themselves. The tracking first requires that the signals present in the separate detectors that could belong in the same track be grouped together, correlating for example a fragment and its knocked out cluster along with any γ rays that they emit. Secondly, a function is fitted to the data so that a track can be determined, and measurements such as mass and momentum can be extracted for each particle.

4.2   Time and Energy Calibration of all Channels

During the experiment all detector channels that are read out by a TDC have their gain monitored by a clock signal that creates events with discrete known times at regular intervals throughout the experiment. This allows an accurate conversion of the time measured in channels to the time measured in ns, since the number of ns/TDC bin may fluctuate slightly over the course of the experiment.

All detector channels read out by a QDC will contain a small amount of energy even when no event has occurred. This is known as the 'pedestal' and its mean value for each channel is determined and subtracted by the *land*02 program at the TCAL level (see 4.1.2 above).

Throughout an experiment, calibration parameters for time, energy and position will vary due to dependencies of the detectors for example on temperature and power fluctuations. It is useful therefore, to monitor the fluctuation of a given parameter as a function of time. This gives an idea of which particular detectors, channels or modules are likely to generate problematic results later on, as well as allowing time-dependent corrections to parameters to be applied, see for example Fig. 4.2.

4.3   Internal Calibration of Detectors

The goal of internally calibrating a detector is to ensure that it delivers one time and one energy value for every hit on the detector as well as a position for each hit given in terms of the detectors structure e.g. fibre number for the GFI detectors. For detectors made up of PM-tubes and scintillating paddles this will mean taking a sum (for energy loss) or average (for time) of the two tubes on one paddle and then gain matching all of the paddles on both planes together to ensure that a particle passing through both planes and hence more than one paddle does not produce a different set of signals in each. Many of the detectors in the setup have a similar structure and thus their calibration routines are similar. For this reason some general calibration procedures are discussed first, before consideration of specific detectors where the calibration requires more unique and detector specific procedures to be applied.

4.3.1   Calibration of Plastic Scintillator Detectors

When a charged particle passes through a plastic scintillator paddle it will deposit some of its energy proportional to its charge. The energy deposited will generate light within the scintillator that will travel along the paddle to the PM-tubes at either end, where the time and amplitude (energy) of the signal will be recorded for the hit as shown in Fig. 4.3.
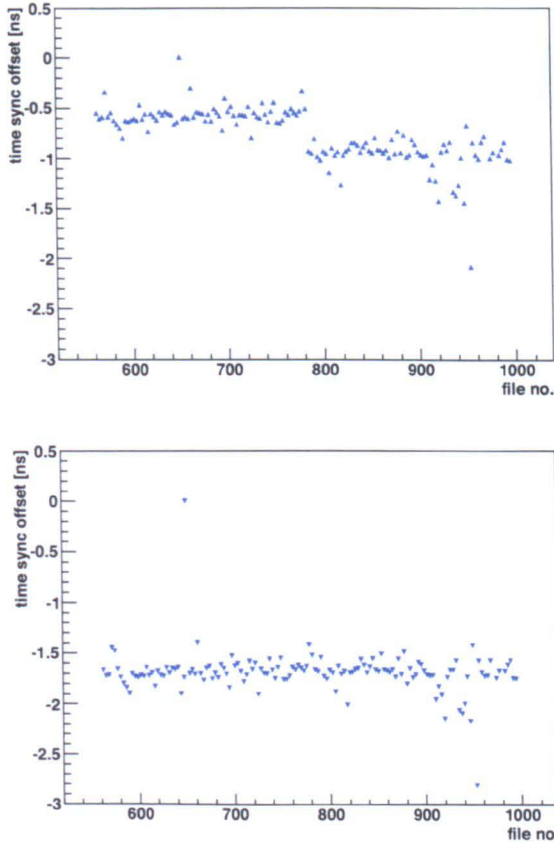
Figure 4.2: The fluctuation of the LAND time synchronisation offset parameter as a function of file number. The bottom figure shows data for paddle no. 27 of LAND and is clearly distributed around a mean value not requiring significant correction. The top figure shows data for paddle no. 26 of LAND and has a distribution that will need correction. Data points on both plots that lie a long way from the mean value for the parameter are due to low statistics for that particular file.

The times measured at each of the PM-tubes, t_1 and t_2 are given by:

$$t_1 = t_0 + \frac{x_1}{v} + c_1 \qquad (4.1)$$

$$t_2 = t_0 + \frac{x_2}{v} + c_2 \qquad (4.2)$$

where v is the speed of light in the paddle and the constants c_1 and c_2 are offsets due to cabling and electronics etc. To obtain the time t_0, an average of the two times can be taken:

$$t_0 = \frac{t_1 + t_2}{2} + t_{offset} \qquad (4.3)$$

48
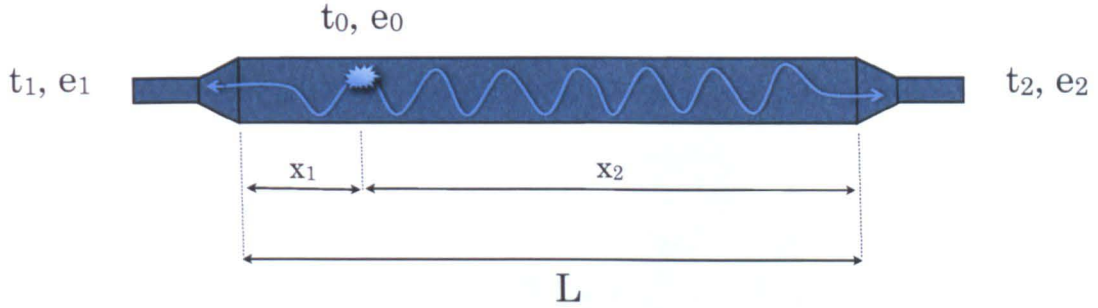
Figure 4.3: Depiction of an event occurring in single scintillator paddle. As the particle passes through the scintillator paddle time and energy signals are recorded at each end. The energy recorded by the PM-tubes depends upon the position of the hit in the paddle.

This is not dependent upon the position of the hit and the constant t_{offset} can be determined by synchronising the detector as discussed in the later section 4.4.

The energies measured at each of the PM-tubes, e_1 and e_2 are given by:

$$e_1 = e_0 \cdot exp\left(\frac{-x_1}{\lambda}\right) \tag{4.4}$$

$$e_2 = e_0 \cdot exp\left(\frac{-x_2}{\lambda}\right) \tag{4.5}$$

where λ is the light attenuation length in a paddle. The energy e_0 is given by:

$$e_0 = \sqrt{e_1 e_2 \cdot exp\left(\frac{x_1}{\lambda} + \frac{x_2}{\lambda}\right)} = exp\left(\frac{L}{2\lambda}\right) \cdot \sqrt{e_1 e_2} \tag{4.6}$$

where L is the total length of the paddle and λ is a constant which, like the t_{offset} term in Eqn. 4.3, can be determined when gain factors are deduced during the calibration procedures.

The TOF walls used in the LAND/R^{3}B setup all have more than one plane. This allows multiple time and energy signals to be recorded for the same event as well as providing position measurements in x and y (and z in the case of LAND). Since both time and energy signals can be used to obtain the position of the particle, the TOF walls are 'over-determined' detectors - providing more information than is necessary. This is useful firstly because it allows the reconstruction routines to choose the best signals to reconstruct the hit, and secondly because if a particle does not leave a complete set of signals (perhaps because of low Z), reconstruction may still be possible. The average time of a hit passing through two perpendicular paddles (Fig. 4.4) is given by:
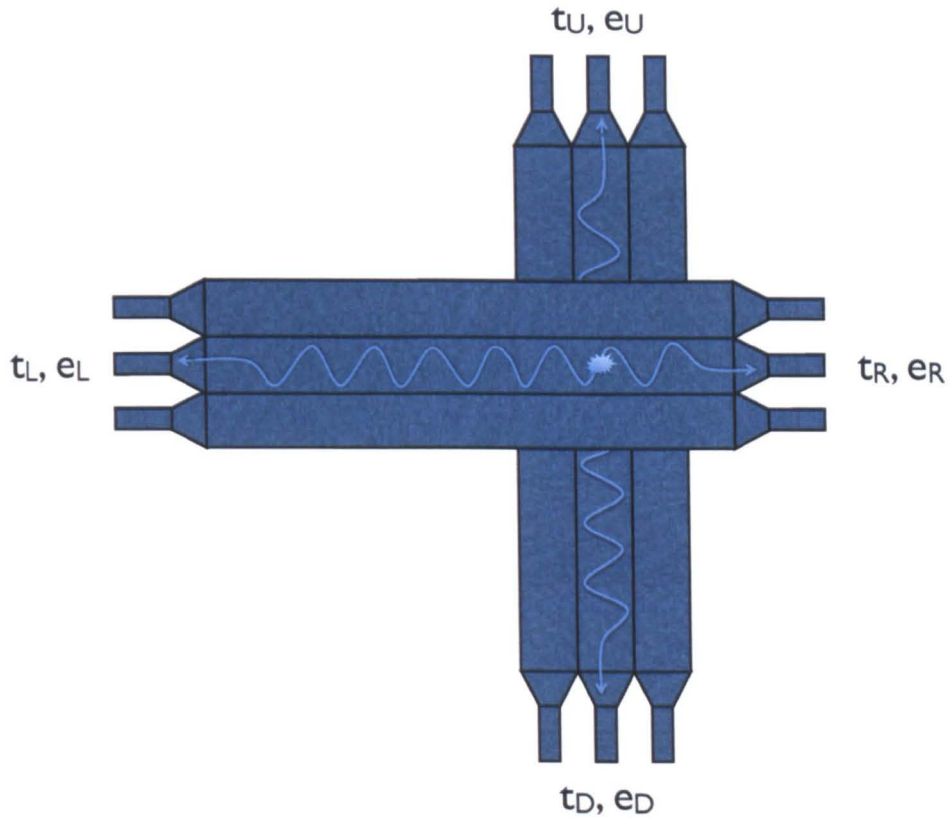
Figure 4.4: Depiction of an event occurring in two crossed scintillator paddles. The particle is shown firing the horizontal paddle in the x-direction and the vertical paddle in the y-direction allowing two pairs of time and energy signals to be recorded.

$$\bar{t}_{xy} = \frac{t_L + t_R + t_U + t_D}{4} \tag{4.7}$$

The corresponding energy deposited by a particle passing through the same configuration is given by:

$$\bar{e}_{xy} = \frac{\sqrt{e_l\, e_r + e_u\, e_d}}{2} \tag{4.8}$$

This quantity will later be used to calculate the Z of the ion.

Using TOF walls with more than a single plane also makes a kind of 'self calibration' possible. When a particle passes through both planes *i.e.* through two perpendicular paddles, the position of the hit is constrained to an area within the paddle width in both x and y. Plotting this position information against the actual position determined

from the time difference or the energy difference allows calibration factors for each paddle to be determined. Time offsets and energy gain factors are then determined such that a hit in the centre of a paddle results in a time and energy difference of zero. Once all paddles and planes are synchronised together in time and energy, the internal calibration steps for that detector are complete.

The time resolution for a plastic scintillator based detector with paddles and planes, can be estimated by looking at the time difference between the planes for the same hit. This can be used for online monitoring of the detector during an experiment and calculated using Eqn. 4.9. This resolution is shown in Fig. 4.5 for the NTF detector.

$$t_{res} = \frac{t_L - t_R}{2} - \frac{t_U - t_D}{2} \tag{4.9}$$
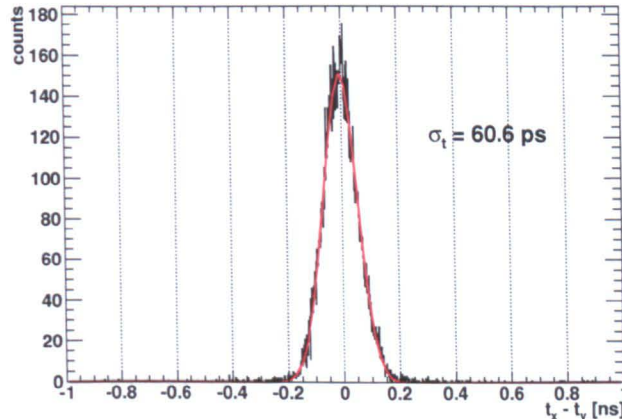
Figure 4.5: The time resolution of the NTF detector measured for ^{12}C ions impinging on a 2.31 mm thick CH_2 target at 400 A.MeV. The overall resolution achieved from combining PM-tubes is better than their individual resolution [85].

4.3.2 The POS Detector

The POS detector is used as the common start for the time measurements of all particles that enter the setup. It is necessary to synchronise its four photo-multiplier tubes so that an average can be taken as the start time for each event. Because POS is a single plane of square scintillator, calibrations that are necessary for the other scintillator-based detectors are not needed. The TOF resolution obtained for fragments travelling between the POS and NTF detectors is shown in Fig. 4.6.

4.3.3 The DSSSDs

The DSSSDs could be considered the most complex detectors being used in the current LAND/R^{3}B setup. This is due mostly to the high number of modules (strips) that have
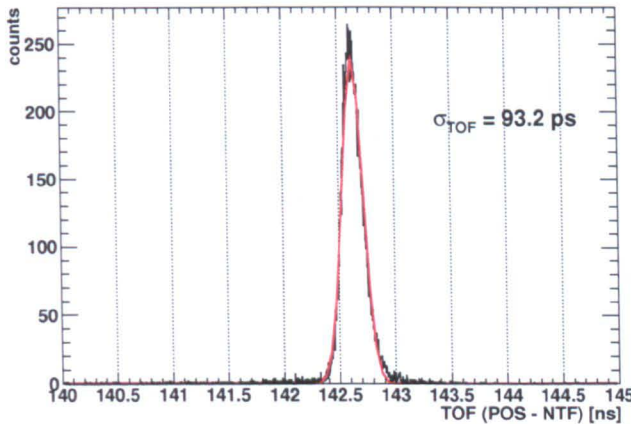
Figure 4.6: The time of flight resolution for fragments between the POS and NTF detectors measured for ^{12}C ions impinging on a 2.31 mm CH_2 target at 400 A.MeV.

to be calibrated and synchronised with each other and also the fact that all channels must be continually read out during an experiment since the distinction between noise and low energy particles such as protons can often only be discerned by analysis offline. This results in very large quantities of data that must be processed. However once carefully adjusted and calibrated they can provide very precise information on the energy and angle of particles emitted from the target during a reaction. Each of the DSSSDs is linked to a chain of front-end electronics that uses VA64 chips from IDEAS, Norway [100, 101]. The signals are then fed out from these chips into NIM modules known as SIDEREMs (SIlicon DEtector REadout Modules) that have been developed by GSI to digitise the signals and perform pedestal and common noise subtraction [102]. Monitoring the pedestals of each strip during an experiment is a way of checking which strips are active and of checking the overall performance of the detector. Each detector can also be recognised by the shape of its pedestals, which will differ because of the varying amounts of electronic noise in its readout modules and the number of dead strips present in the detector itself. An example of the pedestal distribution for two different detectors is shown in Fig. 4.7.

When an ion passes through a DSSSD the number of strips that will fire depends upon the Z of the ion (Eqn. 4.11). This means that in order to get the energy loss of any particular ion, all of the strips that received energy from it must be summed together. This has been carried out successfully in other experiments by defining a cluster of strips and a Centre of Gravity (CG) for each hit from which a total energy loss and position can be determined [103]. Care must be taken to define the best criteria for separating strips that belong to a cluster from strips that contain noise [91]. For this experiment the criteria are as follows: firstly, at least one strip in the cluster must
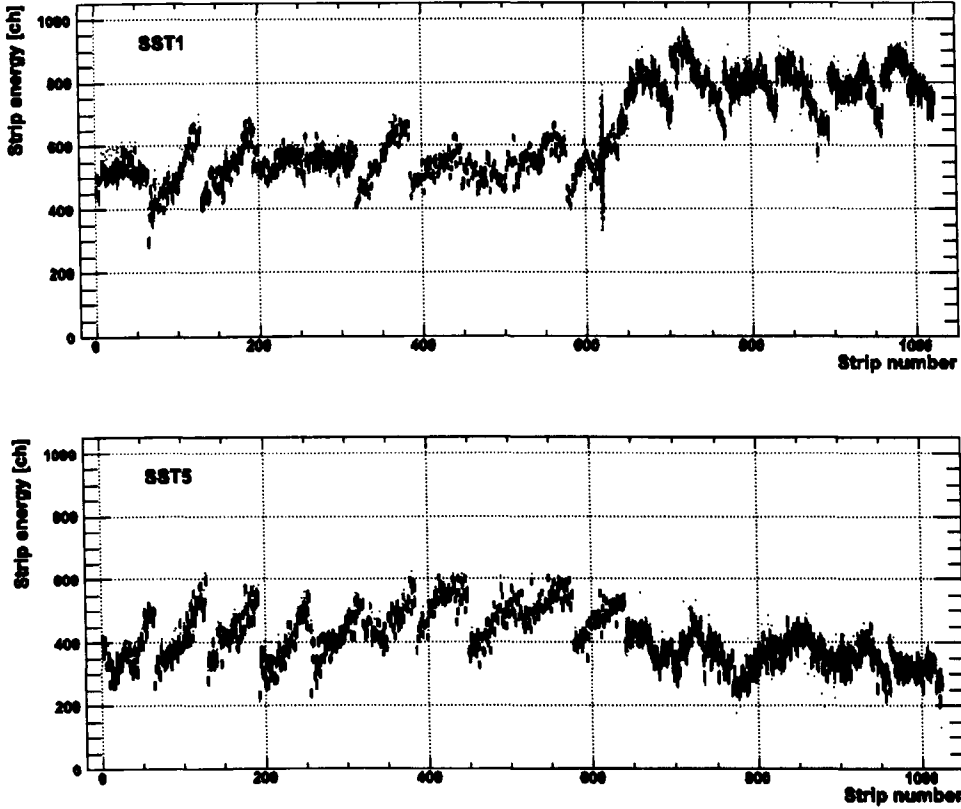
Figure 4.7: The pedestals for the first and fifth DSSSDs situated at the top and bottom of the box surrounding the target. Gaps and distortions can be due to dead strips and electronic noise making the pedestal distribution for each DSSSD different.

have an energy $\geqslant 4\sigma$ of the pedestal and secondly, all surrounding strips that are added to the cluster must have energies $\geqslant 1\sigma$ [97].

This 'summed' energy will need to be corrected for several effects including the inter-strip hit position and the gain of the individual strips and their amplifiers. The correction for the position of the hit relative to a read-out strip is known as the η-correction and can be calculated as the decimal part of the CG expressed as follows:

$$CG = \frac{\sum_i^S s_i \times q_i}{Q} \tag{4.10}$$

where q_i is the charge deposited in strip number s_i and the total charge deposited by an ion in the detector is Q. Since the position of the detectors with respect to the target and the pitch of the strips is known, combining this with the position of the cluster given by the CG calculation allows the position of the hit in the laboratory to be determined. The η-distribution reflects the dependence of charge collection on the position of the hits in the readout gap. It ranges (theoretically) from 0 to 1 where 0

53

is exactly on the left strip and 1 exactly on the right. Integrating the η-distribution allows position to be determined as a function of η improving the position resolution of the detectors to sub-strip pitch values [104–106]. The electronic VA chips for each DSSSD each process 64 channels. These chips must be gain matched so that the groups of strips do not generate different signals when ions with the same Z and β values pass through them. Strips positioned close to the border of the VA chips can often experience a distortion that manifests itself as a spike in the energy distribution of the DSSSD. Careful gain matching can reduce this effect, minimising the amount of events that will be given wrongly assigned position and energy values. All corrections with the exception of correcting for dead strips are only necessary for the two DSSSDs that form the end-cap of the box and are placed directly in the beam. In order to carry out the corrections, data are selected from an empty target run so that the ions passing through each strip can be expected to deposit the same energy without the straggling that is introduced by a target. If a secondary beam is used instead of a primary beam, a single isotope must be selected using the PSP detectors since the η-correction is Z dependent. The correction for the ^{12}C beam used in this analysis is illustrated in Fig. 4.8 and the resulting charge separation for fragments is shown in Fig. 4.9.

It is important that the alignment of the DSSSDs is known to a high precision, so that the tracks and angles of particles emerging from the target can be obtained with the best possible accuracy. The position of each of the DSSSDs with respect to the target centre must be known to within several μm in order for the positions to be extracted with a precision an order of magnitude higher [103]. This alignment is carried out using optical measurements and recorded in technical drawings made prior to the experiment. Further alignment is carried out during the analysis by comparing the position of ions in a detector with the positions predicted from their trajectories in surrounding detectors. This allows suitable offsets to be calculated and applied improving the position uncertainty of individual detectors down to several microns.

4.3.4 Crystal Ball γ-Readout

The radioactive γ-ray sources: ^{88}Y and ^{22}Na were used for taking data before and after the experiment for the calibration of the γ-readouts of the Crystal Ball. It is not practical to monitor whether the Crystal Ball parameters fluctuate over the course of the experiment, but having these two sets of data for calibration allows a check to be made, and if necessary two separate calibrations can be used, depending on whether a run is closer to the start or the end of the experiment. Using the γ rays of 511, 898, 1275 and 1836 keV from both sources, each crystal can be individually calibrated to the same energy values. The procedure for obtaining the parameters is illustrated for
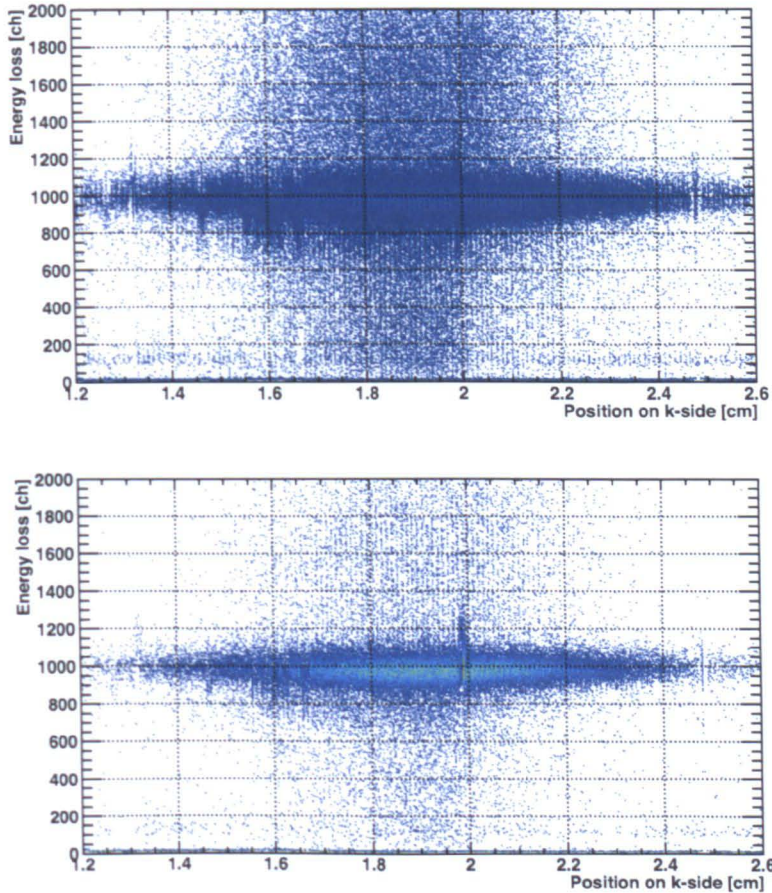
Figure 4.8: An illustration of the η-correction applied to SST3 k-side for events from an empty target run. Both plots show the energy loss of 400 A.MeV ^{12}C ions as a function of position. The first plot is for events without the η-correction applied, distortions and broadening of the energy resolution are apparent. The second plot is with the η-correction applied and dead strips removed resulting in a much better energy resolution and less distortion.

a typical crystal in Fig. 4.10 and Fig. 4.11. Firstly, the known energy peaks from the sources are fitted, secondly these energy values in channels are plotted against their energy in MeV so that a linear fit can be made through these points (Fig. 4.12). Finally, the slope and the offset of the linear fit for each crystal are stored as experiment-specific parameters that are used for energy reconstruction. A check of the calibration can be made by plotting the spectra of each crystal on top of each other to check the alignment.

4.3.5 Crystal Ball High Energy Readout

The high-energy readouts of the Crystal Ball (used by the front 2π of the detector only) need to have a separate energy calibration to the γ readout since high energy particles
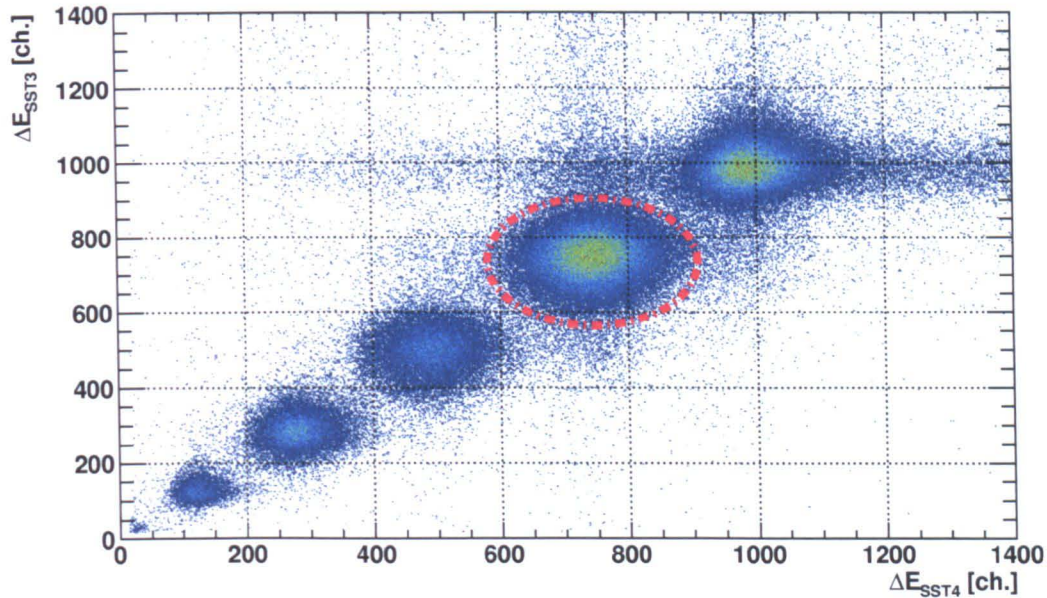
Figure 4.9: The energy loss of fragments in the k-side of SST3 and the k-side of SST4 for CH_2 target events. The multiplicity in each DSSSD is one, and the Crystal Ball sum trigger has been selected. The $Z = 5$ events are shown in the red ellipse.

such as protons can be emitted from a reaction with energies up to the beam energy, and the γ calibration cannot be reliably extrapolated beyond a few tens of MeV. Cosmic ray muons passing through the Crystal Ball and triggering crystals on opposite sides can be used to synchronise the crystals at an energy of approximately 85 MeV. However, in order for this to act as an energy calibration for high energy protons, a 'quenching' factor will be needed since the light production from a muon passing through the crystal will not be the same as for a proton. Additionally, the majority of protons with an energy above $\sim$270 MeV are not fully stopped by the NaI crystals, preventing a full energy measurement. This happens particularly at low angles relative to the beam axis, and a correction that allows their full energy to be reconstructed will be necessary in order to obtain a complete energy calibration. Fig. 4.13 shows proton energy loss in the Crystal Ball against polar angle from the DSSSDs. Protons with an angle less than $\sim$50° do not deposit their full energy in the Crystal Ball. The response of the Crystal Ball to these high energy events is discussed further in chapter 6.

4.3.6 Proton Drift Chamber Calibration

The Proton Drift Chambers provide a measurement of the x and y positions of protons after the ALADIN magnet. In order to do this, the positions of hits inside the drift chambers are obtained by converting 'drift times' to 'drift lengths'. To make this
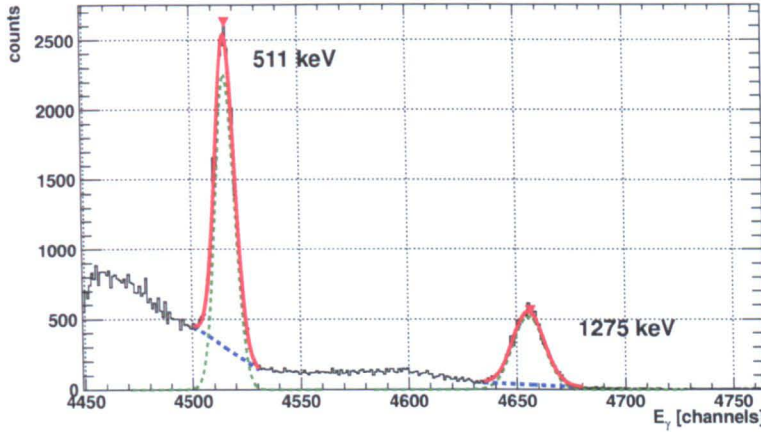
Figure 4.10: The ^{22}Na γ-ray spectrum for crystal 159 of the Crystal Ball detector. The energy resolutions are: $\sigma_{511} = 4.76$ % and $\sigma_{1275} = 3.09$ %.

conversion, events are selected for calibration that allow a so called rt-curve to be constructed. This rt-curve plots the drift times as a function of the drift lengths which run from 0 mm up to a maximum distance of 6.92 mm, the size of each drift cell. Hits throughout this range are all equally likely and only hits that pass through both planes of the detector and through two cells in each layer are selected. Additionally, the track of the proton must be perpendicular, this can be determined by summing the distance from the track to the sense wires. If the track is perpendicular, the distance should always add up to 6.92 mm, see Fig. 4.14 below. In order to determine the rt-curve, a simulation was carried out in the Garfield simulation program [107] which was then fitted to the experimental data [94].

4.3.7 GFI Detectors

Each fibre of the GFI detectors is connected to a 'mask' which is in turn connected to a single PM-tube as discussed in chapter 3. Once the pedestal subtraction has been performed, the remaining calibration of the GFIs is done using a sweep run, where the settings of the ALADIN magnetic field are gradually changed so that the primary beam passes over the entire active area of the detector. This illuminates each fibre so that its response and gain factor can be determined, as well as a measurement of its position with respect to other fibres. The positions of the fibres before and after the gain matching calibration are shown in Fig. 4.15.
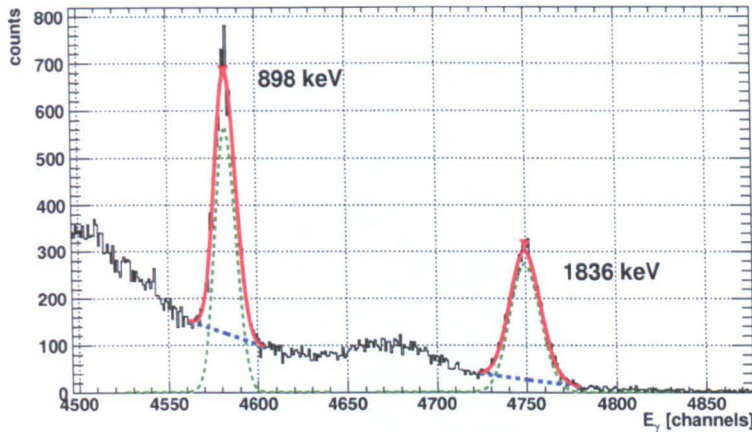
Figure 4.11: The ^{88}Y γ-ray spectrum for crystal 159 of the Crystal Ball detector. The energy resolutions are: $\sigma_{898} = 3.58$ % and $\sigma_{1836} = 2.57$ %.
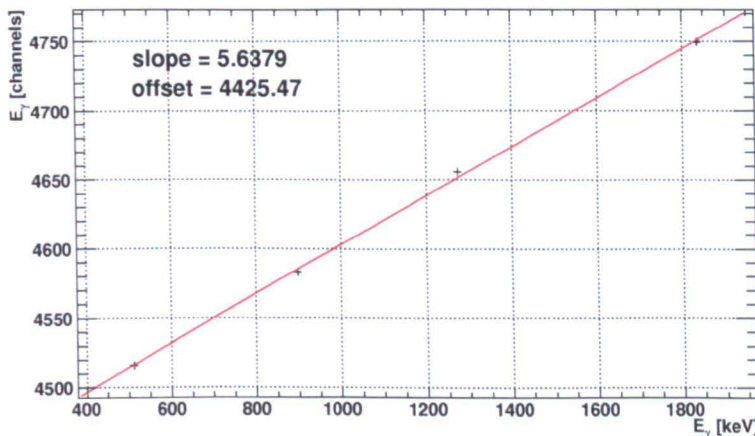
Figure 4.12: The γ-ray energy calibration fit for crystal 159 of the Crystal Ball detector.

4.4   Synchronisation of the Detectors

In order to be able to reconstruct tracks of particles through the setup, the signals from different detectors must be correlated together for each event. Once the different detectors are calibrated and internally sychronised by the various procedures that have been described, they must be synchronised with each other. For timing information, this involves adding 'global offsets' to each detector, so that all timing information is given with respect to the POS detector in *ns*, acting as a common start for all other detectors and for all events. For information on the energy of particles passing through the setup, conversion factors are applied to change from channels to MeV and more importantly, from channels to Z. For position information, the precise locations
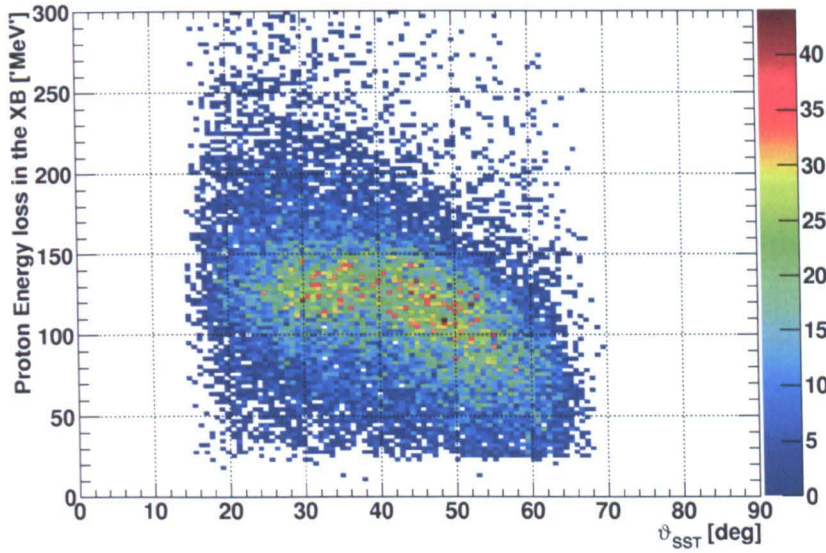
Figure 4.13: Proton energy loss measured in the Crystal Ball as a function of proton polar angle (ϑ), measured in the DSSSDs for ^{12}C($p, 2p$)X events. The proton energy loss in the Crystal Ball is calibrated to MeV using cosmic ray muons and the polar angle of the protons is measured with respect to the beam axis.

of each of the detectors relative to the target centre must be specified in order for reconstruction algorithms to calculate TOF and momentum correctly. These positions must be specified to an accuracy that is less than the spatial resolution of the detectors themselves. Fig. 4.16 shows the γ ray and neutron events that appear in the first plane of LAND for a run with a CH$_2$ target. This clear separation between the γ rays and the neutrons is used to find the global time offset of LAND since its distance from the target is known and thus the TOF for the γ-ray events can be calculated.

4.5 Fragment Identification

After the target, unreacted ^{12}C ions and charged fragments produced in nuclear reactions with the target are passed through the ALADIN dipole magnet which separates the fragments by their A/Z ratio. Measurements of Z, position and TOF are made before and after the ALADIN magnet and can be processed using tracking routines to calculate the A, and momentum values of all particles as described by Eqn. 3.1. Knowing the A and Z of ions before and after the target allows events that have undergone nuclear reactions of interest to be selected. Tracking through the ALADIN magnet depends upon knowledge of the magnetic field which is stored in the form of field maps that can be used to determine the trajectory of a charged particle.
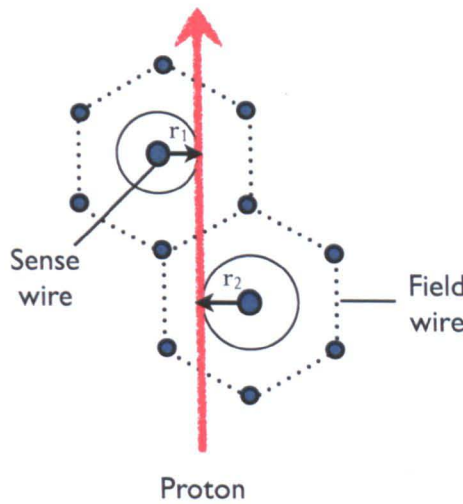
Figure 4.14: A proton event passing perpendicularly through two cells in a Proton Drift Chamber. The distances r_1 and r_2 will always sum to the drift cell length of 6.92 mm.

4.5.1   Fragment Charge Identification

All ions transported to Cave C are fully stripped of their electrons so that only their nuclear charge is measured. At relativistic velocities, the energy loss of an ion as it passes through a material is given by the following version of the Bethe-Bloch formula:

$$-\frac{dE}{dx} = \frac{4\pi}{m_e c^2} \frac{nZ^2}{\beta^2} \left(\frac{e^2}{4\pi\epsilon_0}\right)^2 \left[ln\left(\frac{2m_e c^2 \beta^2}{I(1-\beta^2)}\right) - \beta^2\right] \tag{4.11}$$

where Z, β and E are the atomic number, velocity and energy of the projectile. The distance travelled is x, through a material with electron number density n and mean ionisation potential I. The charge and rest mass of the electron are given by e and m_e respectively, and the other terms are fundamental constants. For small Z ranges as in this experiment, approximations for converting from energy loss (ΔE) to Z can be made such that:

$$\Delta E = kZ^2 \tag{4.12}$$

Precise calculations of Z are not necessary since the values calculated will only be used to select events for the final analysis and nominal values of Z are used in all further calculations of physical quantities. A typical charge distribution for CH_2 target data is shown in Fig. 4.17.

4.5.2 Fragment Mass Identification

In order to obtain the mass and momentum of fragments after the target, the tracking algorithm [97] takes the position measurements of the particles before and after passing through the magnetic field along with their β value and a nominal Z value from the NTF detector. The β value should be measured with the most precision since unlike A and Z its actual value is used in reconstructed quantities such as the invariant-mass of an event (see Eqn. 5.10). The β value of an ion or proton can be measured in two ways, firstly if the incoming β value of a particle is known as it enters the setup (from the SIS or FRS scintillators), then this velocity can be used as the 'calculated' β value of the particle. Secondly, if a detector at the start of the setup e.g. the POS scintillator can be used to supply a 'start' signal for the particle, and another detector after the ALADIN magnet e.g. NTF, TFW or LAND can be used to supply a 'stop' signal, these values can be subtracted from each other and combined with the flight path of the ion (given by the positions of the particle in the tracking detectors) to give the 'measured' β value of the particle. Knowing the β for a particle in both these ways provides additional information that is useful if there is a discrepancy between the A value of an event and its measured trajectory through the detectors. If this is the case, then the better of the two β values can be selected such that the A value is adjusted and the particle stays on its measured track.

Tracking for protons through ALADIN is always done in reverse (i.e. backwards tracking towards the target) as this minimises the uncertainty on the assignment of the track in the DSSSDs, thus allowing its momentum to be reconstructed with the least ambiguity. The energy resolution of the DSSSDs and the electronic noise that is present both in these detectors and in the proton drift chambers make the assignment of the proton track more difficult than with the fragment tracks. In addition, the spatial separation of a fragment and proton from the same event is often small, making the energy loss signals difficult to separate. If several tracks through the DSSSDs are possible then the one with the lowest χ^2 value is selected.

For neutrons produced at the target, the tracking is simpler and handled within the *land02* framework. Since neutrons are not deflected by the magnetic field of ALADIN, the position of a neutron hit in LAND together with the distance of the detector and the TOF of the neutron is used to calculated its momentum.

During the experiment the settings for the ALADIN magnetic field can be changed in order to move the position of the beam and the fragments on the detectors. However, the settings will usually remain at the same value once all calibration runs have been done and all detectors checked so that for the majority of an experiment nothing is changed significantly. The strength of ALADIN's magnetic field is needed by the

tracking routines to calculate the mass from the field maps. A value for the magnetic field strength (equivalent to 1.3 T for most of the s296 experiment) is recorded on each runsheet and the tracking algorithm is given the appropriate value in order to calculate the best possible value for the mass. Final adjustments and improvements to the mass resolution can be made by making small adjustments to the positions of detectors, or by varying the field slightly. As with Z, only nominal values of A are used in the final stages of the analysis to give the best possible resolution for reconstructed physical quantities. A typical mass distribution for CH_2 target data is shown in Fig. 4.18.
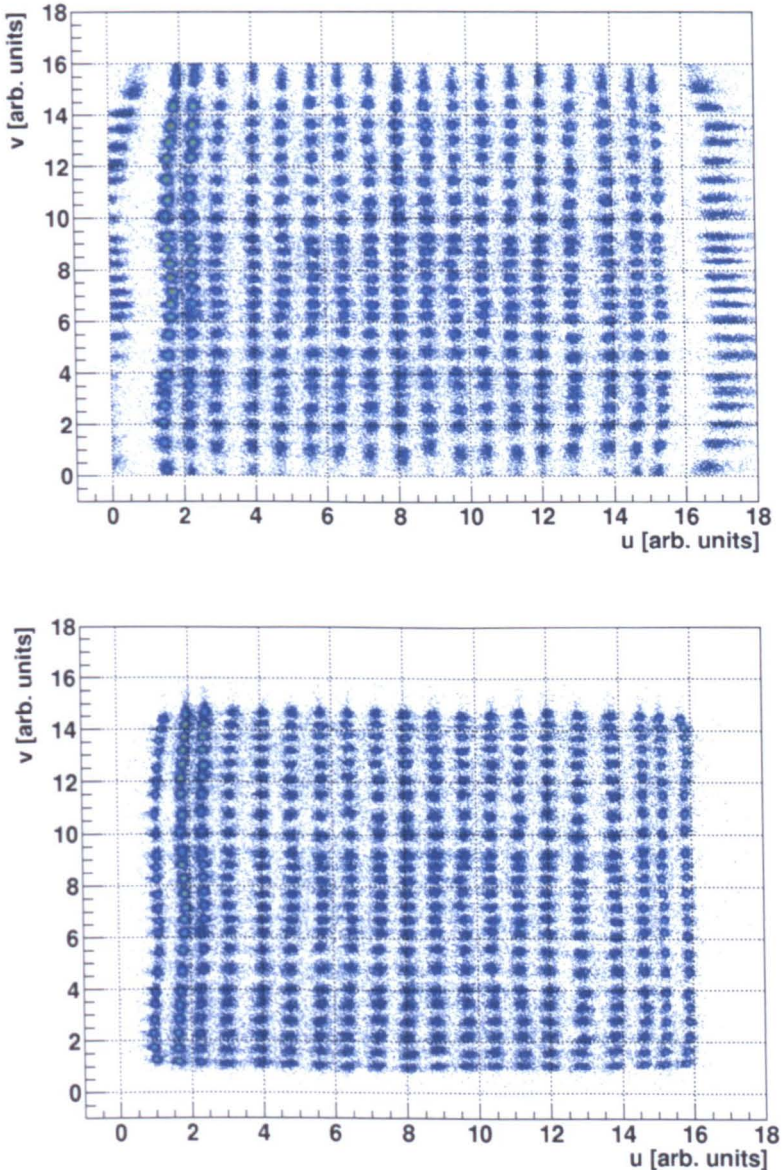
Figure 4.15: The position of the fibres in the second GFI detector before and after calibration. The detector has been illuminated with a sweep run and all fibres can be seen with distortions present especially towards the edges. Positions are given using the internal detector co-ordinates (u,v) used during the DHIT level of reconstruction which will be transformed to fibre numbers at the HIT level. Each of the fibres cover 1mm creating a total active area which extends $\sim$50 cm in x.
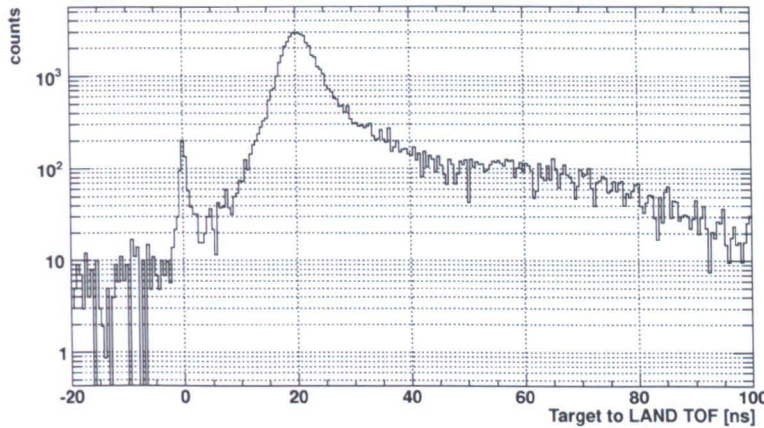
Figure 4.16: Target to LAND TOF spectrum for all events detected in the first plane of LAND. The data shown is for a CH_2 target run with the Crystal Ball sum trigger selected. The empty target background contribution has been subtracted to ensure that the peak positioned at zero contains only γ-ray events that originate from the target. These events are measured with a resolution: $\sigma_{tof} = 572$ ps and the neutron peak can be seen with its maximum at $\sim$20 ns.
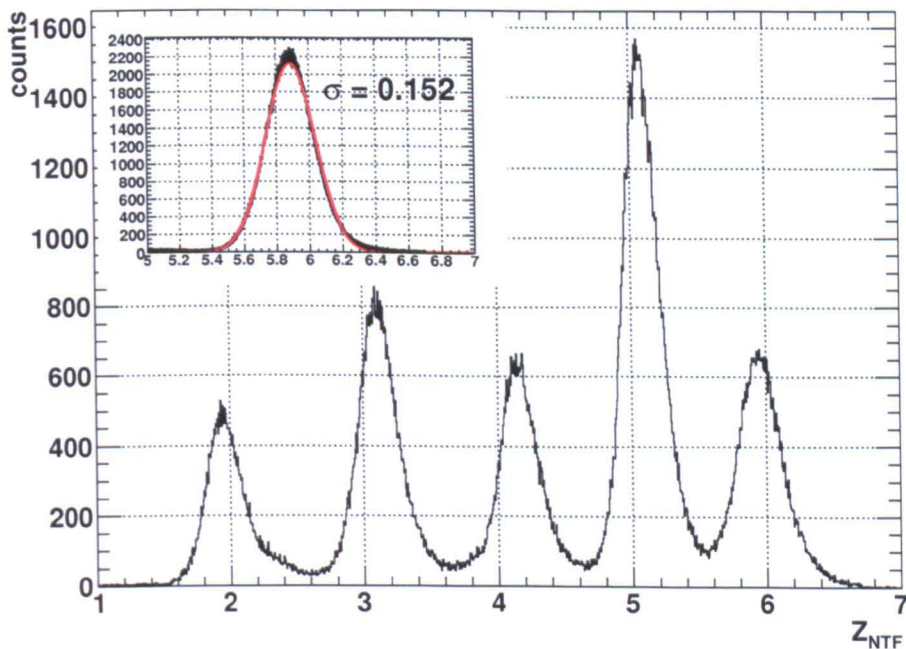
Figure 4.17: The charge spectrum of the NTF detector for reacted and unreacted beam events with CH_2 target data. The reacted beam events are shown in the main figure and selected with the Crystal Ball sum trigger. Unreacted beam events are selected with the Minimum Bias trigger and are shown in the inset of the figure and fitted with a Gaussian distribution.

64
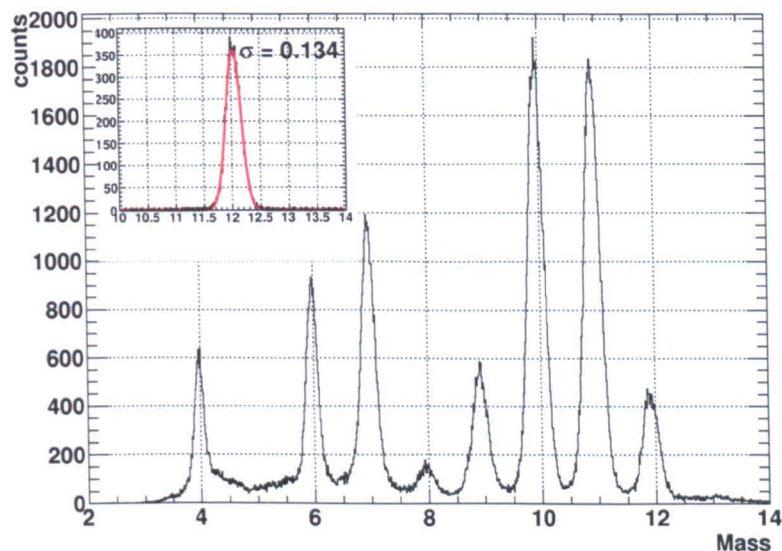
Figure 4.18: The mass spectrum for reacted and unreacted beam events with CH_2 target data. The reacted beam events are shown in the main figure and selected with the Crystal Ball sum trigger. Unreacted beam events are selected with the Minimum Bias trigger and are shown in the inset and fitted with a Gaussian distribution.

Chapter 5

Analysis Methods and Results

In this chapter, the analysis techniques and concepts that have been used to identify the reaction channels of interest, measure their cross sections, and extract physical quantities relating to the momentum and energy of removed nucleons will be described. The results presented in this section will be compared to previous work on similar quasi-free scattering reactions in chapter 7.

5.1 Angular Correlations and Event Identification

Given the geometry and angular coverage of the target-recoil detectors, the most natural coordinate system to use throughout the analysis has been a spherical one. In this system, quantities such as momentum and energy can be easily expressed as vectors whose direction is specified by the polar angle ϑ and the azimuthal angle φ. The angle of the scattered protons participating in a quasi-free scattering reaction can be determined both by the DSSSDs arranged around the target and by the Crystal Ball detector in which they deposit most or all of their energy. The best angular resolution is given by the DSSSDs while the larger angular coverage is given by the Crystal Ball. By combining the signals of both detectors, such that angular information is taken primarily from the DSSSDS and correlated with the Crystal Ball acting primarily for triggering purposes, a clear signature of potential quasi-free scattering events can be made and the individual tracks of the scattered protons emerging from the target can be constructed (see Fig. 5.1).
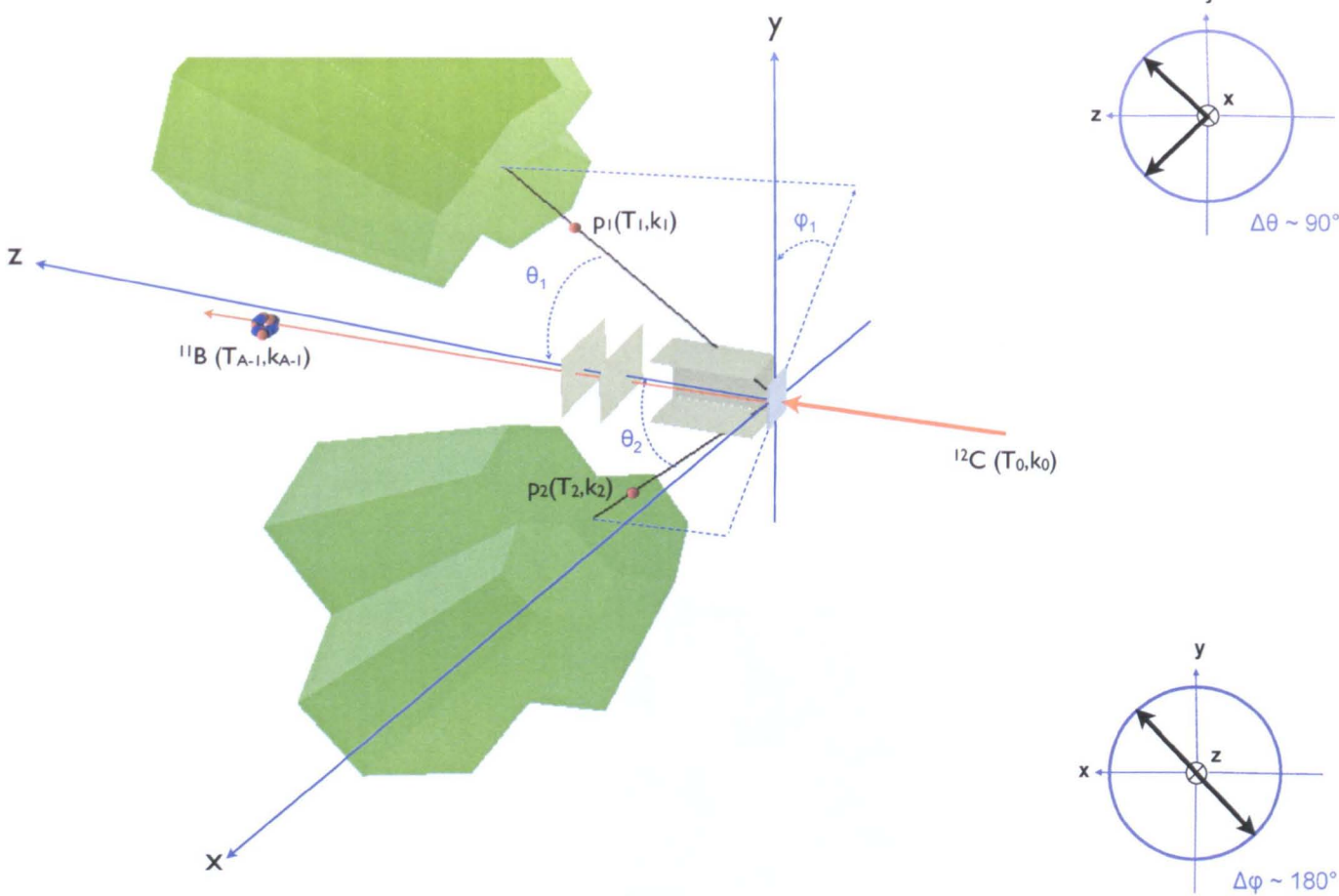
Figure 5.1: Schematic of a $^{12}C(p, 2p)^{11}B$ event taking place with a CH_2 target and entering the target-recoil detectors. T is the kinetic energy of a particle participating in the reaction, and k its momentum. Events from a $(p, 2p)$ process are expected to have clear kinematical correlations in ϑ and φ such that events can be selected with cuts applied to the protons emerging from the target with $\vartheta \sim 90°$ and $\varphi \sim 180°$.

Angular correlations have been observed in previous experiments [84, 85] with more basic versions of the current setup (e.g. Fig. 2.13) and are explained using a simple kinematical model discussed in chapter 6. These correlations are observed in the present experiment and are shown in Fig. 5.2.
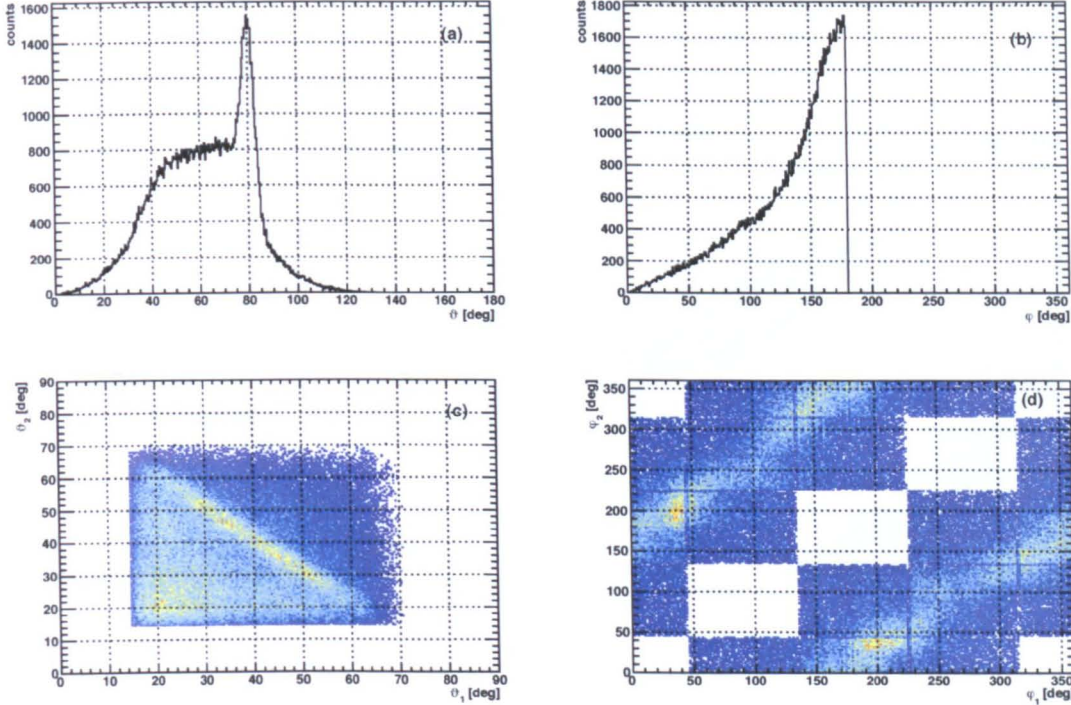
Figure 5.2: Angular correlations of scattered protons from $^{12}C(p, 2p)X$ events produced with a 2.31 mm CH_2 target and a beam energy of 400 MeV.A. All angles are measured by correlating angular information from the 'box' DSSSDs with signals in the Crystal Ball (a procedure that lowers the solid angle coverage but improves the angular resolution and identification of events). Fig. (a) shows the polar angle ($\sim \vartheta_1 + \vartheta_2$) of the proton pair emerging from the target with the contribution from the carbon present in the CH_2 target visible below the hydrogen peak at $\vartheta \sim 80°$. Fig. (b) shows the azimuthal angle of the proton pair ($\varphi_1 - \varphi_2$). Fig. (c) shows the polar angle of the first proton plotted against the second. Fig. (d) shows the azimuthal angle of the first proton plotted against the second. Correlations are clearly seen in both ϑ and φ confirming that quasi-free scattering is taking place. These kinematical correlations can be used to select events for the subsequent analysis.

Contributions from the carbon and the hydrogen in the CH_2 target can be clearly seen when the kinematical correlations are compared with the simulation mentioned above for the same reaction using a hydrogen target (Fig. 5.3). In both cases the proton peak in the polar angle plot (a), emerges at $\sim 80°$.

Using energy loss cuts in the box of DSSSDs around the target ensures that protons appear above the electronic noise, and a kinematical cut for the proton pair emerging
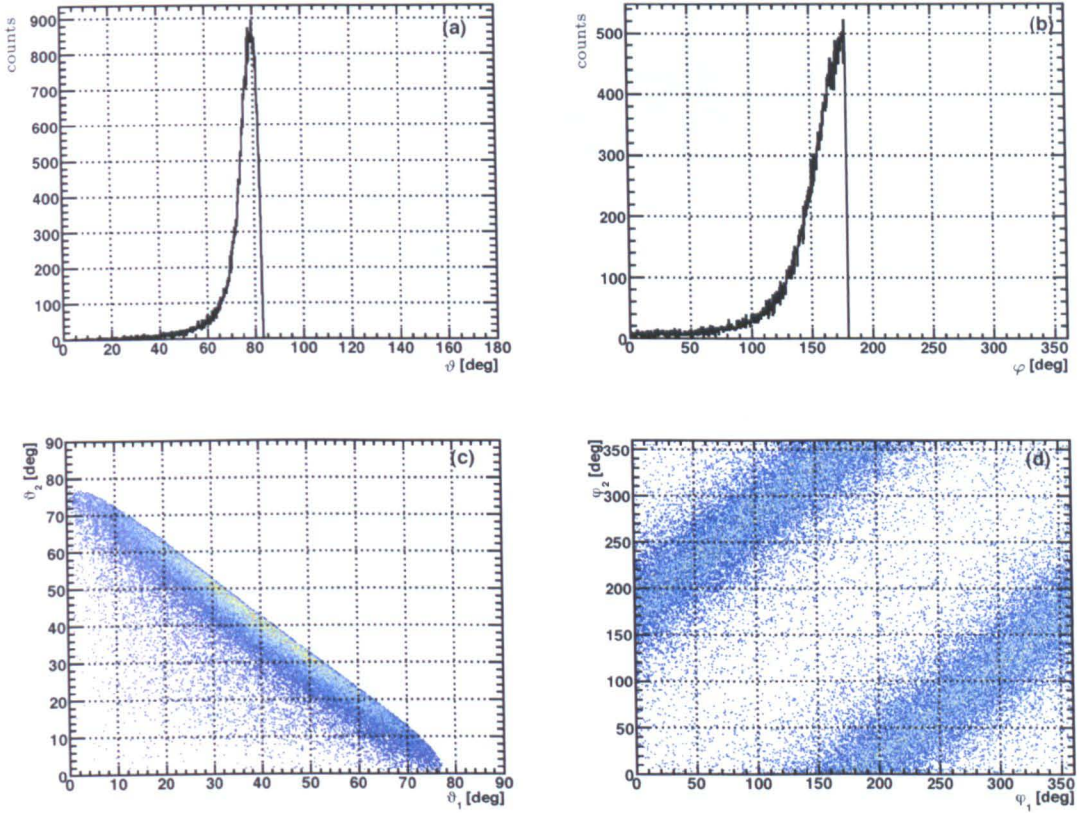
Figure 5.3: Simulated angular correlations for $^{12}C(p, 2p)X$ events produced with a H target and a beam energy of 400 MeV.A. Calculations with this kinematical simulation have been compared to a previous experiment here [84] and a description of the model upon which the simulation is based is given in chapter 6.

from the target at $\sim 80°$ allows a good selection of the $^{12}C(p, 2p)^{11}B$ events for further analysis. The decay channels of the fragment after the reaction can then be identified by the fragment A and Z values after they have passed through the magnetic field of ALADIN. This is shown in the particle identification plot in Fig. 5.4.

Isotopes produced in a $(p, 2p)$ process can decay in numerous ways. If a proton is removed from the outer p-shell in ^{12}C, the ^{11}B fragment can remain intact occupying either its ground state or an excited state that will decay with γ-ray emission. For proton removal from the more deeply bound s-shell in ^{12}C, fragments will be highly excited into the continuum of ^{11}B and can decay by emitting single or multiple nucleons and clusters, in addition to γ rays until the ground state is reached. Further characterisation of the states from which the proton has been removed will be discussed in the following sections.
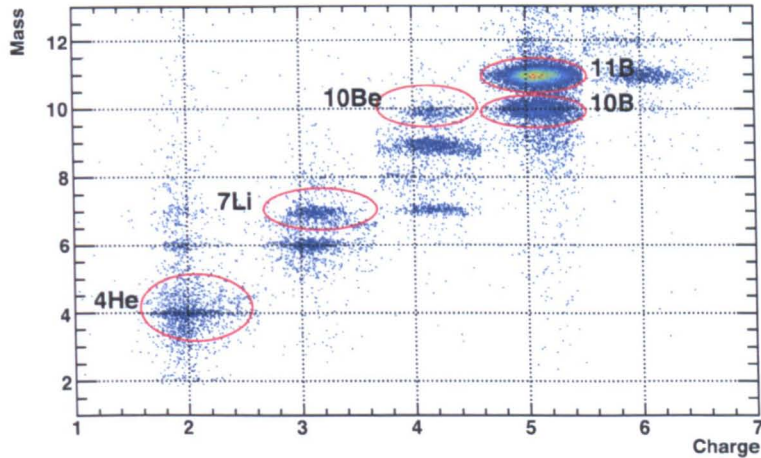
Figure 5.4: Particle identification measured for events produced by the $^{12}C(p, 2p)X$ reaction. These events are selected using energy loss and kinematical cuts on the protons emerging from the target as discussed above. Some of the more prominent decay channels are labelled.

5.2 Background Subtraction

Despite the kinematical selection of the protons and the A and Z values of fragments after the ALADIN magnet, background can still be present for some of the quantities being reconstructed. This can be separated into two different sources, both of which can be subtracted. Firstly, since the CH_2 target is composed of both carbon and hydrogen atoms, unwanted nuclear reactions can contribute to the final set of events because of reactions with the carbon that is present in the target. Secondly, reactions can occur outside of the target because of collisions with the setup and beam line materials as well as with the air between some of the detectors. In order to observe only quasi-free reactions between the incident ^{12}C ions and the hydrogen present in the target, both types of background should be estimated and subtracted. This is done by taking data during the experiment with carbon and empty targets which can be analysed with the same cuts applied to the CH_2 data. The data sets produced with the different targets are then normalised so that the different yields for each target can be estimated for the same number of incoming events. A second normalisation is carried out between the CH_2 and carbon target data sets because of the different thicknesses and densities of the two targets and the assumption is made that the background contribution from the setup will be independent of the target that is used. Details of these targets used for the experiment are given below in Table 5.1.

Target	Thickness	Density	Atomic Mass	Area Density
CH_2	2.31 mm	0.92 g/cm^3	14 u	9.1418×10^{21} /cm^2
Carbon	2.01 mm	1.84 g/cm^3	12 u	1.8561×10^{22} /cm^2

Table 5.1: A comparison of the targets used for the s296 experiment.

The density normalising factor for the carbon and CH_2 targets is given by the ratio of the respective area densities:

$$\rho_s = \frac{\rho_{CH_2}}{\rho_C} = 0.4925 \tag{5.1}$$

The background subtraction (after event normalisation) is then carried out in the following way:

$$X = N_{CH_2} - \rho_s N_C - \alpha N_E \tag{5.2}$$

where X is the final number of counts and N_{CH_2}, N_C and N_E are the total number of events of interest generated by the CH_2, carbon and empty targets respectively. Since some of the empty target contribution is subtracted in the carbon target contribution, the final empty target subtraction can be scaled such that it does not need to be subtracted twice. Assuming that the background from the setup is the same for normalised CH_2 and carbon target runs, since $\rho_s \sim 0.5$, it follows that only approximately half the background from the setup has been subtracted in the CH_2 - C subtraction and therefore that a further factor of: $\alpha = (1 - \rho_s) \sim 0.5$ multiplied by the empty target contribution is still left to be subtracted from the CH_2 events. In general, the more conditions that must be satisfied and the greater the number of detectors used to reconstruct a quantity, the lower the background from both sources becomes. An example of a reconstructed quantity after background subtraction is shown in Fig. 5.5.
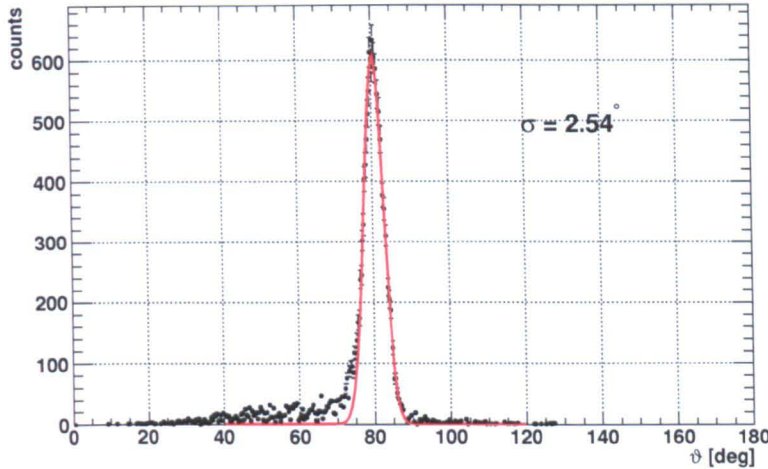
Figure 5.5: The polar angle (ϑ), of the scattered proton pair for events produced by the $^{12}C(p, 2p)X$ reaction after background subtraction. This figure can be compared with Fig. 5.2a in order to see the effect of the background subtraction procedure.

5.3 Energy-Momentum Four-Vectors

For each nuclear reaction, projectiles enter the cave and impinge upon the target at relativistic energies ($v/c \sim 0.7$). It is therefore useful to construct energy-momentum four-vectors for the fragments and γ-rays emerging from the target during a reaction of interest. This procedure is necessary for the reconstruction of certain quantities because they cannot be measured directly, i.e. because a Lorentz transformation is required to change from the laboratory frame where quantities are measured, to the centre of mass or rest frame to obtain their true values. Setting $c = 1$, the energy-momentum four-vector can be represented in the following way:

$$\mathbf{P} = \begin{pmatrix} E \\ P_x \\ P_y \\ P_z \end{pmatrix} \tag{5.3}$$

where E is the total energy of the system, and P_x, P_y and P_z are its momentum components in a standard right-handed coordinate system forming the total momentum vector: $\vec{p}$. The length of this four-vector is given by the following relation:

$$M = E^2 - \vec{p}^2 \tag{5.4}$$

72

where M is the rest mass of the system and is invariant under Lorentz transformation [108]. This property is named the invariant-mass of the system, and is used to obtain the excitation energy of unbound states occupied in ^{11}B populated after a ^{12}C$(p, 2p)X$ reaction.

Since the beam has its velocity directed along the z-axis, only quantities with components measured along this axis will need to undergo a Lorentz transformation. This transformation is carried out for the total energy, E, and longitudinal momentum component, P_z, in the following way:

$$\begin{pmatrix} E_{RF} \\ P_z^{RF} \end{pmatrix} = \begin{pmatrix} \gamma & -\beta\gamma \\ -\beta\gamma & \gamma \end{pmatrix} \begin{pmatrix} E^{LAB} \\ P_z^{LAB} \end{pmatrix} \tag{5.5}$$

where β, and γ are defined in the same way as in Eqn. 3.1, and the labels *RF* and *LAB* stand for rest frame and laboratory frame respectively. The transverse component of the momentum, P_{tr}, is formed from the components P_x and P_y which remain invariant under this Lorentz transformation.

5.4 Crystal Ball Doppler Correction

Fragments that emit γ rays after an interaction with the target will be moving with a velocity similar to the beam such that the measured energy of the γ rays in the Crystal Ball will be Doppler shifted to a larger value. In order to reconstruct the true energy of the γ-rays in the rest frame of the nucleus from which they were emitted, a Doppler correction is performed on an event-by-event basis. This correction for the energy is obtained using Eqn. 5.5 and shown below in Eqn. 5.6:

$$E_{RF} = \gamma E_{LAB} \left[1 - \beta \cdot cos(\vartheta_{LAB}) \right] \tag{5.6}$$

where E_{RF} is the γ-ray energy in the rest frame, E_{LAB} and ϑ_{LAB} are the energy and angle of the γ ray measured in the laboratory frame. The angle at which the γ ray is detected contributes significantly to the energy resolution of the measurement since it is only known with a precision defined by the opening angle of each NaI crystal ($\sim$78 msr). This effect is known as Doppler broadening and cannot be corrected for during the analysis.

5.5 Integrated Cross Sections

One of the key observables for any nuclear reaction is its cross section. A measurement of this quantity is a measurement of the probability that the reaction will occur, which

can in turn be linked to valuable nuclear structure information about the occupancy of a nuclear shell. Using the LAND/R^{3}B setup, cross section values for one and two nucleon removal have been determined for carbon and hydrogen targets using the following expression:

$$\sigma = \frac{N_f}{N_i}\frac{1}{N_t} \qquad (5.7)$$

where N_f is the number of fragments detected for a given channel, N_i is the number of ^{12}C ions incident on the target, and N_t is the area density of the target given in Table 5.1. Cross sections are determined for the C and H targets by carrying out the background subtraction as outlined in Eqn. 5.2. Measurements with a C target can be compared to similar experiments using normal kinematics at different energies as well as to a calculated theoretical value for the energy of this experiment (see section 7.4). This allows the method that has been used to extract the cross sections to be relied upon for measurements with the H target where there are very few experimental data available and a lack of theoretical work for comparison. In order to perform the cross section measurements, unambiguous events have the charge (or energy loss) of their fragments plotted in the first silicon detector after the target, against the charge or energy loss of the same fragments in the fragment TOF wall after the ALADIN magnet. This allows unwanted nuclear reactions that occur outside of the target to be easily identified and excluded. Additionally, efficiencies associated with the triggers and detectors used to select the events will have the same effect on all distributions making the extraction of the cross section more straightforward. Proton and proton-neutron removal events can be selected with an elliptical cut and counted along with the number of ^{12}C ions incident on the target. This separation is illustrated in Fig. 5.6.

After determining the number of events for a specific Z value, the mass of these fragments must be selected so that the cross section for a specific reaction channel can be extracted (see Fig. 5.7). Combining the number of events of a given mass and charge (N_f) with the number of incident ions (N_i) together with the target area density (N_t), as shown in Eqn. 5.7, gives a first measurement of the cross section. In order to make the value as accurate as possible, statistical corrections for legitimate events omitted by the cuts can be made by fitting and integrating the distribution of events in each of the detectors where the cuts are made. This effectively allows the efficiency of each of the cuts to be determined and any necessary corrections to be applied. For distributions that could not be fitted, functions that model the response of the detector to the specific charge or mass value were used, as shown in Fig. 5.8. Acceptance corrections for both the x and y dimensions are shown in Fig. 5.9 and Fig. 5.10.
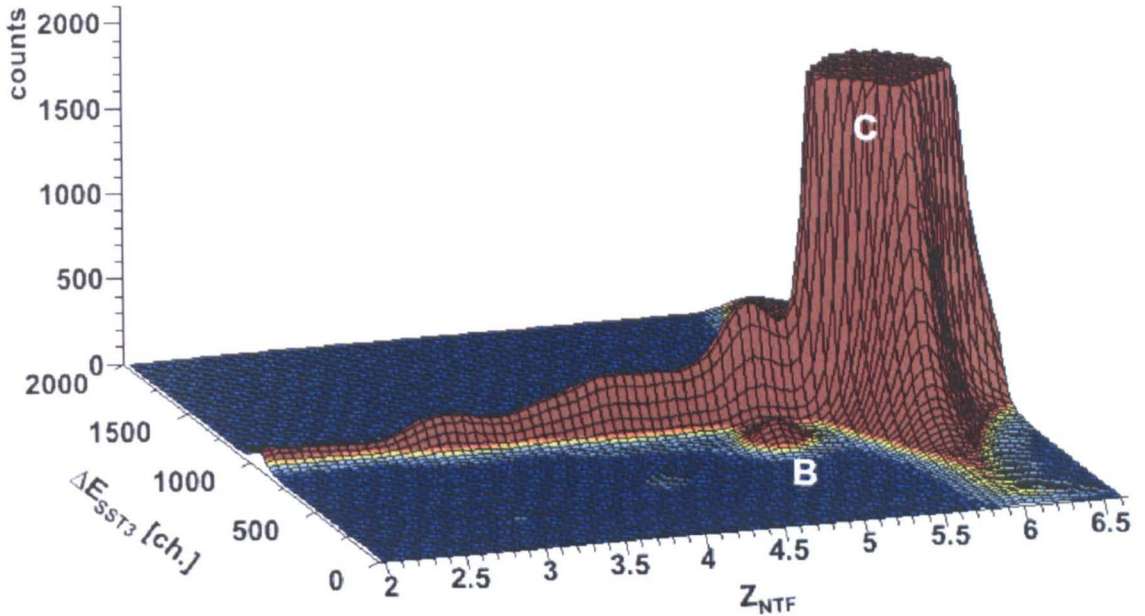
Figure 5.6: Distribution of fragments by their Z value before and after the ALADIN magnet for CH_2 target data. Boron and carbon fragments are denoted by the letters B and C respectively. Fragments created in reactions with the target can be recognised by the fact that their Z value remains the same before and after the magnet. Only events with a multiplicity of one have been selected in coincidence with the fragment trigger. Counts per bin are shown up to a maximum of 2000.

Cross section values after the corrections mentioned above are presented for proton removal, and for neutron-proton removal in Table 5.2.

Target	σ_{-p} [mb]	σ_{-np} [mb]
CH_2	82.7 ± 7.7	48.1 ± 5.3
C	45.9 ± 4.4	30.7 ± 2.3
H	18.4 ± 2.7	8.7 ± 1.7

Table 5.2: Total reaction cross sections measured for proton and neutron-proton removal from ^{12}C to bound states in ^{11}B and ^{10}B with their statistical errors.

In order to extract the cross sections to unbound states, the total cross section for all proton removal reactions given by the target-recoil detectors could be subtracted from the bound state cross sections presented here. This has not yet been possible due to an error in the construction of the Crystal Ball sum trigger.
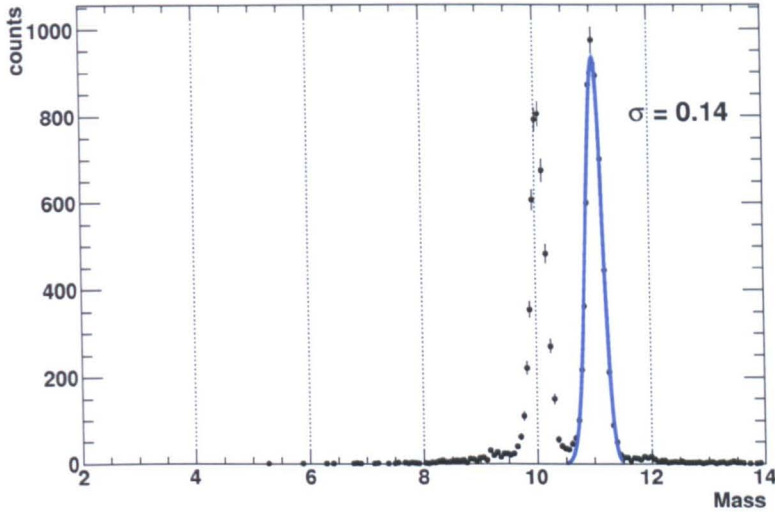
Figure 5.7: The mass distribution for boron fragments selected as shown in Fig. 5.6 and produced with a CH_2 target. The fit for the $A = 11$ events allows the efficiency of the mass cut to be calculated, which is high because the masses are well resolved. The $A = 10$ peak corresponds to proton-neutron removal from ^{12}C.
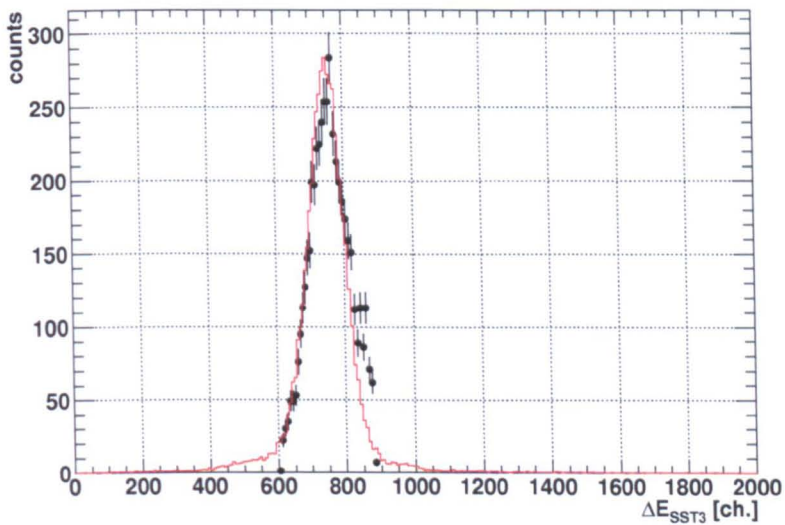
Figure 5.8: The charge correction for $Z = 5$ events in the k-side of SST3 produced with a C target. The data are shown in black and the corrected distribution in red. The response function for the correction is generated by selecting $Z = 5$ events in detectors before and after the k-side of SST3 so that its response can be determined as unambiguously as possible.

76
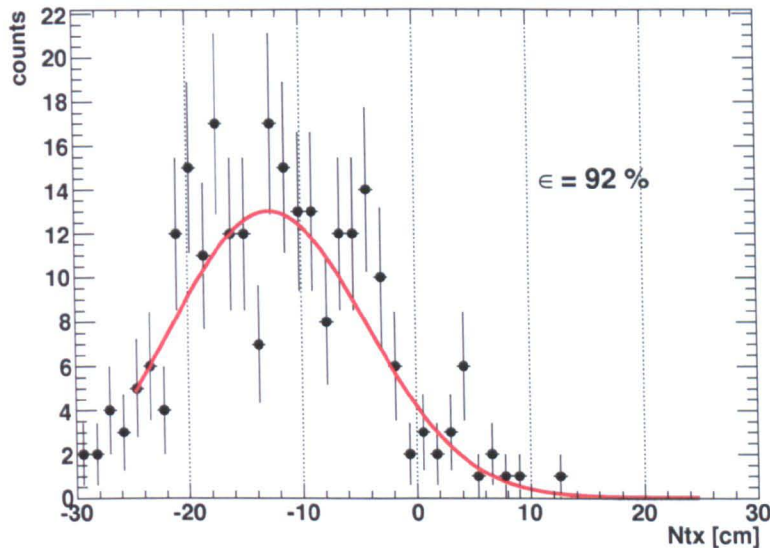
Figure 5.9: The acceptance of the NTF detector in the x-direction for ^{11}B events produced with an empty target. The integral of the fit (shown in red) allows a measurement of the acceptance loss of the detector in the x-direction.
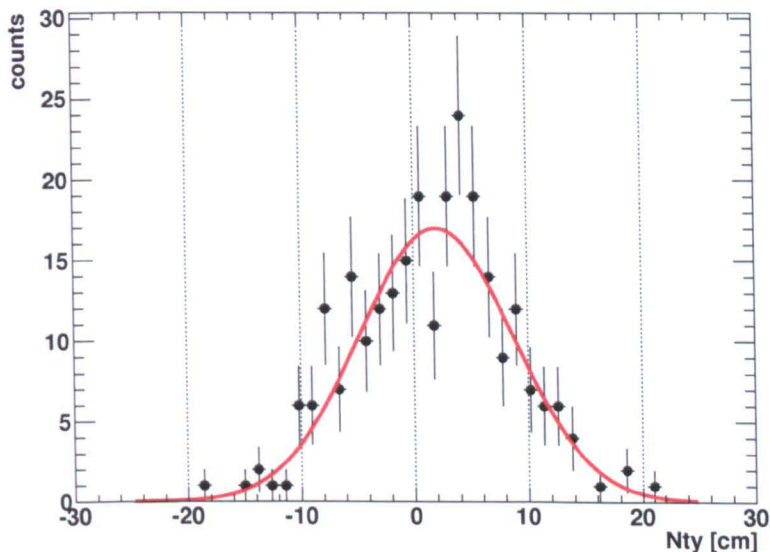
Figure 5.10: The acceptance of the NTF detector in the y-direction for ^{11}B events produced with an empty target. The integral of the fit (shown in red) allows a measurement of the acceptance loss of the detector in the y-direction, which is zero compared with 8% in x (see Fig. 5.9).

5.6 Momentum Distributions

The projection of the momentum distributions of fragments or nucleons onto an axis can be analysed to determine which orbital the removed nucleons were taken from as discussed in chapter 2. Typically, the longitudinal momentum (P_z) component is measured since it receives less deflection from the Coulomb field of the target nuclei compared to the transverse momentum components. However, since the beam in this analysis carries a large momentum (~ 11.4 GeV/c) and the target has a low Z, the transverse momentum components P_x and P_y can be used. The total momentum of a particle in the laboratory frame is given by:

$$P = m_0 \beta \gamma \tag{5.8}$$

where m_0 is the rest mass of the particle. The components of the momentum in spherical coordinates are:

$$
\begin{aligned}
P_x &= P sin(\vartheta) cos(\varphi) \\
P_y &= P sin(\vartheta) sin(\varphi) \\
P_z &= P cos(\vartheta)
\end{aligned}
\tag{5.9}
$$

By summing quadratically both the P_x and P_y components of the transverse momentum, the total transverse momentum $P_{tr} = \sqrt{P_x^2 + P_y^2}$ is calculated. This is shown for ^{11}B fragments produced with the reconstructed H target in Fig. 5.11. One of the advantages of performing quasi-free scattering using inverse kinematics is the ability to measure both the residual fragment and the knocked out nucleon together. In the case of momentum this would be particularly useful as it would allow a comparison to be drawn that would give some idea of the contribution to the momentum from final state interactions and the comparison of momentum widths for both bound and unbound states in ^{11}B. Due to the difficulties faced in calibrating the Crystal Ball's high energy readout (outlined in both chapter 4 and chapter 6), it has not been possible to obtain the proton momentum distributions for comparison with the fragment distributions presented here. For comparison with the H target results shown in Fig. 5.11, momentum distributions for ^{11}B fragments obtained by proton removal with the C target are shown in Fig. 5.12.
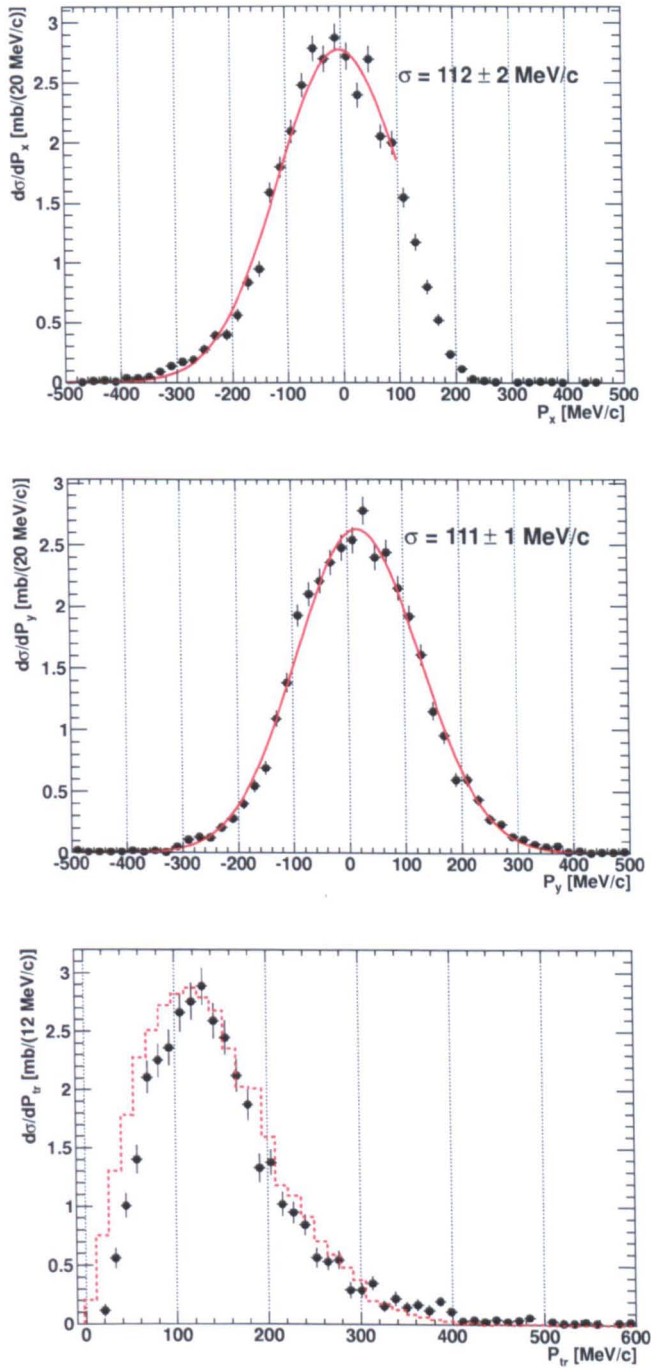
Figure 5.11: Transverse momentum distributions for ^{11}B fragments produced with the reconstructed H target. The first figure shows the P_x component of the transverse momentum and its fit limited by the acceptance of the NTF detector. The second figure shows the P_y component of the transverse momentum with its fit and no acceptance loss. The third figure shows the total transverse momentum P_{tr} reconstructed from the first half of the P_x distribution and its associated P_y components. The distribution represented by the red dashed line is calculated using the widths of the P_x and P_y distributions.
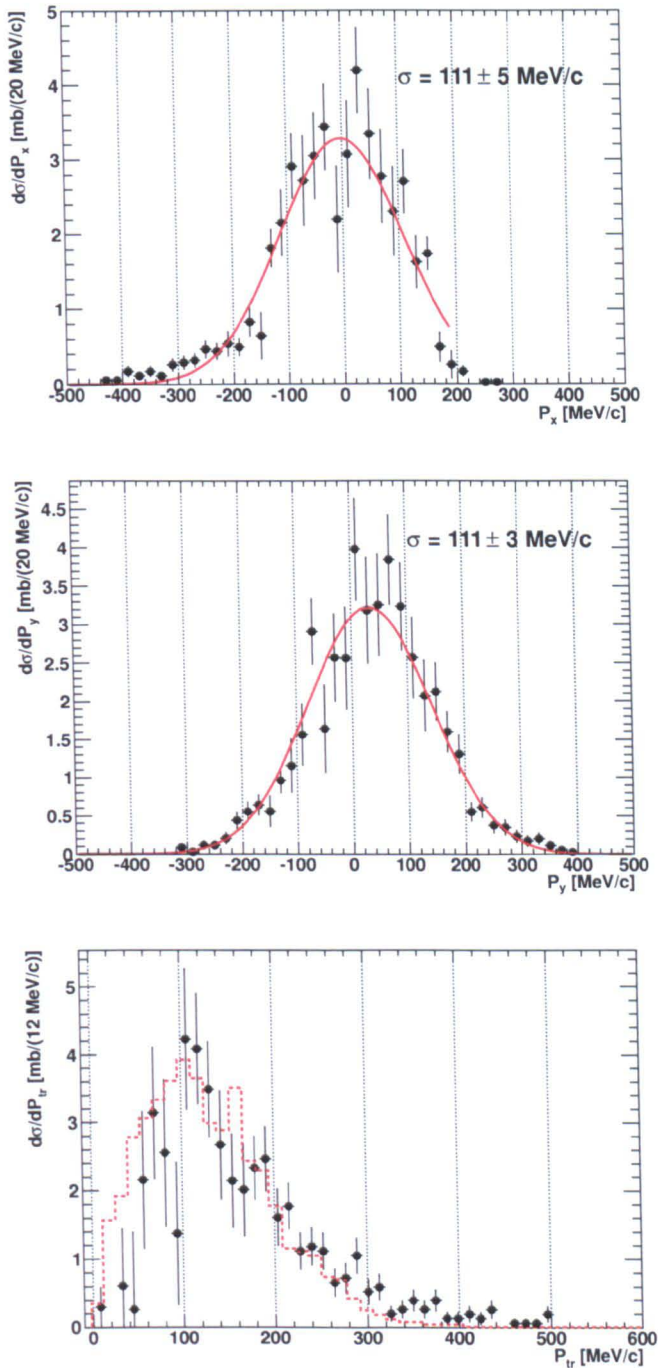
Figure 5.12: Transverse momentum distributions for ^{11}B fragments produced with a C target. These figures show the same quantities as Fig. 5.11.

In order to estimate the contribution to the momentum distributions from the straggling of the beam in the detectors and target, the momentum of unreacted ^{12}C beam has also been measured. This is shown in Fig. 5.13 which demonstrates that the presence of the target increases the width of the momentum distribution by $\sim$10 -

15%. The width of the momentum distribution for unreacted ^{12}C beam with an empty target comes from both the angular resolution of the detectors used to analyse the momentum, as well as the straggling of the beam and fragments in the detectors themselves. In comparing this momentum resolution with the momentum width for the ^{12}C$(p, 2p)^{11}$B and ^{12}C$(^{12}$C,^{11}B$)X$ reaction channels it is clear that the momentum width for nucleon removal (approximately 100 MeV/c [109]), is much wider than its resolution. This allows a feasible momentum measurement to be made despite the fact that the incoming angle has not been measured on an event-event by event basis (see section 3.2.2).
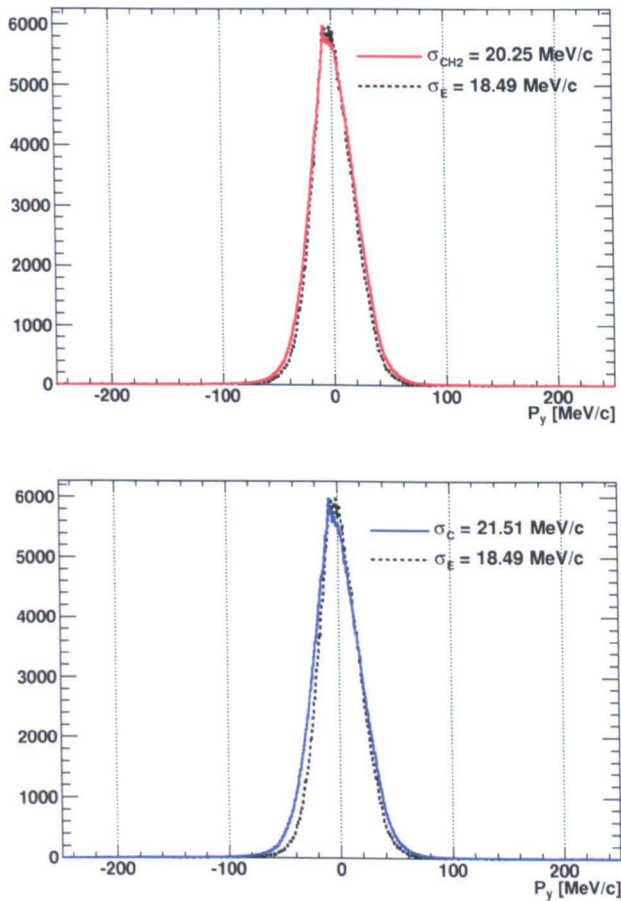
Figure 5.13: A comparison of the P_y distribution of transverse momentum for unreacted ^{12}C beam with, and without, a target. The presence of the CH$_2$ target for example, introduces an additional straggling of $\sigma = \sqrt{20.25^2 - 18.49^2} = 8.26$ MeV/c. This result is reproduced by the computer simulation ATIMA [110] which calculates various physical quantities in order to characterise the passage of charged particles through matter.

5.7 The Excitation Energy

In order to determine which states in ^{11}B have been populated during the ^{12}C$(p, 2p)X$ reaction, the excitation energy of ^{11}B is reconstructed, making use of all the detectors surrounding the target and after the ALADIN magnet. Transitions to the ground state of ^{11}B are assigned when no decays are observed in the target-recoil or fragment detectors after ALADIN. Bound excited states are reconstructed using the Crystal Ball detector, while unbound excited states are reconstructed using multiple detectors and the invariant-mass method. Combining all these results allows the excitation energy spectrum for ^{11}B to be reconstructed.

5.7.1 Reconstruction of Bound States

Bound states in ^{11}B are reconstructed using in-beam γ-ray spectroscopy with the Crystal Ball detector and the add-back algorithms to be described in chapter 6. Transitions from excited states are clearly observed and shown in Fig. 5.14.
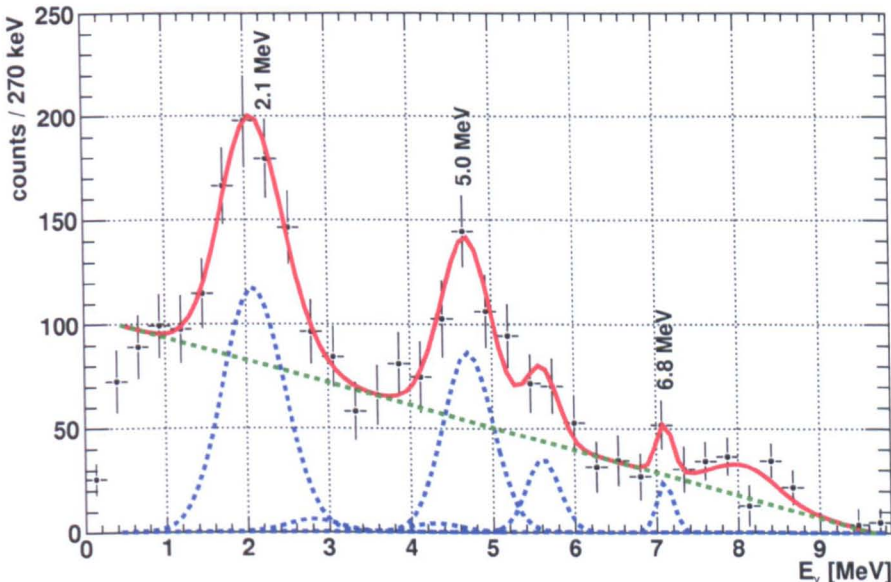
Figure 5.14: The γ-ray energy spectrum measured with the Crystal Ball for ^{12}C$(p, 2p)^{11}$B* reconstructed H target events. Three decays that occur directly to the ground state have been labelled with their known energies (see Fig. 5.15) and fitted with Gaussian distributions. The first labelled transition has a mean of 2.1 MeV and σ = 0.4 MeV, the second a mean of 4.7 MeV and σ = 0.3 MeV, and the third a mean of 7.1 MeV and σ = 0.1 MeV. Transitions below 7.1 MeV that are not labelled are indirect decays or 'cascades' to the ground state. Above 7.1 MeV states are not fully resolved and have not been labelled. A linear function in green is applied to describe the residual background. The red distribution is composed of the green and the blue distributions and fitted to the data points and their statistical error bars shown in black.

These transitions have been identified with the help of previous work to be discussed in chapter 7, and are indicated on the partial level scheme for ^{11}B shown in Fig. 5.15. In order to improve the fitting procedure, the mean value of each Gaussian was permitted to differ from the known value by a maximum of 400 keV. States below 6 MeV appear shifted to lower energies, an effect that has been seen in previous experiments with the Crystal Ball [111]. This is due to the response of the detector to high energy γ rays with a significant Doppler shift. For the states above 6 MeV the shift in energy appears in the opposite direction. This may be due to the contamination of the γ-ray energies with the proton energies from the same event (see section 6.2.2). In addition to the tolerance applied for the mean values of each Gaussian, the σ values of each fit were constrained by the width of the first transition *i.e.* by requesting that they be less than 400 keV.
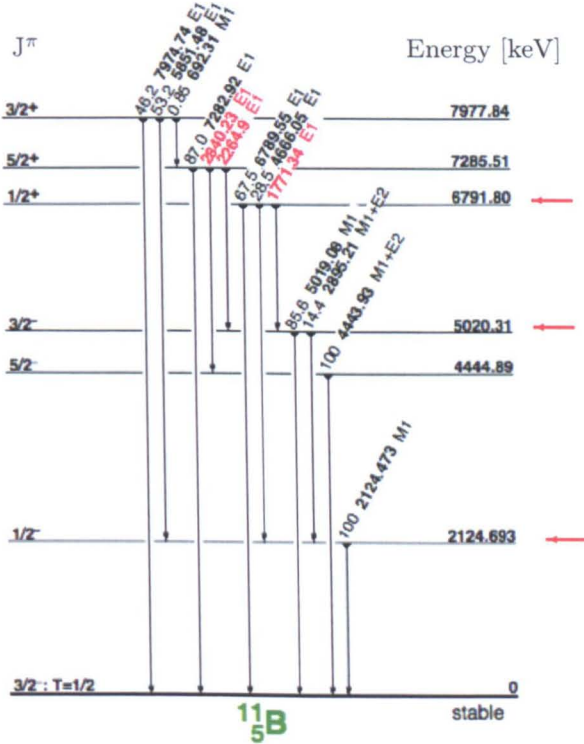
Figure 5.15: Partial γ-ray level scheme for ^{11}B showing excited states below the α particle emission threshold. The states from which the labelled transitions in Fig. 5.14 occur are indicated by the red arrows. Additional γ-rays are observed by decays occurring between these states and others above it. Figure developed from the data collated in this reference [112].

5.7.2 Reconstruction of Unbound States

Unbound states in ^{11}B decay by emitting nucleons or clusters of nucleons when the fragment is excited above certain energy thresholds (see Fig. 5.16). For these events,

access to the energy of the unbound system depends upon construction of the energy-momentum four-vectors of all the particles involved in the decay, and thus the energy must be calculated on an event-by-event basis, rather than being measured directly (as is possible when observing a decay from bound excited states).
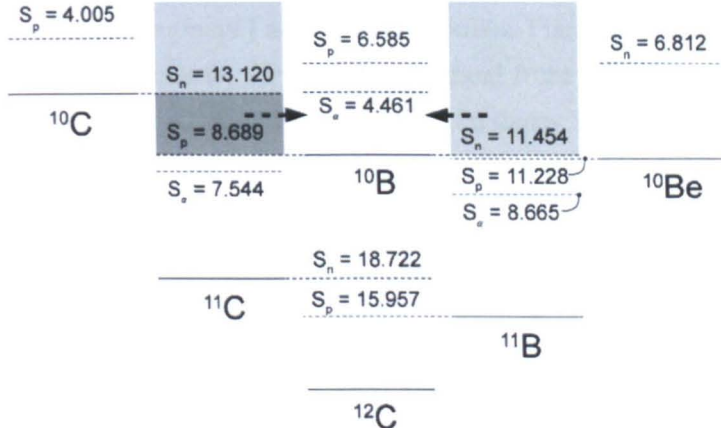
Figure 5.16: Level scheme showing n, p and α particle separation energies for fragments produced by one and two nucleon removal from ^{12}C. ^{11}B fragments produced in a $(p, 2p)$ reaction can be excited into the continuum i.e. above the particle emission thresholds such that their decay must be reconstructed with the invariant-mass method. Below the α particle emission threshold in ^{11}B, particles decay via γ-ray emission which can be reconstructed with the Crystal Ball detector. Figure taken from [62].

If all the particles in the decay can be identified in this way, the excitation energy can be reconstructed using the invariant-mass method described in section 5.3 and below in Eqn. 5.10:

$$M = \sqrt{\sum_i m_i^2 + \sum_{i \neq j} \gamma_i \gamma_j m_i m_j (1 - \beta_i \beta_j cos\vartheta_{ij})} + E_\gamma \tag{5.10}$$

where i and j denote the different particles involved in the decay, β and γ are defined in Eqn. 5.6, ϑ is the angle between the fragments and E_γ the energy of any γ-rays deposited in the Crystal Ball. This quantity is derived from the length of the energy-momentum four-vectors for each of the particles in the decay and can be used to obtain the excitation energy of the decaying system since it is the same in all frames of reference. The rest mass of the system before decay can be subtracted from the total energy of the decaying system measured in the laboratory. Conservation of energy gives the difference between these quantities as the remaining excitation energy of the unbound system (Eqn. 5.11):

$$E^* = \sqrt{\sum_i m_i^2 + \sum_{i \neq j} \gamma_i \gamma_j m_i m_j (1 - \beta_i \beta_j cos\vartheta_{ij})} + E_\gamma - m_{proj} \tag{5.11}$$

where m_{proj} is the rest mass of the ^{11}B fragment. Since such distributions require the summation of quantities obtained from several different detectors, this will be reflected in the resolution of the measurement. An example of the opening angle of the ^{10}B+n system is shown in Fig. 5.17 and the associated TOF for the neutrons and ^{10}B fragments are taken from the NTF (fragment) and LAND (neutron) time of flight walls. For decays involving only charged fragments, the angle is obtained from the DSSSDs that are placed directly in the beam. Separation and selection of the decay fragments in these detectors can be made with the aid of plot such as Fig. 4.9. The individual decay channels that make up the final excitation energy spectrum are shown in Fig. 5.18. Corrections for the acceptance of the fragments have been applied as discussed for the cross section measurements presented in section 5.5 and shown in Fig. 5.9 and Fig. 5.10. In order to estimate the efficiency and acceptance for neutron detection, a response function for the LAND detector was calculated as a function of the incident neutron kinetic energy [113]. The response function was calculated using a simulation known as the LAND event generator (LEG) that has been successfully used in previous experiments [114]. A nominal value for the efficiency of the proton branch of the setup was taken from a previous similar experiment [115] because of the low statistics encountered for proton evaporation channels during this analysis. The response of the Crystal Ball detector is estimated using a GEANT4 simulation discussed in chapter 6.
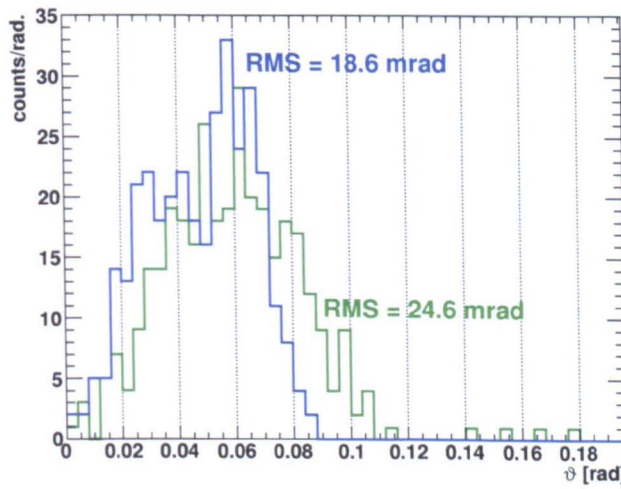
Figure 5.17: The opening angle of the unbound ^{10}B+n system for CH_2 target data. The blue data represent the angle of the neutrons only, and the green data the angle of the ^{10}B+n. The fragment β and angle come from the fragment time of flight wall (NTF) and the DSSSDs respectively, while the neutron β and angle are taken from the LAND detector.

5.7.3 The Excitation Energy spectrum

Combining the bound and unbound excited states for ^{11}B, the reconstructed excitation energy spectrum of ^{11}B is shown in Fig. 5.19. Contributions from bound and unbound decay channels are not normalised since it has not yet been possible to measure an integrated cross section for the decays from the s-state. A successful measurement of this quantity could be combined with the cross section presented in section 5.5 to give a total reaction cross section to which the distribution presented in Fig. 5.19 could be scaled. Instead, (as was the case with early $(p, 2p)$ work in normal kinematics, see Fig. 7.6) the spectrum is presented in order to show how both bound and unbound states have been probed by the ^{12}C$(p, 2p)X$ reaction, and how their decays contribute to the final energy spectrum. It is also possible to compare this spectrum qualitatively with those obtained using electrons and protons as probes on C targets that are discussed in chapter 7. Differences in resolution can be clearly seen especially when compared to the $(e, e'p)$ data. However, Fig. 5.19 displays the main structural features of ^{11}B. This includes the ground and excited states that are populated via proton removal from the p-shell of ^{12}C, as well as the unbound excited states populated with proton removal from the s-shell in which there are indications of some sub-structure.

The excitation energy of ^{11}B can also be obtained by measuring the energy of the protons that emerge from the target after a quasi-free scattering reaction. However, an adequate high energy calibration of the Crystal Ball detector has not been possible during this analysis. This issue is discussed further in the chapters 4 and 6 of this thesis.
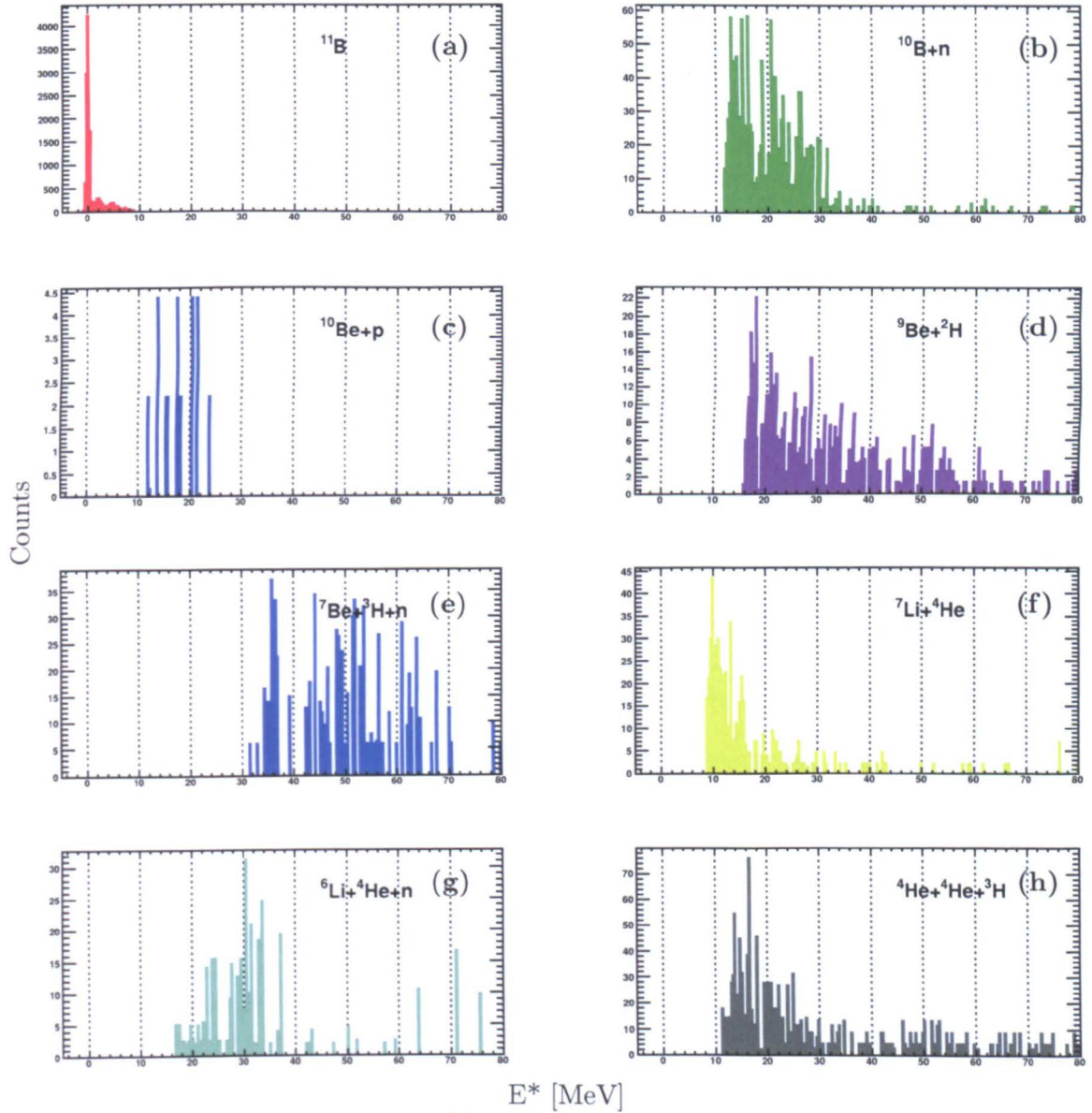
Figure 5.18: Fragmentation of the ^{11}B excitation energy for the reconstructed H target. Removal of a proton from the p-shell of ^{12}C produces a ^{11}B fragment in its ground state or bound excited states (Fig.(a)). Removal of a proton from the s-shell of ^{12}C produces a ^{11}B fragment that is excited above the particle emission threshold resulting in decay via the various unbound channels (presented in Fig.(b) - Fig.(h)). These individual excitation energy spectra can be combined to give the total excitation energy spectrum for ^{11}B shown in Fig. 5.19.
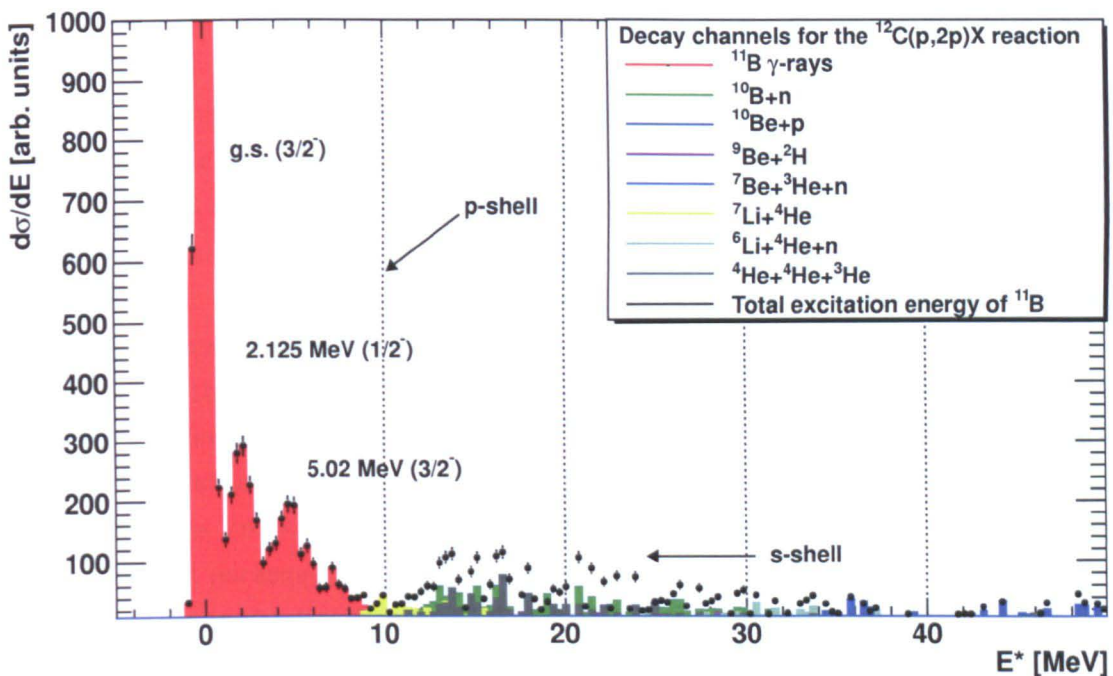
Figure 5.19: The excitation energy spectrum of ^{11}B using ^{12}C$(p, 2p)X$ events produced with the reconstructed H target. The spectrum is constructed from the individual energy spectrums shown in Fig. 5.18, namely, the bound states measured by the Crystal Ball detector corresponding to proton removal from the p-shell of ^{12}C, and the unbound states measured with the proton, fragment and neutron detectors after the target, corresponding to proton removal from the s-shell. Counts per bin are shown up to a maximum of 1000.

Chapter 6

GEANT4 Simulations

Alongside the development of the *land02* framework for the analysis of experimental data (see chapter 4), a simulation package that can adequately describe the response of the LAND/R^{3}B setup to high energy beams and their reaction products has become necessary. A first initiative at such a simulation known as R3Bsim [116] focused upon the Crystal Ball detector and another similar detector composed of CsI crystals and plastic scintillators placed around the target in previous experiments [85]. However this did not contain the geometry of all necessary detectors and the event generators to model quasi-free scattering reactions. More recently, GSI has commissioned a new software platform from which the various experiments at the FAIR facility can be simulated. This platform is known as FAIRROOT [117] and is based upon the GEANT [118] and ROOT [98] packages developed at the CERN laboratory in Geneva. FAIRROOT contains within it the full geometry of the proposed R^{3}B setup as well as all of the current detectors in the LAND/R^{3}B setup in the form of a sub-program known as R3BRoot [119]. During the analysis of this experiment, developments of this simulation have taken place that have allowed the response of the target-recoil detectors to high energy protons and γ rays to be modelled and better understood. This has allowed the optimisation of the add-back procedure that is used to separate proton and γ-ray events in the detectors and obtain their energy and angle. The efficiency of the Crystal Ball to detect γ-ray events measured in coincidence with two high energy protons has also been estimated.

6.1 Event Generator Based on the Goldhaber Model

In order to determine the response of the target-recoil detectors to a $(p, 2p)$ process, a realistic event generator is required as input to the R3BRoot simulation. It is particularly important to determine the response of the Crystal Ball detector to events that contain not only two protons but γ rays as well. This gives an indication of how well the energies

from the different particles can be separated (discussed further in the add-back section below) and also allows a response function for the γ-ray energy spectra to be created and fitted to the experimental data. From this description of the data, factors such as total efficiency and energy resolution can be better understood. The event generator that has been used relies upon a kinematical code developed by Leonid Chulkov at GSI, and is based upon the Goldhaber model [120, 121]. In this model, the width of the intrinsic momentum distribution of a knocked-out cluster or nucleon is related to its binding energy in the following way:

$$\sigma_g^2 = \sigma_0^2 \frac{A_1 A_2}{A} \tag{6.1}$$

where σ_g is the width of the momentum distribution (a value of 165.7 MeV/c is calculated by the simulation for ^{12}C), σ_0 a constant relating to the average binding energy of a nucleon, A is the mass of the nucleus before nucleon removal which become the two fragments of mass A_1 and A_2. The proton-proton scattering kinematics are calculated using the beam energy and intrinsic momentum of the protons in the projectile together with the differential cross section for elastic scattering of these protons from a hydrogen target at rest. Events are generated for protons over the forward hemisphere (2π) of the Crystal Ball and merged with Doppler boosted γ-ray events emitted over the full 4π solid angle. Excited states in ^{11}B are populated and decay to the ground state directly or via a γ-ray cascade. The Goldhaber model is attractive because of its simplicity and ability to reproduce the kinematical correlations that are expected in fragmentation reactions [120] (see Fig. 5.2 and Fig. 5.3). The addition of Doppler boosted transitions in the γ-ray cascade (see Fig. 5.15) allows a more realistic picture of the detector response to the ^{12}C$(p, 2p)^{11}$B reaction (see Fig. 6.1).

6.2 Simulating the Response of the Crystal Ball Detector

The goal of the response simulation is to take events from the event generator and pass them through the R3BRoot simulation containing the geometry and materials of the target-recoil detectors. In this way, the simulation acts as an experimental filter for the generated $(p, 2p)$ events, after which variables similar to those used in the experimental data can be constructed. These variables can be passed through the same reconstruction algorithms that are used for the analysis of the experimental data allowing a quantitative comparison between the two.
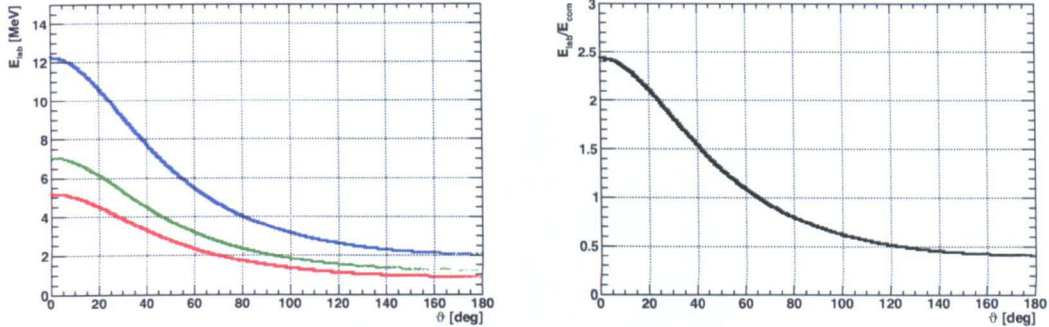
Figure 6.1: The energy of γ-rays emitted from a moving projectile with $\beta = 0.712$ and detected by the Crystal Ball as a function of detection angle. The first figure depicts how the energy varies for each of the transitions in the cascade (see Fig. 5.15) as a function of detection angle (red is the first excited state at 2.12 MeV, blue the third excited state at 5.02 MeV, and green the transition between them at 2.9 MeV). The second figure shows the ratio between the centre of mass energy and the laboratory energy of the γ rays as a function of detection angle. The β value used corresponds to the energy of the beam corrected for energy loss up to half the target thickness.

6.2.1 Crystal Ball Response to High-Energy Protons

Earlier measurements using individual crystals and proton beams [23] led to the conclusion that above $\sim$270 MeV protons would have sufficient energy to penetrate through the entire length of a crystal preventing their full energy from being measured (see also chapter 4). In addition to confirming this fact, the R3BRoot simulation showed that a full measurement of the proton or γ-ray energy is not always possible even if it is fully absorbed, due to the large number of secondary reactions that can be generated (depicted in Fig. 6.2). Many of these secondary particles do not pass the energy threshold for detection or leave the Crystal Ball without being fully stopped or detected. Limitations such as this are important considerations for the upgraded versions of the target-recoil detectors that will be used in the R^3B setup at FAIR.

The fraction of proton events that escape the Crystal Ball without depositing their full energy is shown for an isotropic distribution of 200 MeV protons in Fig. 6.3.

6.2.2 Optimisation of the Add-Back Algorithm

Events in the Crystal Ball from charged particles or γ rays will usually cause a group of crystals or 'cluster' to fire. The identification of the clusters that belong to recoiling protons is the first step in identifying the $(p, 2p)$ reaction channel and is depicted for experimental and simulated data in Fig. 6.4. The energy deposited in a cluster must be summed and added back to the first crystal that received the event (see Fig. 6.5) so that the correct angle can be obtained for the interaction and its full energy recovered.
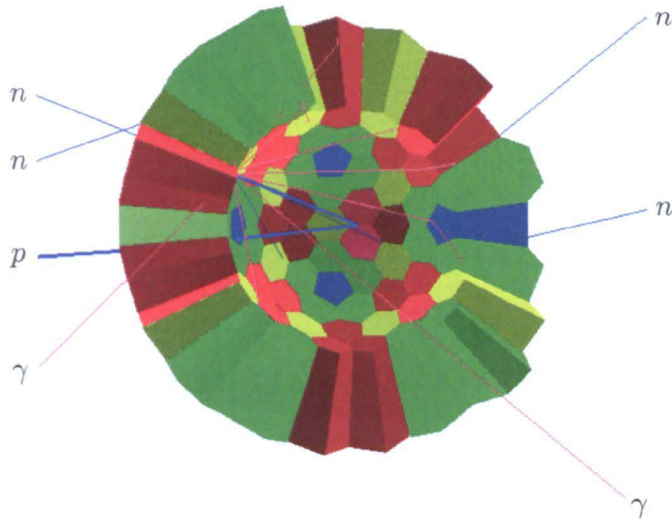
Figure 6.2: Cross section through the Crystal Ball showing a typical $(p, 2p)$ event (thicker lines) in which one proton is absorbed by the Crystal Ball and the other 'punches' through. Secondary interactions that produce neutrons and γ-rays within a crystal can prevent a full energy measurement of the absorbed proton.

For charged particles the angle from the Crystal Ball can be correlated with the angle obtained from the DSSSDs and for γ rays the angle is used to perform the Doppler correction.

The procedure used by the add-back routines for determining and separating the proton and γ-ray clusters is to create a list of all crystals that have received energy during an event that are then sorted by their energy. The central crystal for a cluster is taken as the highest energy crystal and its neighbours are found by taking the crystal with the next highest energy and checking to see if it is a neighbouring crystal. Additional thresholds and conditions are applied to help disentangle crystals that contain energy belonging to a proton or γ-ray event. Once a cluster has been built from the crystals in the list, the crystals it contains can be removed and the procedure repeated until all crystals containing sufficient energy have been accounted for. Challenges with this procedure arise when the multiple hits that can be generated from a single event in the target prove difficult to distinguish from each other. This occurs when different particles belonging to the same event have low angular separation such that a single crystal can receive energy from both a proton and a γ ray, for example. This creates an ambiguous situation for the add-back procedure, and events where the energies of particles cannot be separated should be discarded to avoid large background occurring in the energy spectra for the Crystal Ball. For the crystals in the forward hemisphere of the Crystal Ball which contain both a high energy and a γ-ray readout, an additional
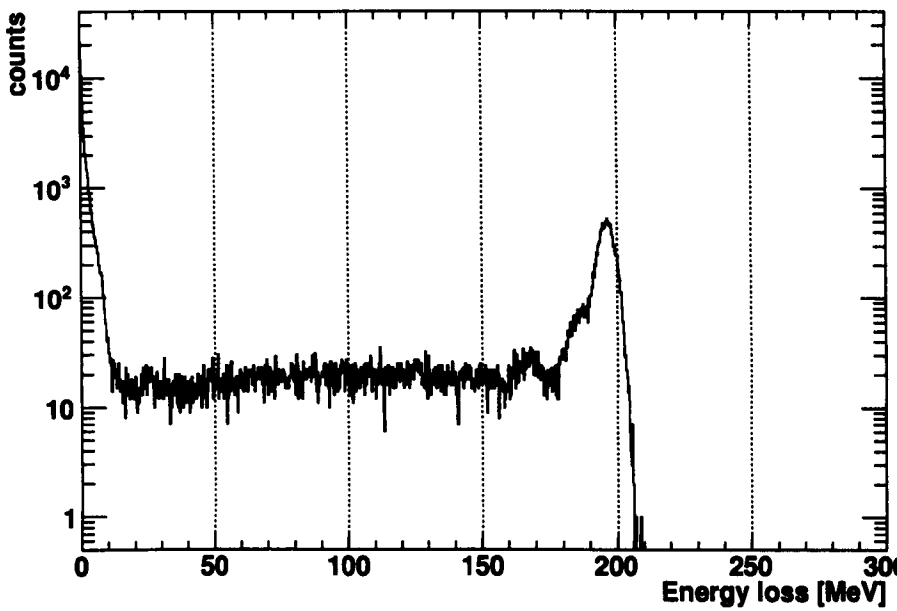
Figure 6.3: The energy loss of single 200 MeV proton events in the Crystal Ball, assuming an isotropic distribution. Particles that escape the Crystal Ball preventing a full energy measurement of the proton can be seen in the tail of events before the full energy peak which contains ~10% of the total events.

problem occurs, due to low energy charged particles entering the crystal either from a reaction in the target, or from a secondary reaction in the crystals, and being mistaken for a γ ray (the reverse situation is also possible). Additionally, the add-back procedure treats events as clusters (shown in Fig. 6.5), yet sometimes a charged particle can scatter around crystals creating secondary reactions so that it distributes its energy in a pattern that is more like the 'chain' of crystals (depicted in Fig. 6.6). These events should be identified and removed from the analysis if they prove too difficult to reconstruct. One of the advantages of using the R3BRoot simulation is the ability to observe quickly and easily how problems such as punch through, re-scattering and secondary reactions change with the energy of the incident protons/γ rays and also how the algorithms and thresholds used for the add-back procedure can be modified to cope with this.
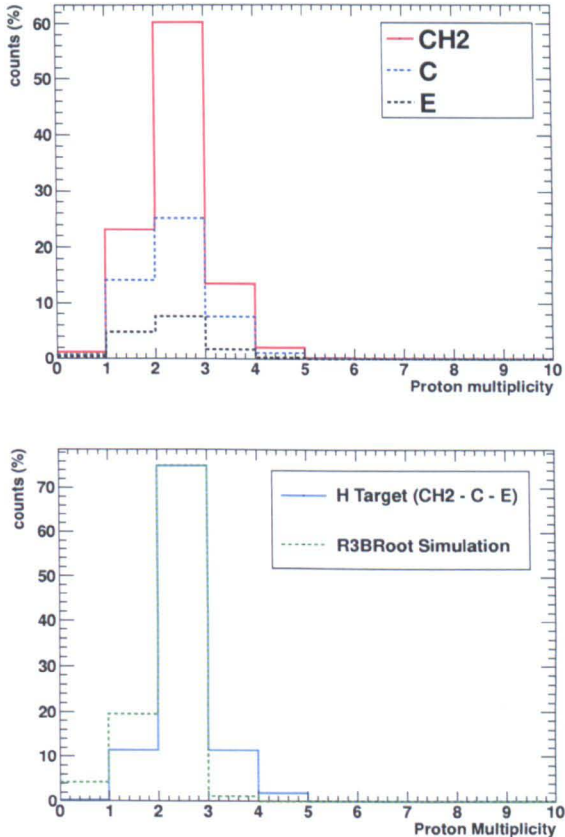
Figure 6.4: A comparison of the recoil proton multiplicity detected by the Crystal Ball for the experimental data and the R3BRoot simulation. The top figure shows the contributions to the CH_2 proton multiplicity for ^{11}B fragments with the Crystal Ball sum trigger. The bottom figure shows a comparison between the reconstructed H target data created from a subtraction of the background shown in the first figure (see section 5.2), and the R3BRoot simulation discussed in this chapter. In the analysis of the experimental and simulated data a cut is made on all events with a proton multiplicity equal to two.
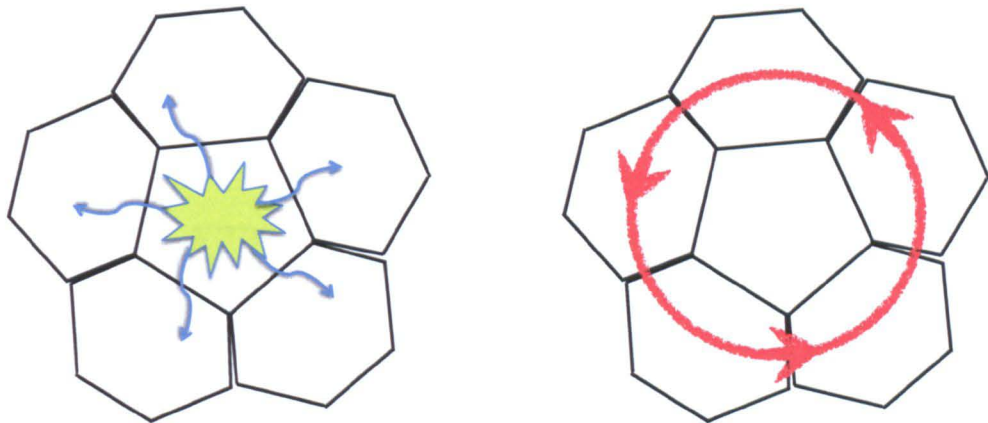
Figure 6.5: A depiction of a proton/γ-ray event that disperses its energy to multiple neighbouring crystals in the form of a cluster. The left figure shows how neighbouring crystals form the cluster, and the right figure shows that such an event is straightforward for the add-back procedure to process.
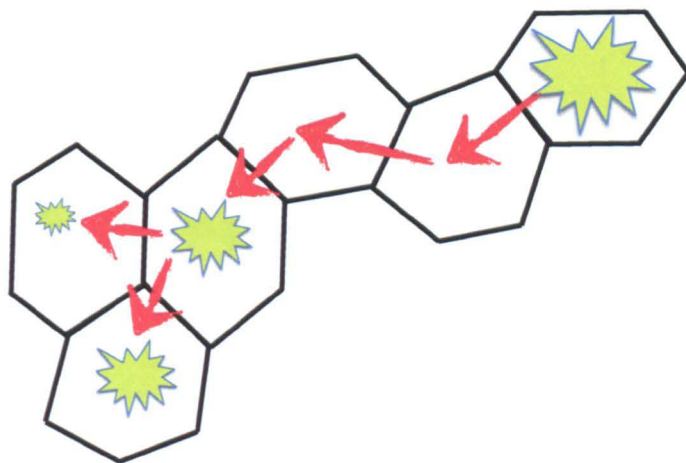
Figure 6.6: A depiction of a proton/γ-ray event that disperses its energy to neighbouring crystals in the form of a chain. A event such as this is not easy for the add-back procedure to reconstruct due to the large amount of crystals and secondary reactions involved.

6.2.3 Crystal Ball Response to High-Energy γ rays

Combining the event generator, R3BRoot and the analysis algorithms used to reconstruct the experimental data, the response of the Crystal Ball has been simulated for $^{12}C(p, 2p)^{11}B^*$ events which populate the first and third excited states in ^{11}B. The result is shown in Fig. 6.7.
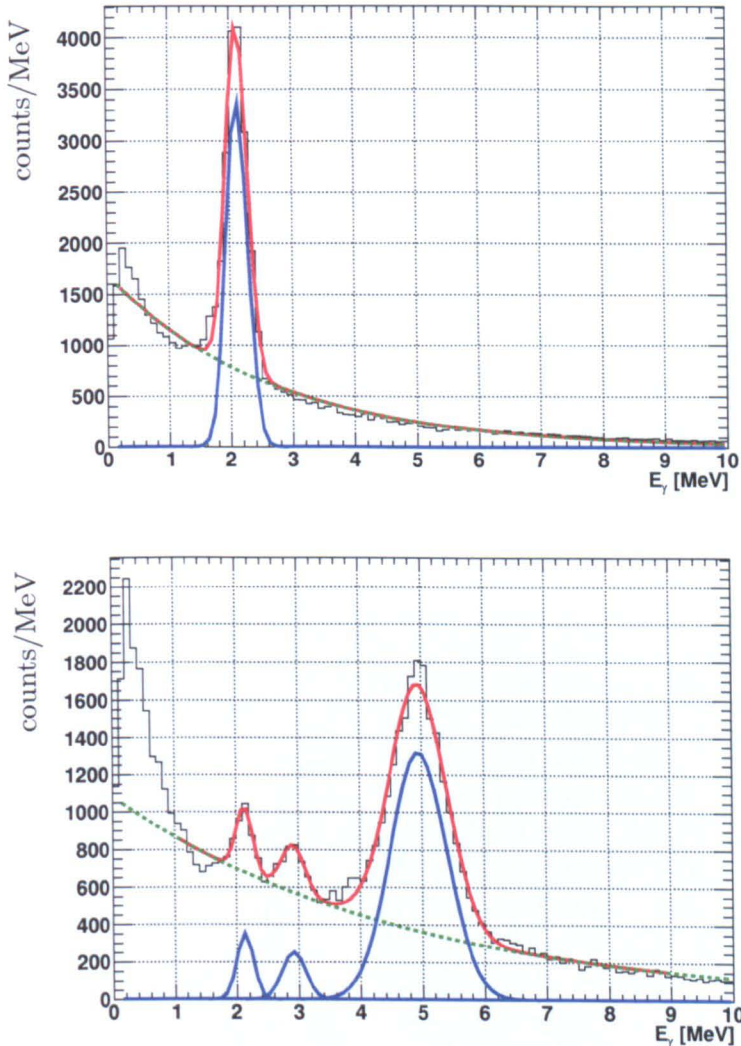
Figure 6.7: The response of the Crystal Ball to γ decays from the first and third excited states in ^{11}B after a $^{12}C(p, 2p)^{11}B$ reaction. The first figure shows the response for the 2.12 MeV state and the second figure the response to the 5.02 MeV state and its cascade (see Fig. 5.15) to the ground state.

These response functions can be used to fit the γ-ray energy spectrum shown for the experimental data in chapter 5. This allows the population of bound states in ^{11}B to be deduced, as well as an idea of the combined efficiency losses due to the geometry and

materials of the Crystal Ball and the reconstruction routines. The proportion of events populating the bound states in ^{11}B were determined by the response functions fitted to the experimental data to be: 76% occupying the ground state, 11% occupying the first excited state (2.12 MeV) and 13% occupying the third excited state (5.02 MeV). These numbers are found to be consistent with results for quasi-free scattering reactions in normal kinematics using both proton and electron probes [122].

6.3 R3BRoot and the Future R^{3}B Setup

Results from the R3BRoot simulation have been used to inform the design of the new detectors in the R^{3}B setup. In particular, consideration has been given to which materials and geometry will be most suitable for the new target-recoil detectors as well as to creating reconstruction algorithms that can be applied and tested with simulated data ready for use when the first experimental data becomes available. In this way, the simulation not only receives input from the analysis of experimental data but also helps to shape how it will be carried out. For the R^{3}B setup, the upgrade to the Crystal Ball detector is known as the CALorimeter for In-Flight emitted gAmmas (CALIFA) [123]. The proposed design for the barrel together with the end-cap section of the detector is shown below in Fig. 6.8.
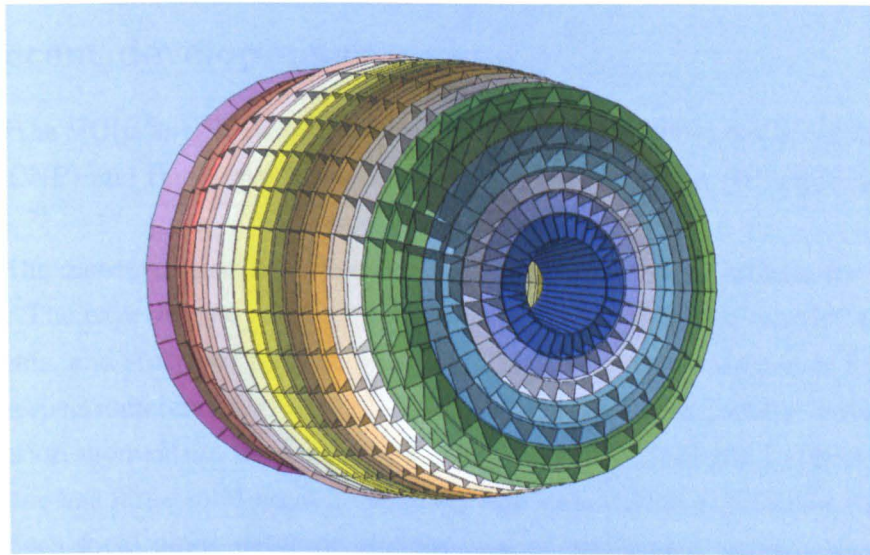
Figure 6.8: Proposed structure of the CALIFA detector made with R3BRoot. The full detector will contain four CsI crystals in each of the coloured containers (alveoli) making it a highly segmented array with ∼3000 CsI crystals in total. The crystals are up to 20 cm in length and designed to stop 300 MeV protons at forward angles. Energy resolution for γ rays is expected to be 5% (FWHM at 1 MeV), and 2% for light charged particles.

Chapter 7

Discussion of Results

In this chapter comparisons will be drawn between measurements that have been made during this analysis, and the previous work carried out with $(e, e'p)$ measurements in normal kinematics and $(p, 2p)$ measurements in both normal and inverse kinematics. Differences will be highlighted and explained and conclusions about the versatility of the reaction and methods of reconstruction will be drawn, in order to show the advantages of the LAND/R^{3}B setup for measuring quasi-free scattering reactions. Since the previous work on $(p, 2p)$ measurements is closest to the work presented in this thesis and is more recent than most of the $(e, e'p)$ measurements, the experimental setups that are in use for some of this most recent work will be discussed first.

7.1 Recent developments

Analysis of the ^{12}C$(p, 2p)^{11}$B reaction has taken place at the Research Center for Nuclear Physics (RCNP) and the Heavy Ion Medical Accelerator in Chiba (HIMAC) facilities in Japan.

At RCNP the measurements have been carried out using normal kinematics with high resolution. The experiments are limited to stable beams, as is the case for the $(e, e'p)$ measurements, and scattered protons from $(p, 2p)$ reactions are measured at fixed angles in two large spectrometers (see Fig. 7.1). The Grand Raiden spectrometer is designed for high resolution momentum measurements (p/Δp $\approx$ 37000) and the Large Acceptance Spectrometer has large solid angle ($\sim$20 msr) and momentum acceptance capabilities ($\pm$15%). Each focal plane detector is composed of two plastic scintillators and two multi-wire drift chambers [124].

At the HIMAC facility (see Fig. 7.2), $(p, 2p)$ reactions using inverse kinematics have been measured for the first time, allowing both stable and radioactive isotopes to be investigated. However because HIMAC is primarily a medical facility the range of

Grand Raiden (GR)
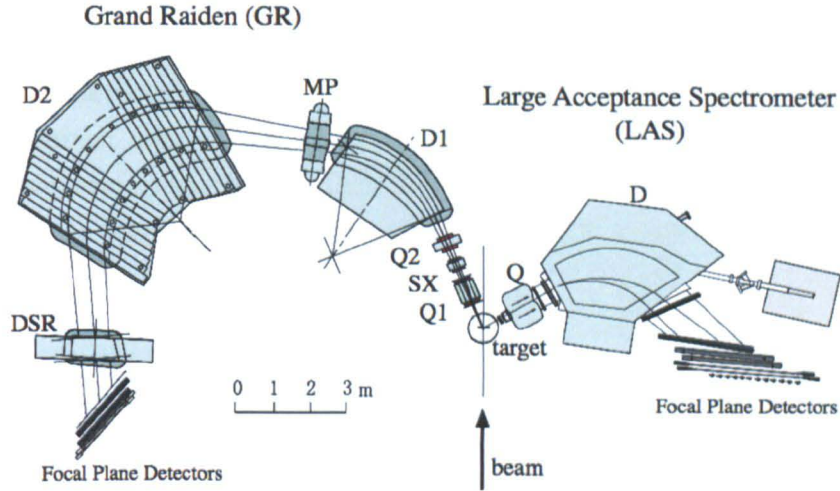
Figure 7.1: The RCNP setup for measuring $(p, 2p)$ reactions at Osaka University, Japan. Scattered protons are measured at fixed angles with high resolution, analysis of the residual fragments is not possible due to the measurement being performed using normal kinematics. Figure taken from [125].

secondary beams and energies is lower. By contrast, both the RIBF facility at RIKEN, Japan, and GSI offer a greater range of beams at larger energies and intensities and measurements with greater kinematical coverage. Currently, the SAMURAI setup at RIKEN [126] (due to come online in 2012) provides the best opportunities for kinematically complete measurements on fast radioactive beams until the FAIR facility comes online and the full R^3B setup is in use.
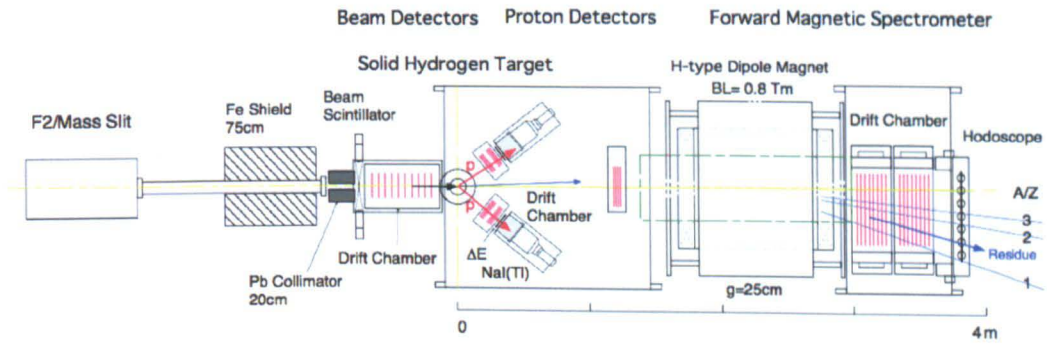
Figure 7.2: The HIMAC setup for measuring $(p, 2p)$ reactions at Chiba, Japan. Scattered protons are measured at fixed angles in NaI telescopes and analysis of the residual fragments is performed using a magnetic spectrometer after which ΔE, TOF, position and time of flight measurements are made.

Experiments at the HIMAC facility can take advantage of thick solid hydrogen

targets ($\sim$5 mm), and secondary beam intensities of 10^4 - 10^5 ions/spill depending on the isotope. Scattered protons are measured in two telescopes containing silicon and NaI scintillator detectors for energy loss and tracking measurements, which are fixed at $\pm 39°$. Fragment residues from the $(p, 2p)$ reactions travel forward before passing through a magnetic spectrometer, after which three drift chambers and a scintillator are placed for the fragment momentum analysis and ΔE and TOF measurement [83].

7.2   Momentum Distributions

For $(e, e'p)$ reactions in normal kinematics, the recoil momentum of the system is measured by analysing the momentum of the scattered electron-proton pair. An example of this measurement was carried out at the Saclay accelerator in France by Mougey *et al.* [127] and the result is shown for the $^{12}C(e, e'p)X$ reaction in Fig. 7.3. The momentum is analysed for a specific range of the excitation energy so that the recoil momentum can be presented for both the bound and the unbound states that are populated in the ^{11}B fragment.

A similar measurement but only for the momentum of protons removed from the $s_{1/2}$ state in ^{12}C was carried out using the $^{12}C(p, 2p)^{11}B$ reaction at RCNP by Noro *et al.* [128], primarily to investigate in-medium effects of nucleon-nucleon scattering. In order to minimise final state interactions and other structural effects they chose only protons that had been removed from the deeply bound $s_{1/2}$ state in ^{12}C and selected them via the excitation energy of the system as with the electron measurement discussed above. The cross section as a function of recoil momentum is shown for the s-state protons in Fig. 7.4 and the maximum can be seen around 0 MeV/c where the cross section for proton removal from the s-state is expected to be maximal. This is consistent with the electron measurement presented in Fig. 7.3.

Further to this, the transverse momentum of recoiling fragments has been measured in coincidence with the $^{9-16}C(p, 2p)X$ reactions at the HIMAC facility for a secondary beam of energy 250 MeV.A [83]. The results are shown in Fig. 7.5 and the measurement for $^{12}C(p, 2p)^{11}B$ (proton removal from the p-shell of ^{12}C) is consistent with the momentum distributions shown in Fig. 7.3 and Fig. 7.4 [83].

Both the $(e, e'p)$ and $(p, 2p)$ distributions for the proton removal from the p-state are consistent with the result presented in this thesis (Fig 5.11), each of these distributions showing a maximum at $\sim$100 MeV/c. The width of the momentum distributions for the p-state compared to the width of the s-state could not be confirmed in this analysis due to the inability to measure the energy and momentum of the scattered protons accurately.
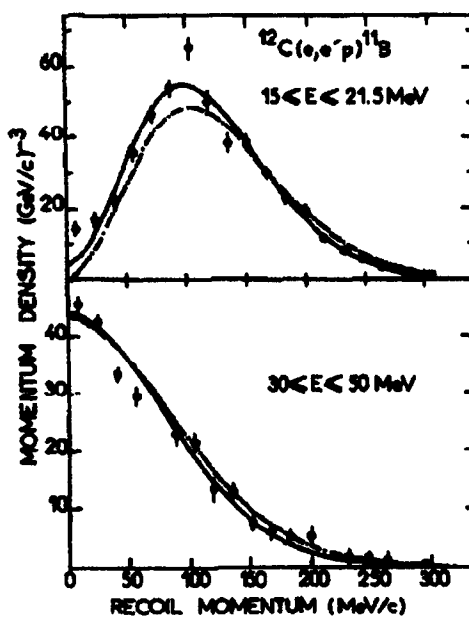
Figure 7.3: Momentum distribution produced with the $^{12}C(e, e'p)X$ reaction at Saclay with a 497 MeV electron beam. Proton-electron pairs emerging from the target are collected at fixed angles and their momentum analysed. The top figure shows the recoil momentum for protons removed from the $p_{3/2}$ state in ^{12}C populating bound states in ^{11}B, the bottom figure shows the recoil momentum for protons removed from the $s_{1/2}$ state in ^{12}C populating unbound states in ^{11}B. The momentum distributions for each state are constructed in coincidence with a condition on the energy of the scattered electron-proton pair to ensure that they represent both shells in ^{12}C. Figures taken from [127].
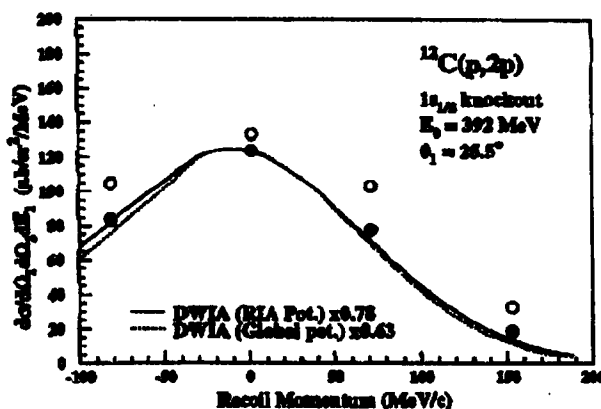
Figure 7.4: Differential cross section as a function of momentum produced with the $^{12}C(p, 2p)X$ reaction at RCNP with a 392 MeV proton beam. Protons removed from the $s_{1/2}$ state in ^{12}C and populating unbound states in ^{11}B are selected using kinematics and a condition on the energy of the scattered proton pair. Figure taken from [128].
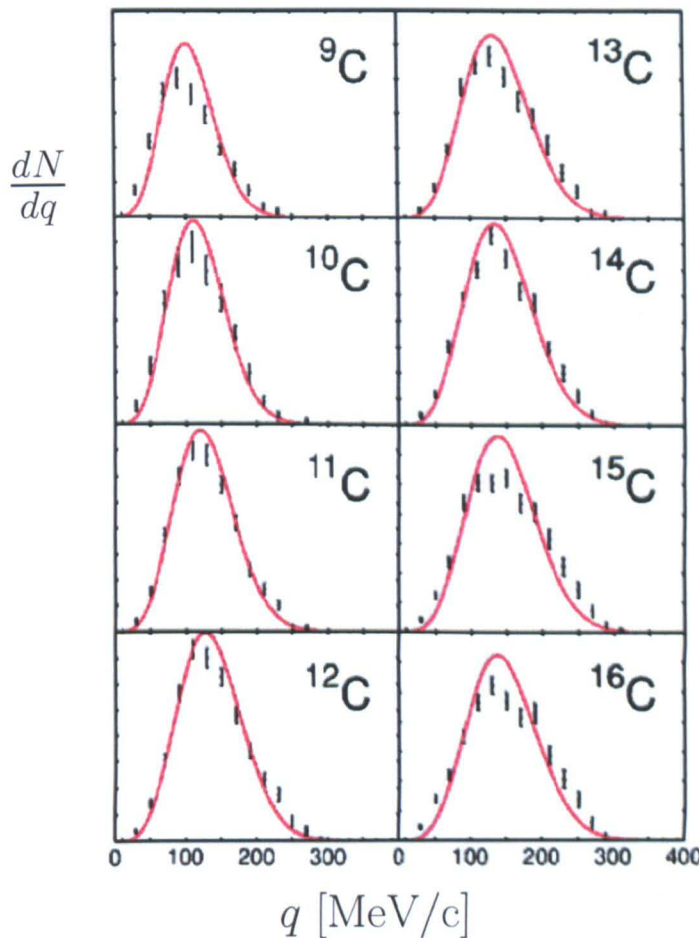
Figure 7.5: Momentum distributions for protons measured in coincidence with the $^{9-16}$C$(p, 2p)X$ reactions. Each distribution has been fitted with a harmonic oscillator function of the form: $\frac{dN}{dq} \propto q^{2\ell+2} exp(-q^2/\sigma_\ell^2)$ where ℓ is the angular momentum, q the momentum and σ the width of the distribution. Figure modified from [83].

7.3 Excitation Energy

An early measurement comparing the $(p, 2p)$ and (p, pn) reactions on ^{2}H and ^{12}C was carried out at the TRIUMF laboratory in Canada [129]. The excitation energy for ^{11}B was reconstructed by measuring scattered protons at fixed angles, in coincidence with the ^{12}C$(p, 2p)^{11}$B reaction and is shown in Fig. 7.6 where the separation of the *s*-state and the *p*-state can be seen.
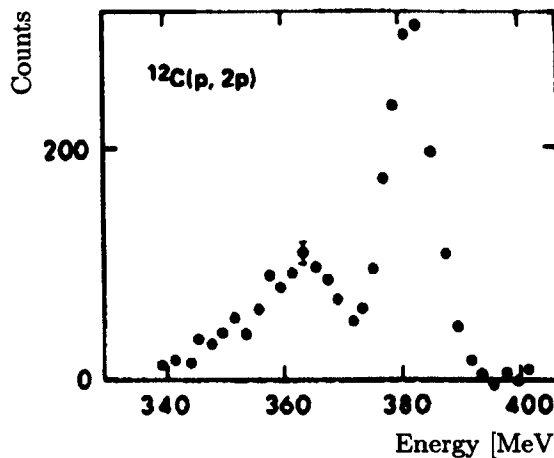
Figure 7.6: An early measurement of the excitation energy spectrum of ^{11}B reconstructed by measuring protons in coincidence with the ^{12}C$(p, 2p)^{11}$B reaction at 400 MeV.A. Protons removed from the *p*-state in ^{12}C are seen at a missing energy of ~20 MeV and protons removed from the *s*-state in ^{12}C have a missing energy of ~40 MeV. This experiment was carried out in normal kinematics at the TRIUMF facility in 1979. Figure adapted from [129].

Early measurements of the excitation energy using quasi-free scattering reactions were made using $(e, e'p)$ measurements with the lightest nuclei all the way up to Pb (see chapter 2). An example of excitation energy spectra obtained from the ^{12}C$(e, e'p)X$ reactions is shown in Fig. 7.7 where different parts of the cross section have been identified by a selection on the momentum transferred to the electron-proton pair emerging from the target.

Systematic measurements of the excitation energy obtained for the boron isotopes via the $^{9-16}$C$(p, 2p)X$ reactions at 250 MeV.A from HIMAC are shown in Fig. 7.8. The authors present the excitation energy for bound (B), unbound (C) and both bound and unbound (A) states separated by selecting events with/without a surviving boron fragment and then measuring the energy of the protons in coincidence with this condition.
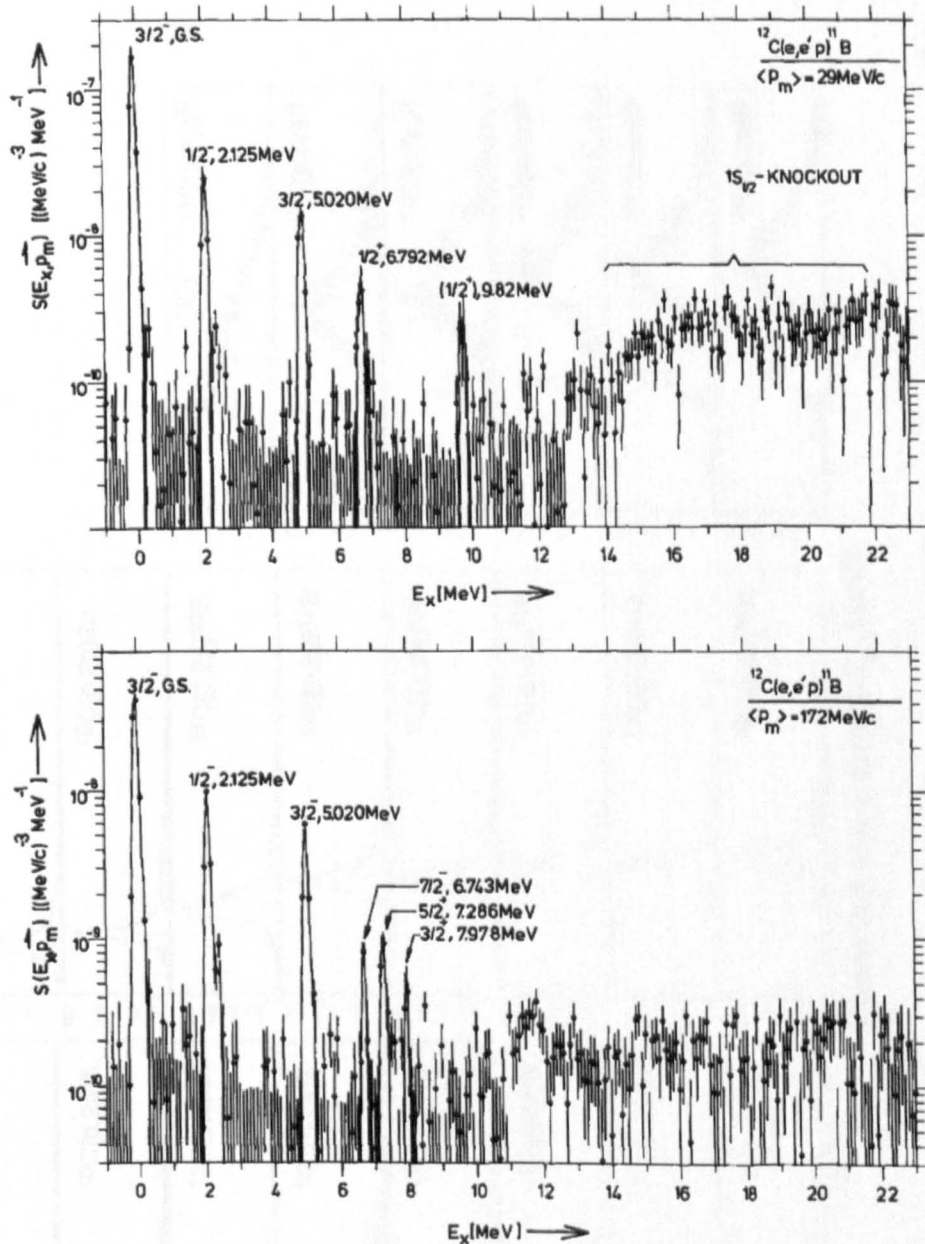
Figure 7.7: Excitation energy spectra for ^{11}B measured in coincidence with the ^{12}C$(e, e'p)X$ reaction and a specific value of momentum transferred to the outgoing electron-proton pair. The top figure shows a high resolution measurement made with a low momentum transfer of 29 MeV/c where proton removal from the s-state in ^{12}C dominates. The bottom figure shows the same distribution for a high momentum transfer of 172 MeV/c where proton removal from the p-state in ^{12}C dominates. Figures taken from [130].
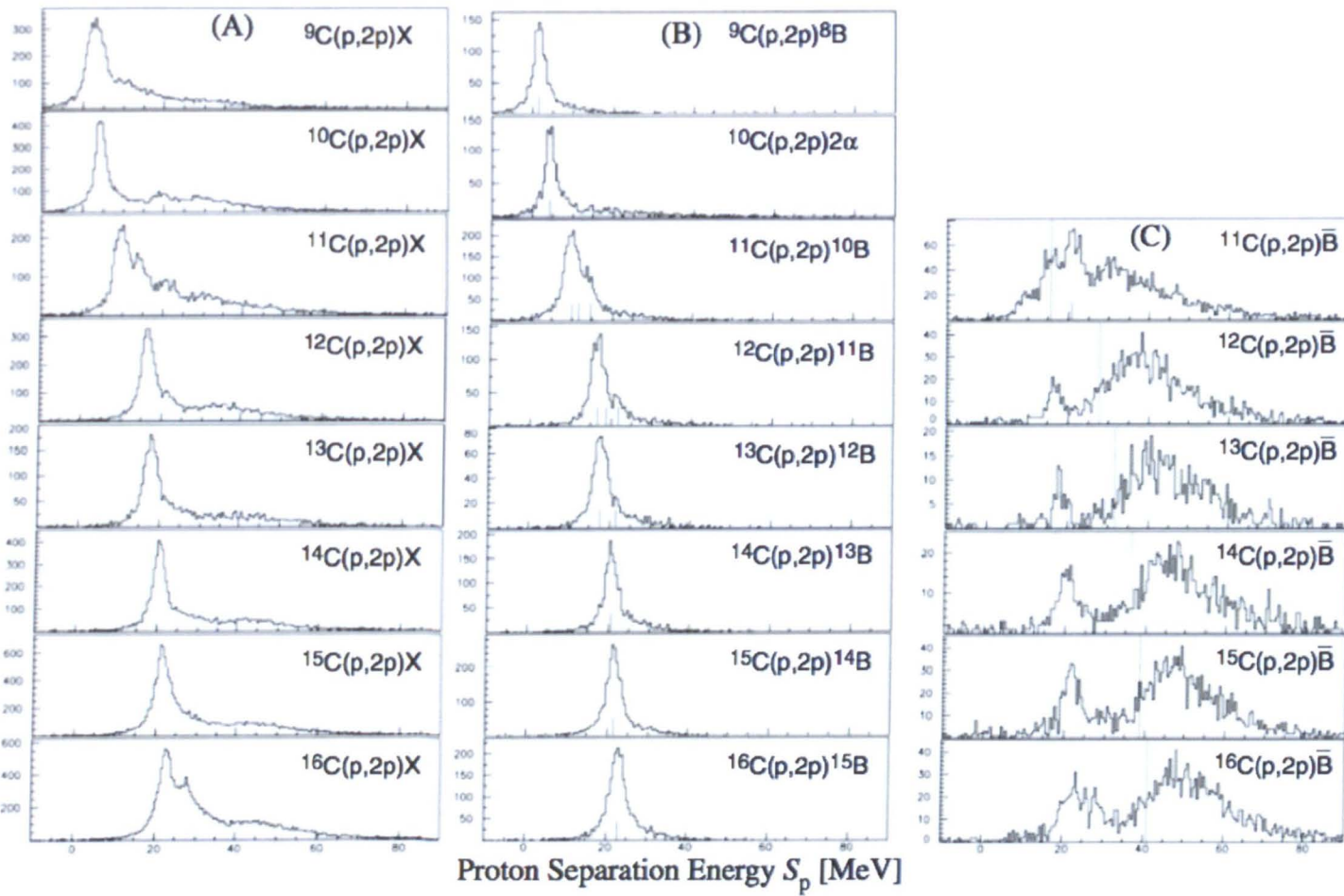
Figure 7.8: Excitation energy for all bound (B), unbound (C) and both bound and unbound (A) states populated by the $^{9-16}$C$(p,2p)X$ reactions at 250 MeV.A at the HIMAC facility. Figure taken from [83].
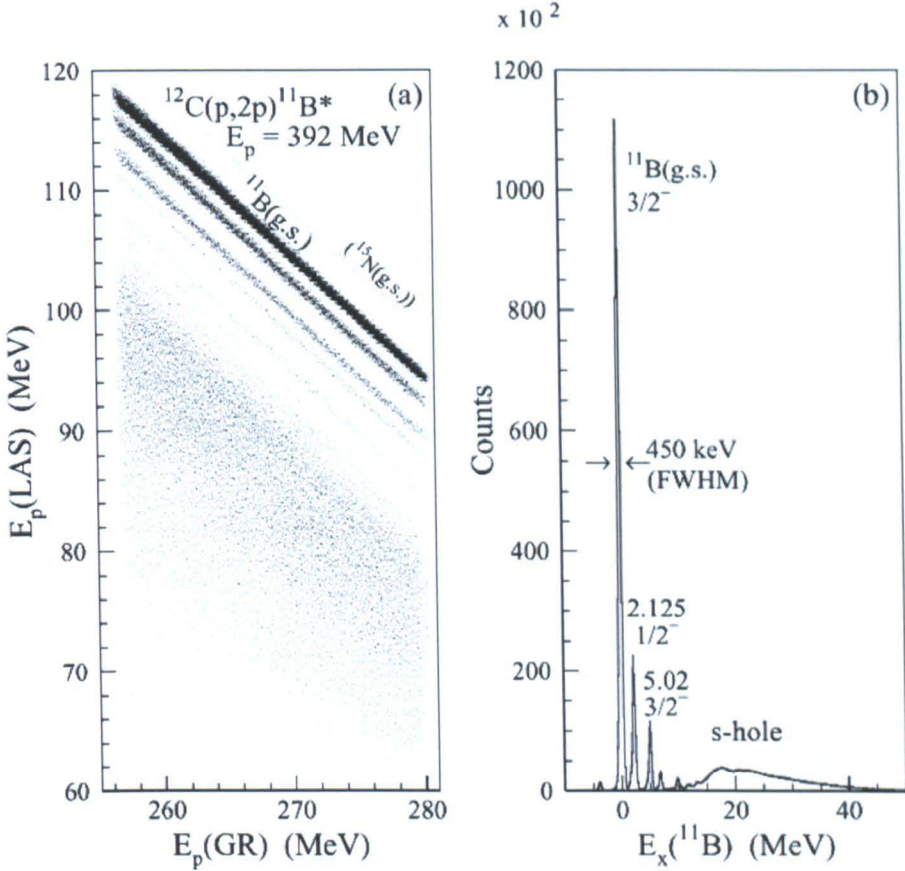
Figure 7.9: Excitation energy spectrum of ^{11}B measured in coincidence with the ^{12}C$(p, 2p)^{11}$B* reaction at 392 MeV.A. This experiment took place in normal kinematics with the Grand Raiden and Large Acceptance Spectrometer at the RCNP facility in Osaka University, Japan. A small amount of contamination is visible from ^{15}N due to a previous measurement of ^{16}O$(p, 2p)$. Figure taken from [125].

The excitation energy spectrum of ^{11}B presented in this thesis (Fig. 5.19) compares well to the distributions presented here for previous work done with $(e, e'p)$ and $(p, 2p)$ reactions. When comparing the results presented in this thesis with the recent results from the RCNP facility in normal kinematics (Fig. 7.9), it is apparent that the resolution of the measurement, while not comparable still enables the main structural features of ^{11}B to be observed. This includes the ground and first excited states corresponding to proton removal from the p-shell of ^{12}C, and the unbound states in ^{11}B corresponding to proton removal from the s-shell of ^{12}C. Measurements at the HIMAC facility using inverse kinematics represent the first time that $(p, 2p)$ reactions have been carried out on stable and radioactive isotopes of carbon at the same time. However, the GSI setup is more suited to these measurements since it offers a full solid angle measurement along with better momentum and energy resolution for analysis of the recoiling fragments.

This difference in resolution can be seen when comparing the final excitation energy spectra, in particular the separation of states in the p-shell.

7.4 Integrated Cross Section Measurements

For comparison of the proton removal cross sections presented in this thesis, the paper by Kidd *et al.* [131] is used. They report on measurements of the proton removal cross section from ^{12}C using a carbon target at beam energies of 250, 1050 and 2100 MeV.A at the Bevalac accelerator in Berkeley, California. The measurement presented in this thesis is shown alongside this previous work in Fig. 7.10.
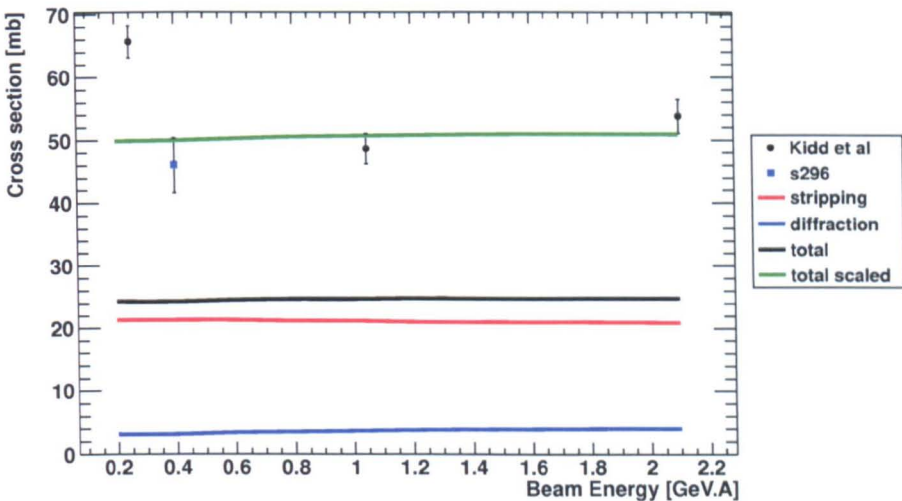
Figure 7.10: A comparison of ^{12}C(^{12}C,^{11}B)X cross sections with different beam energies. The value presented in chapter 5.2 is the data point labelled 's296' and is consistent with the theoretical calculation shown as the green line [132]. The software for calculating the cross sections presented here is based upon the approximations and formulae discussed in section 2.2 [133, 134].

A clear discrepancy between the low energy measurement by Kidd *et al.* and the measurement presented in this thesis (45.9±4.4 mb) is apparent. However, the agreement with the theoretical calculation presented here and the two values at higher energy suggest that the measurement presented in this thesis could be the more accurate one. This discrepancy between the low energy and high energy points is commented on in the paper by Brown *et al.* [135] in which they discard the cross section at 250 MeV.A and instead take an average cross section from the 1050 and 2100 MeV.A points for their calculations.

There are few data for comparing the proton removal cross section from ^{12}C with the reconstructed H target. An integrated cross section measurement in the paper by

Gooding and Pugh [136] gives a value of 16±4 mb measured using normal kinematics with a proton beam energy of 153 MeV on a C target. This is in agreement with our measurement of 18.4±2.7 mb within the errors specified. Theoretical support for nucleon removal with a proton target is not yet fully available. The cross section measurements made for the H target in this thesis, will thus be useful points of comparison when the formalism is developed.

Chapter 8

Conclusions and Future Work

The goals of the quasi-free scattering program at R^3B (outlined in chapter 1) are to investigate single-particle properties in nuclei and the modification of the nucleon-nucleon interaction within nuclear matter. The experiment reported on in this thesis was carried out in order to obtain a data set for a stable beam that would put a limit on the various observables associated with these objectives for measurements made with radioactive beams and inverse kinematics. This first objective has been completed, using for the first time, the invariant-mass method combined with in-beam γ-ray spectroscopy for analysis of the decaying forward fragments created with $(p, 2p)$ reactions. This involved the use of all detectors surrounding the target, and after the ALADIN magnet, as well as a detailed simulation of the target-recoil detectors, in order to determine their response to events where charged particles and γ rays must be detected and measured together.

Measurements of the fragment momentum distribution and the proton removal cross section for bound states have been made using a C target, and compared with previous measurements, as well as with theoretical calculations. Using the same analysis method, the same measurements have been extracted for the reconstructed H target where a theoretical framework is not yet established. The excitation energy spectrum of ^{11}B is a promising result that is consistent with previous experiments in normal kinematics and evidence of nucleon removal from the deeply bound s-state in ^{12}C is observed. However, the cross section for nucleon removal from this state has been difficult to extract, due to the construction of the reaction trigger and acceptance losses for some isotopes that proved difficult to correct for. The additional objective of measuring the momentum and energy of the scattered protons allowing a comparison with the fragment data and investigation of the nucleon-nucleon interaction within ^{12}C has not been possible. This is due to the unsuccessful high energy calibration of the calorimeter surrounding the target. It has, however, been possible to measure the angular distribution of the protons emerging from the target with a higher precision than has been possible with previous experiments, allowing a very clean way of observing $(p, 2p)$ events in the

analysis. Many of the difficulties encountered during the analysis of this experiment have led to development of dedicated correction algorithms and where possible, the addition of extra detectors to the current setup for experiments that have been carried out since.
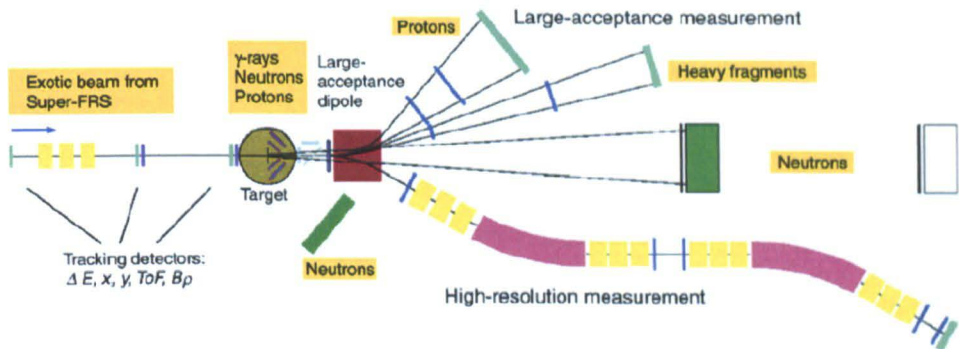
Figure 8.1: A schematic of the future R^3B setup that will be in operation at the FAIR facility. Most of the detectors will be based upon similar principles to ones being used in the current LAND/R^3B setup, but will have greater acceptance and resolution capabilities. The main difference with the current setup is the ability to operate in either a high acceptance or high resolution mode. Image taken from [20].

Conclusions concerning the upgrade and design of detectors for the future full R^3B setup at FAIR have been drawn both from the data set produced in this work as well as the simulations that have been carried out for the response of the target-recoil detectors. Attention to the geometry and materials proposed for the design of the target-recoil detectors, in particular at their forward angles into which the highly focused cone of high-energy reactions products and scattered particles will be directed, has led to the design of longer crystals at forward angles, and additional layers of silicon that will enable more comprehensive ΔE-E measurements of scattered protons to take place. The future R^3B setup is depicted in the schematic shown in Fig. 8.1, where much of the upgrade consists of re-designing the existing detectors to enhance their acceptance and resolution, allowing cleaner measurements at higher energy and intensity as well as experiments that probe the drip lines. Analysis of the experiment reported on in this thesis continues, with promising results from the simulations reported on in chapter 6 opening up the possibility of measuring exclusive cross sections and spectroscopic factors for the excited states observed in ^{11}B. Additionally to this, characterisation of other more experimentally challenging channels such as the proton induced (p,pn) and $(p,p\alpha)$ reactions should soon be possible.

Bibliography

[1] E. Rutherford. The scattering of the alpha and beta rays and the structure of the atom. *Proc. Manchester Lit Phil Soc*, IV(55):18–20, 1911.

[2] H. A. Bethe and R. F. Bacher. Stationary States of Nuclei. *Reviews of Modern Physics*, 8(2):82–229, April 1936.

[3] M. Mayer. On Closed Shells in Nuclei. *Physical Review*, 74(3):235–239, August 1948.

[4] O. Haxel, J. Jensen, and H. Suess. On the "Magic Numbers" in Nuclear Structure. *Physical Review*, 75(11):1766–1766, June 1949.

[5] R. F. Casten. *Nuclear Structure from a Simple Perspective (Oxford Studies in Nuclear Physics)*. OUP USA, 1990.

[6] R. D. Woods and D. S. Saxon. Diffuse Surface Optical Model for Nucleon-Nuclei Scattering. *Physical Review*, 95:577, 1954.

[7] J. Dobaczewski, W. Nazarewicz, T. Werner, J. Berger, C. Chinn, and J. Decharge. Mean-field description of ground-state properties of drip-line nuclei: Pairing and continuum effects. *Physical Review C*, 53(6):2809–2840, June 1996.

[8] P. Adrich, A. Klimkiewicz, and M. Fallot. Evidence for Pygmy and Giant Dipole Resonances in ^{130}Sn and ^{132}Sn. *Physical Review Letters*, 95:132501, 2005.

[9] A. Klimkiewicz, N. Paar, and P. Adrich. Nuclear symmetry energy and neutron skins derived from pygmy dipole resonances. *Physical Review C*, 76:051603, 2007.

[10] G. D. Alkhazov, M. N. Andronenko, A. V. Dobrovolsky, P. Egelhof, G. E. Gavrilov, H. Geissel, H. Irnich, A. V. Khanzadeev, G. A. Korolev, and A. A. Lobodenko. Nuclear Matter Distributions in 6He and 8He from Small Angle p-He Scattering in Inverse Kinematics at Intermediate Energy. *Physical Review Letters*, 78(12):2313–2316, 1997.

[11] T. Otsuka, R. Fujimoto, Y. Utsuno, A. Brown, M. Honma, and T. Mizusaki. Magic numbers in exotic nuclei and spin-isospin properties of the NN interaction. *Physical Review Letters*, 87:082502-1, 2001.

[12] J. Dobaczewski, I. Hamamoto, W. Nazarewicz, and J. A. Sheikh. Nuclear shell structure at particle drip lines. *Physical Review Letters*, 72:981, 1994.

[13] B. Chen, J. Dobaczewski, and K. L. Kratz. Influence of shell-quenching far from stability on the astrophysical r-process. *Physics Letters B*, 355:37-44, 1995.

[14] T. Otsuka, T. Suzuki, R. Fujimoto, H. Grawe, and Y. Akaishi. Evolution of Nuclear Shells due to the Tensor Force. *Physical Review Letters*, 95(23), November 2005.

[15] L. Gaudefroy, O. Sorlin, D. Beaumel, Y. Blumenfeld, Z. Dombrádi, S. Fortier, S. Franchoo, M. Gélin, J. Gibelin, S. Grévy, and Others. Reduction of the Spin-Orbit Splittings at the N= 28 Shell Closure. *Physical Review Letters*, 97(9):92501, 2006.

[16] FAIR Green Paper - The Modularized Start Version: http://www.fair-center.de/fileadmin/fair/publications_FAIR/FAIR_GreenPaper_2009.pdf. Technical report, GSI, 2009.

[17] FAIR Webpage: http://www.gsi.de/portrait/fair/beschleuniger_e.html.

[18] G. Rosner. Future Facility: FAIR at GSI. *Nuclear Physics B - Proceedings Supplements*, 167:77-81, 2007.

[19] R. Krücken and the NuSTAR Collaboration. The NuSTAR facilty at FAIR. *Journal of Physics G: Nuclear and Particle Physics*, 31(10):S1807-S1811, October 2005.

[20] T. Aumann. Prospects of nuclear structure at the future GSI accelerators. *Progress in Particle and Nuclear Physics*, 59(1):3-21, July 2007.

[21] R3B Letter of Intent: http://www.gsi.de/forschung/kp/kr/R3B_e.html.

[22] R. C. Lemmon, T. Nilsson, and O. Kiselev. Quasifree Hadronic Scattering Studies of Exotic Nuclei, GSI Experiment proposal: S296 (unpublished). Technical report, STFC Daresbury, 2004.

[23] F. Wamers. *Quasi-Free-Scattering and One-Proton-Removal Reactions with the Proton-Dripline Nucleus ^{17}Ne at Relativistic Beam Energies*. PhD thesis, TU-Darmstadt, 2011.

[24] J. Chadwick, A. N. May, T. G. Pickavance, and C. F. Powell. An Investigation of the Scattering of High-Energy Particles from the Cyclotron by the Photographic Method. *Proceedings of the Royal Society A: Mathematical, Physical and Engineering Sciences*, 183(992):1–25, August 1944.

[25] S. T. Butler. Angular Distributions from (d,p) and (d,n) Nuclear Reactions. *Proceedings of the Royal Society A: Mathematical, Physical and Engineering Sciences*, 208(1095):559–579, September 1951.

[26] Daphne. F Jackson. *Nuclear Reactions - Google Books*. Taylor & Francis, Library of Congress. Aerospace Technology Division, 1961.

[27] P.G. Hansen and J.A. Tostevin. Direct Reactions with exotic nuclei. *Annual Review of Nuclear and Particle Science*, 53:219–261, November 2003.

[28] NSCL Whitepaper: http://www.nscl.msu.edu/future/nsclwhitepaper2006. Technical report, NSCL, 2006.

[29] A. Gade, P. Adrich, D. Bazin, M. D. Bowen, B. A. Brown, C. M. Campbell, J. M. Cook, T. Glasmacher, P. G. Hansen, K. Hosier, S. McDaniel, D. McGlinchery, A. Obertelli, K. Siwek, L. A. Riley, J. A. Tostevin, and D. Weisshaar. Reduction of spectroscopic strength: Weakly-bound and strongly-bound single-particle states studied using one-nucleon knockout reactions. *Physical Review C*, 77(4), April 2008.

[30] T. Aumann. Reactions with fast radioactive beams of neutron-rich nuclei. *The European Physical Journal A*, 26(3):441–478, January 2006.

[31] N. Austern. *Direct nuclear reaction theories*. John Wiley & Sons Inc, 1970.

[32] R. C. Johnson. Contribution of Deuteron Breakup Channels to Deuteron Stripping and Elastic Scattering. *Physical Review C*, 1(3):976–990, March 1970.

[33] J. Harvey and R. Johnson. Influence of Breakup Channels on the Analysis of Deuteron Stripping Reactions. *Physical Review C*, 3(2):636–645, February 1971.

[34] N. K. Timofeyuk and R. C. Johnson. Deuteron stripping and pick-up on halo nuclei. *Physical Review C*, 59(3):1545–1554, March 1999.

[35] W.N. Catford. Nucleon transfer studies with radioactive beams. *Nuclear Physics A*, 701(1-4):1–6, April 2002.

[36] M. S. Chowdhury and H. M. Sen Gupta. A study of nuclear structure in ^{59}Ni from the (d,p) reaction on ^{58}Ni. *Nuclear Physics A*, 205(3):454–474, 1973.

[37] K. Rehm, F. Borasi, C. Jiang, D. Ackermann, I. Ahmad, B. Brown, F. Brumwell, C. Davids, P. Decrock, S. Fischer, J. Görres, J. Greene, G. Hackmann, B. Harss, D. Henderson, W. Henning, R. Janssens, G. McMichael, V. Nanal, D. Nisius, J. Nolen, R. Pardo, M. Paul, P. Reiter, J. Schiffer, D. Seweryniak, R. Segel, M. Wiescher, and A. Wuosmaa. Study of the ^{56}Ni$(d,p)^{57}$Ni Reaction and the Astrophysical ^{56}Ni$(p,\gamma)^{57}$Cu Reaction Rate. *Physical Review Letters*, 80(4):676–679, January 1998.

[38] M. Labiche, W.N. Catford, R.C. Lemmon, C.N. Timis, R. Chapman, N.A. Orr, B. Fernández-Domínguez, G. Moores, N.L. Achouri, and N. Amzal. TIARA: A large solid angle silicon array for direct reaction studies with radioactive beams. *Nuclear Instruments and Methods in Physics Research Section A: Accelerators, Spectrometers, Detectors and Associated Equipment*, 614(3):439–448, March 2010.

[39] J.C. Lighthall, B.B. Back, S.I. Baker, S.J. Freeman, H.Y. Lee, B.P. Kay, S.T. Marley, K.E. Rehm, J.E. Rohrer, J.P. Schiffer, D.V. Shetty, A.W. Vann, J.R. Winkelbauer, and A.H. Wuosmaa. Commissioning of the HELIOS spectrometer. *Nuclear Instruments and Methods in Physics Research Section A: Accelerators, Spectrometers, Detectors and Associated Equipment*, 622(1):97–106, 2010.

[40] W. N. Catford, C. N. Timis, R. C. Lemmon, M. Labiche, N. A. Orr, B. Fernández-Domínguez, R. Chapman, M. Freer, M. Chartier, H. Savajols, M. Rejmund, N. L. Achouri, N. Amzal, N. I. Ashwood, T. D. Baldwin, M. Burns, L. Caballero, J. M. Casadjian, N. Curtis, G. de France, W. Gelletly, X. Liang, S. D. Pain, V. P. E. Pucknell, B. Rubio, O. Sorlin, K. Spohr, Ch. Theisen, and D. D. Warner. Migration of Nuclear Shell Gaps Studied in the $d(^{24}$Ne,p$\gamma)^{25}$Ne Reaction. *Physical Review Letters*, 104(19):192501, May 2010.

[41] B. Fernández-Domínguez, J. Thomas, W. Catford, F. Delaunay, S. Brown, N. Orr, M. Rejmund, M. Labiche, M. Chartier, N. Achouri, H. Al Falou, N. Ashwood, D. Beaumel, Y. Blumenfeld, B. Brown, R. Chapman, N. Curtis, C. Force, G. de France, S. Franchoo, J. Guillot, P. Haigh, F. Hammache, V. Lapoux, R. Lemmon, F. Maréchal, A. Moro, X. Mougeot, B. Mouginot, L. Nalpas, A. Navin, N. Patterson, B. Pietras, E. Pollacco, A. Leprince, A. Ramus, J. Scarpaci, N. de Séréville, I. Stephan, O. Sorlin, and G. Wilson. Emergence of the N=16 shell gap in ^{21}O. *Physical Review C*, 84(1), July 2011.

[42] R. Kanungo. Structure of light neutron-rich nuclei through nucleon transfer and knockout reactions. *Nuclear Physics A*, 834:505c–508c, 2010.

[43] A. Gillibert, N. Alamanos, M. Alvarez, F. Auger, D. Beaumel, E. Becheva, Y. Blumenfeld, R. Dayras, F. Delaunay, A. Drouart, G. de France, L. Giot, B. Jurado, N. Keeley, K.W. Kemper, V. Lapoux, W. Mittig, X. Mougeot, L. Nalpas, A. Obertelli, and et Al. Structure of exotic nuclei from direct reactions. *Nuclear Physics A*, 787:423–432, 2007.

[44] J.A. Cizewski, K.L. Jones, S.D. Pain, J.S. Thomas, C. Baktash, D.W. Bardayan, J.C. Blackmon, C. Gross, J.F. Liang, D. Shapira, M.S. Smith, R.L. Kozub, B.H. Moazen, C.D. Nesaraja, H.K. Carter, M.S. Johnson, R.P. Fitzgerald, D.W. Visser, U. Greife, R.J. Livesay, and et Al. Neutron transfer reactions with neutron-rich radioactive ion beams. *Nuclear Instruments and Methods in Physics Research Section B: Beam Interactions with Materials and Atoms*, 241:200–203, 2005.

[45] K. L. Jones, A. S. Adekola, D. W. Bardayan, J. C. Blackmon, K. Y. Chae, K. A. Chipps, J. A. Cizewski, L. Erikson, C. Harlin, R. Hatarik, R. Kapler, R. L. Kozub, J. F. Liang, R. Livesay, Z. Ma, B. H. Moazen, C. D. Nesaraja, F. M. Nunes, S. D. Pain, N. P. Patterson, D. Shapira, J. F. Shriner, M. S. Smith, T. P. Swan, and J. S. Thomas. The magic nature of ^{132}Sn explored through the single-particle states of ^{133}Sn. *Nature*, 465(7297):454–7, May 2010.

[46] T. Symons, Y. Viyogi, G. Westfall, P. Doll, D. Greiner, H. Faraggi, P. Lindstrom, D. Scott, H. Crawford, and C. McParland. Observation of New Neutron-Rich Isotopes by Fragmentation of 205-MeV/Nucleon ^{40}Ar Ions. *Physical Review Letters*, 42(1):40–43, January 1979.

[47] G. Westfall, T. Symons, D. Greiner, H. Heckman, P. Lindstrom, J. Mahoney, A. Shotter, D. Scott, H. Crawford, C. McParland, T. Awes, C. Gelbke, and J. Kidd. Production of Neutron-Rich Nuclides by Fragmentation of 212-MeV/amu ^{48}Ca. *Physical Review Letters*, 43(25):1859–1862, December 1979.

[48] K. S. Krane. *Introductory Nuclear Physics*. John Wiley & Sons, 1987.

[49] I. Tanihata, H. Hamagaki, O. Hashimoto, Y. Shida, N. Yoshikawa, K. Sugimoto, O. Yamakawa, T. Kobayashi, and N. Takahashi. Measurements of Interaction Cross Sections and Nuclear Radii in the Light p-Shell Region. *Physical Review Letters*, 55(24):2676–2679, December 1985.

[50] I. Tanihata, T. Kobayashi, O. Yamakawa, S. Shimoura, K. Ekuni, K. Sugimoto, N. Takahashi, T. Shimoda, and H. Sato. Measurement of interaction cross sections using isotope beams of Be and B and isospin dependence of the nuclear radii. *Physics Letters B*, 206(4):592–596, June 1988.

[51] P. G. Hansen and B. Jonson. The neutron halo of extremely neutron-rich nuclei. *Europhysics Letters*, 4(4):409–414, August 1987.

[52] A. S. Jensen, K. Riisager, and D. V. Fedorov. Rev. Mod. Phys. 76, 215 (2004): Structure and reactions of quantum halos. *Reviews of Modern Physics*, 76(1):215–261, February 2004.

[53] A. Navin, D. Anthony, T. Aumann, T. Baumann, D. Bazin, Y. Blumenfeld, B. Brown, T. Glasmacher, P. Hansen, R. Ibbotson, P. Lofy, V. Maddalena, K. Miller, T. Nakamura, B. Pritychenko, B. Sherrill, E. Spears, M. Steiner, J. Tostevin, J. Yurkon, and A. Wagner. Direct Evidence for the Breakdown of the N=8 Shell Closure in ^{12}Be. *Physical Review Letters*, 85(2):266–269, July 2000.

[54] J. Terry, D. Bazin, B. Brown, C. Campbell, J. Church, J. Cook, A. Davies, D. Dinca, J. Enders, and A. Gade. Physics Letters B : Direct evidence for the onset of intruder configurations in neutron-rich Ne isotopes. *Physics Letters B*, 640(3):86–90, September 2006.

[55] J. Al-Khalili and F. Nunes. Reaction models to probe the structure of light exotic nuclei. *Journal of Physics G: Nuclear and Particle Physics*, 29(11):R89–R132, November 2003.

[56] E. Sauvan, F. Carstoiu, N.A. Orr, J.C. Angélique, W.N. Catford, N.M. Clarke, M. Mac Cormick, N. Curtis, M. Freer, S. Grévy, C. LeBrun, M. Lewitowicz, E. Liégard, F.M. Marqués, P. Roussel-Chomaz, M.G. SaintLaurent, M. Shawcross, and J.S. Winfield. One-neutron removal reactions on neutron-rich psd-shell nuclei. *Physics Letters B*, 491(1-2):1–7, October 2000.

[57] A. Sakharuk and V. Zelevinsky. Particle removal reactions with deformed projectiles. *Physical Review C*, 61(1), December 1999.

[58] J. A. Tostevin. Core excitation in halo nucleus break-up. *Journal of Physics G: Nuclear and Particle Physics*, 25:735, 1999.

[59] A. Gade, D. Bazin, B. Brown, C. Campbell, J. Church, D. Dinca, J. Enders, T. Glasmacher, P. Hansen, Z. Hu, K. Kemper, W. Mueller, H. Olliver, B. Perry, L. Riley, B. Roeder, B. Sherrill, J. Terry, J. Tostevin, and K. Yurkewicz. One-neutron knockout reactions on proton-rich nuclei with N=16. *Physical Review C*, 69(3), March 2004.

[60] D. Bazin, B. Brown, C. Campbell, J. Church, D. Dinca, J. Enders, A. Gade, T. Glasmacher, P. Hansen, W. Mueller, H. Olliver, B. Perry, B. Sherrill, J. Terry,

and J. Tostevin. New Direct Reaction: Two-Proton Knockout from Neutron-Rich Nuclei. *Physical Review Letters*, 91(1), June 2003.

[61] A. Gade, P. Adrich, D. Bazin, M. Bowen, B. Brown, C. Campbell, J. Cook, S. Ettenauer, T. Glasmacher, K. Kemper, S. McDaniel, A. Obertelli, T. Otsuka, A. Ratkiewicz, K. Siwek, J. Terry, J. Tostevin, Y. Utsuno, and D. Weisshaar. Spectroscopy of ^{36}Mg: Interplay of Normal and Intruder Configurations at the Neutron-Rich Boundary of the Island of Inversion. *Physical Review Letters*, 99(7), August 2007.

[62] E. Simpson and J. Tostevin. Two-nucleon correlation effects in knockout reactions from ^{12}C. *Physical Review C*, 83(1), January 2011.

[63] G. Jacob and Th. A. J. Maris. Quasi-Free Scattering and Nuclear Structure. *Reviews of Modern Physics*, 38(1):121, 1966.

[64] O. Chamberlain and E. Segrè. Proton-Proton Collisions within Lithium Nuclei. *Physical Review*, 87(1):81–83, July 1952.

[65] P. Kitching, W. J. McDonald, Th. A. J. Maris, and Vasconcellos C. A. Z. Recent Developments in Quasi-free Nucleon-Nucleon Scattering. *Advances in Nuclear Physics*, 15:43, 1985.

[66] P. Wolff. The Scattering of Protons from Carbon. *Physical Review*, 87(3):434–438, August 1952.

[67] N. Chant and P. Roos. Distorted-wave impulse-approximation calculations for quasifree cluster knockout reactions. *Physical Review C*, 15(1):57–68, January 1977.

[68] C. Samanta and A. A. Cowley. Tests of the factorized distorted wave impulse approximation for $(p, 2p)$ reactions. *Physical Review C*, 34(5):1610–1619, November 1986.

[69] Th. A. J. Maris. Quasi-elastic scattering and nuclear structure. *Nuclear Physics*, 7:1–9, August 1958.

[70] G. Jacob. Quasi-free electron-proton scattering (II). *Nuclear Physics*, 31:152–156, April 1962.

[71] G. Jacob. Quasi-free electron-proton scattering (I). *Nuclear Physics*, 31:139–151, April 1962.

[72] U. Amaldi, G. Venuti, G. Cortellessa, C. Fronterotta, A. Reale, P. Salvadori, and P. Hillman. Inner-Shell Proton Binding Energies in ^{12}C and ^{27}Al from the $(e, e'p)$ Reaction using 550-MeV Electrons. *Physical Review Letters*, 13(10):341–343, September 1964.

[73] C. Devries, C. Dejager, L. Lapikas, G. Luijckx, R. Maas, H. Devries, and P. K. A. De Witt Huberts. The 500 MeV electron-scattering facility at NIKHEF-K. *Nuclear Instruments and Methods in Physics Research*, 223(1):1–25, June 1984.

[74] P. K. A. De Witt Huberts. Proton spectral functions and momentum distributions in nuclei from high-resolution $(e, e'p)$ experiments. *Journal of Physics G: Nuclear and Particle Physics*, 16(4):507, 1990.

[75] A. E. L. Dieperink and P. K. A. De Witt Huberts. On High Resolution $(e, e'p)$ Reactions. *Annual Review of Nuclear and Particle Science*, 40(1):239–284, December 1990.

[76] L. Lapikás. Quasi-elastic electron scattering off nuclei. *Nuclear Physics A*, 553:297–308, March 1993.

[77] W. Dickhoff and C. Barbieri. Progress in Particle and Nuclear Physics : Self-consistent Green's function method for nuclei and nuclear matter. *Progress in Particle and Nuclear Physics*, 52(2):377–496, April 2004.

[78] R. Shneor, P. Monaghan, R. Subedi, B. Anderson, K. Aniol, J. Annand, J. Arrington, H. Benaoum, F. Benmokhtar, P. Bertin, W. Bertozzi, W. Boeglin, J. Chen, Seonho Choi, E. Chudakov, E. Cisbani, B. Craver, C. de Jager, R. Feuerbach, S. Frullani, F. Garibaldi, O. Gayou, S. Gilad, R. Gilman, O. Glamazdin, J. Gomez, J.-O. Hansen, D. Higinbotham, T. Holmstrom, H. Ibrahim, R. Igarashi, E. Jans, X. Jiang, Y. Jiang, L. Kaufman, A. Kelleher, A. Kolarkar, E. Kuchina, G. Kumbartzki, J. LeRose, R. Lindgren, N. Liyanage, D. Margaziotis, P. Markowitz, S. Marrone, M. Mazouz, D. Meekins, R. Michaels, B. Moffit, S. Nanda, C. Perdrisat, E. Piasetzky, M. Potokar, V. Punjabi, Y. Qiang, J. Reinhold, B. Reitz, G. Ron, G. Rosner, A. Saha, B. Sawatzky, A. Shahinyan, S. Širca, K. Slifer, P. Solvignon, V. Sulkosky, N. Thompson, P. Ulmer, G. Urciuoli, E. Voutier, K. Wang, J. Watson, L. Weinstein, B. Wojtsekhowski, S. Wood, H. Yao, X. Zheng, and L. Zhu. Investigation of Proton-Proton Short-Range Correlations via the ^{12}C$(e, e'pp)$ Reaction. *Physical Review Letters*, 99(7), August 2007.

[79] E. Piasetzky. Short Range Correlations and Color Transparency. *Nuclear Physics A*, 827(1-4):85c–92c, August 2009.

[80] A.N. Antonov, M.K. Gaidarov, M.V. Ivanov, D.N. Kadrev, M. Aïche, G. Barreau, S. Czajkowski, B. Jurado, G. Belier, and A. Chatillon. The electron-ion scattering experiment ELISe at the International Facility for Antiproton and Ion Research (FAIR). *Nuclear Instruments and Methods in Physics Research Section A: Accelerators, Spectrometers, Detectors and Associated Equipment*, 637(1):76–60, February 2011.

[81] G. P. A. Berg, T. Adachi, M. N. Harakeh, N. Kalantar-Nayestanaki, H. J. Wörtche, H. Simon, I. A. Koop, M. Couder, and M. Fujiwara. A novel spectrometer for studying exotic nuclei with the electron/ion collider ELISe. *Nuclear Instruments and Methods in Physics Research Section A: Accelerators, Spectrometers, Detectors and Associated Equipment*, February 2011.

[82] J. Ryckebusch, W. Cosyn, and M. Vanhalst. Density dependence of quasifree single-nucleon knockout reactions. *Physical Review C*, 83(5), May 2011.

[83] T. Kobayashi, K. Ozeki, K. Watanabe, Y. Matsuda, Y. Seki, T. Shinohara, T. Miki, Y. Naoi, H. Otsu, S. Ishimoto, S. Suzuki, Y. Takahashi, and E. Takada. $(p, 2p)$ Reactions on $^{9-16}$C at 250 MeV/A. *Nuclear Physics A*, 805:431c–438c, 2008.

[84] L. Chulkov, F. Aksouh, A. Bleile, O. Bochkarev, D. Cortina-Gil, A. Dobrovolsky, P. Egelhof, H. Geissel, M. Hellstrom, N. Isaev, O. A. Kiselev, B. G. Komkov, M. Matos, F. N. Moroz, G. Munzenberg, M. Mutterer, V. A. Mylnikov, S. R. Neumaier, V. N. Pribora, M. D. Seliverstov, L. O. Sergeev, A. Shrivastava, K. Summerer, S. Yu. Torilov, H. Weick, M. Winkler, and V. I. Yatsoura. Quasifree scattering with 6-8He beams. *Nuclear Physics A*, 759(1-2):43–63, September 2005.

[85] S. Paschalis. *Relativistic One-Nucleon Removal Reactions*. PhD thesis, University of Liverpool, 2008.

[86] V. Metag, R. Fischer, W. Kuhn, R. Muhlhans, R. Novotny, D. Habs, U. Helmolt, H. Heyng, R. Kroth, and D. Pelte. Physics with 4π-γ-detectors. *Nuclear Physics A*, 409:331–342, November 1983.

[87] The LAND Collaboration, Th. Blaich, Th.W. Elze, H. Emling, H. Freiesleben, K. Grimm, W. Henning, R. Holzmann, G. Ickert, J.G. Keller, H. Klingler, W. Kneissl, R. König, R. Kulessa, J.V. Kratz, D. Lambrecht, J.S. Lange, Y. Leifels, E. Lubkiewicz, M. Proft, W. Prokopowicz, C. Schutter, R. Schmidt, H. Spies, K. Stelzer, J. Stroth, W. Walus, E. Wajda, H. J. Wollersheim, M. Zinser, and E. Zude. A large area detector for high-energy neutrons. *Nuclear Instruments and*

Methods in Physics Research Section A: Accelerators, Spectrometers, Detectors and Associated Equipment, 314(1):136–154, 1992.

[88] V. Bindi. The alpha magnetic spectrometer AMS-02: Soon in space. *Nuclear Instruments and Methods in Physics Research Section A: Accelerators, Spectrometers, Detectors and Associated Equipment*, 617(1-3):462–463, May 2010.

[89] P. Zuccon. The AMS silicon tracker: Construction and performance. *Nuclear Instruments and Methods in Physics Research Section A: Accelerators, Spectrometers, Detectors and Associated Equipment*, 596(1):74–78, October 2008.

[90] W. Burger. The Alpha Magnetic Spectrometer Silicon Tracker. *Nuclear Instruments and Methods in Physics Research Section A: Accelerators, Spectrometers, Detectors and Associated Equipment*, 435(1-2):202–214, October 1999.

[91] B. Alpat, G. Ambrosi, P. Azzarello, R. Battiston, P. Bene, B. Bertucci, S. Bizzaglia, M. Bizzarri, S. Blasko, and M. Bourquin. Charge determination of nuclei with the AMS-02 silicon tracker. *Nuclear Instruments and Methods in Physics Research Section A: Accelerators, Spectrometers, Detectors and Associated Equipment*, 540(1):121–130, 2005.

[92] B. Alpat. High-precision tracking and charge selection with silicon strip detectors for relativistic ions. *Nuclear Instruments and Methods in Physics Research Section A: Accelerators, Spectrometers, Detectors and Associated Equipment*, 446(3):522–535, May 2000.

[93] LAND Pictures: http://www-land.gsi.de/a_new_land/.

[94] C. Wimmer. Proton Tracking at the R3B Experiment. Technical report, GSI, 2007.

[95] J. Cub, G. Stengel, A. Grünschloß, K. Boretzky, T. Aumann, W. Dostal, B. Eberlein, Th.W Elze, H. Emling, G. Ickert, J. Holeczek, R Holzmann, J.V Kratz, R. Kulessa, Y. Leifels, H. Simon, K. Stelzer, J. Stroth, A. Surowiec, and E. Wajda. A large-area scintillating fibre detector for relativistic heavy ions. *Nuclear Instruments and Methods in Physics Research Section A: Accelerators, Spectrometers, Detectors and Associated Equipment*, 402(1):67–74, 1998.

[96] K. Mahata, H.T. Johansson, S. Paschalis, H. Simon, and T. Aumann. Position reconstruction in large-area scintillating fibre detectors. *Nuclear Instruments and Methods in Physics Research Section A: Accelerators, Spectrometers, Detectors and Associated Equipment*, 608(2):331–335, 2009.

[97] R. Plag. land02 - the unofficial guide: http://www-linux.gsi.de/~rplag/land02/index.php?page=detectors/ssd/.

[98] ROOT - A Data Analysis Framework: http://root.cern.ch/.

[99] H. Johansson. *The DAQ always runs.* PhD thesis, Chalmers University of Technology, 2006.

[100] M. Stanoiu. Fragment tracking with Si Microstrip detectors. Technical report, GSI, 2006.

[101] M. Menichelli, L. Accardo, G. Ambrosi, R. Battiston, M. Bizzarri, S. Blasko, D. Cosson, E.M. Fiori, O. Maris, and A. Papi. Construction and qualification of the Power Supply system of the AMS-02 Tracker detector. *Nuclear Physics B - Proceedings Supplements*, 166:234–240, April 2007.

[102] J. Hoffmann, N. Kurz, and W. Ott. SIDEREM2 Manual: http://www.gsi.de/informationen/wti/ee/elekt_entwicklung/siderem2_e.html, 2007.

[103] M. Stanoiu, K. Summerer, I. Mukha, A. Chatillon, E. Cortina Gil, M. Heil, J. Hoffman, OA Kiselev, N. Kurz, W. Ott, and Others. A novel Si strip array to investigate reaction and decay mechanisms. *Nuclear Instruments and Methods in Physics Research Section B: Beam Interactions with Materials and Atoms*, 266(19-20):4625–4627, 2008.

[104] B. Alpat. The AMS silicon tracker readout: performance results with minimum ionizing particles. *Nuclear Instruments and Methods in Physics Research Section A: Accelerators, Spectrometers, Detectors and Associated Equipment*, 439(1):53–64, January 2000.

[105] H. Spieler. *Semiconductor detector systems.* OUP Oxford, Oxford, 2005.

[106] E. Belau, R. Klanner, G. Lutz, E. Neugebauer, HJ Seebrunner, A. Wylie, T. Bohringer, L. Hubbeling, P. Weilhammer, J. Kemmer, and Others. Charge collection in silicon strip detectors. *Nuclear Instruments and Methods in Physics Research*, 214(2-3):253–260, 1983.

[107] GARFIELD - Simulation of gaseous detectors: http://garfield.web.cern.ch/garfield/.

[108] B. Martin and G. Shaw. *Particle Physics (Manchester Physics Series).* Wiley-Blackwell, 2008.

[109] D. Greiner, P. Lindstrom, H. Heckman, B. Cork, and F. Bieser. Momentum Distributions of Isotopes Produced by Fragmentation of Relativistic ^{12}C and ^{16}O Projectiles. *Physical Review Letters*, 35(3):152–155, July 1975.

[110] H. Weick. ATIMA: ATomic Interactions with MAtter http://www-linux.gsi.de/~weick/atima/.

[111] U. Datta Pramanik, T. Aumann, K. Boretzky, B. V. Carlson, D. Cortina, Th. W. Elze, H. Emling, H. Geissel, A. Grünschloß, and M. Hellström. Coulomb breakup of the neutron-rich isotopes ^{15}C and ^{17}C. *Physics Letters B*, 551(1-2):63–70, January 2003.

[112] F. Ajzenberg-Selove. Energy levels of light nuclei A = 11-12. *Nuclear Physics A*, 506(1):1–158, 1990.

[113] D. Rossi. Private Communication, 2011.

[114] K. Boretzky, A. Grünschloß, S. Ilievski, P. Adrich, T. Aumann, C. A. Bertulani, J. Cub, W. Dostal, B. Eberlein, Th. W. Elze, H. Emling, M. Fallot, J. Holeczek, R. Holzmann, C. Kozhuharov, J. V. Kratz, R. Kulessa, Y. Leifels, A. Leistenschneider, E. Lubkiewicz, S. Mordechai, T. Ohtsuki, P. Reiter, H. Simon, K. Stelzer, J. Stroth, K. Sümmerer, A. Surowiec, E. Wajda, and W. Walus. Two-phonon giant resonances in ^{136}Xe, ^{208}Pb, and ^{238}U. *Physical Review C*, 68(2), August 2003.

[115] J. Marganiec. Private Communication, 2011.

[116] R3BSim description and results: http://www.usc.es/genp/r3b/.

[117] D. Bertini, M. A-Turany, I. Koenig, and F. Uhlig. The FAIR simulation and analysis framework. *Journal of Physics: Conference Series*, 119(3):032011, July 2008.

[118] S. Agostinelli, J. Allison, K. Amako, J. Apostolakis, H. Araujo, P. Arce, M. Asai, D. Axen, S. Banerjee, G. Barrand, F. Behner, L. Bellagamba, J. Boudreau, L. Broglia, A. Brunengo, H. Burkhardt, S. Chauvie, J. Chuma, R. Chytracek, and G. Cooperman. GEANT4 - a simulation toolkit. *Nuclear Instruments and Methods in Physics Research Section A: Accelerators, Spectrometers, Detectors and Associated Equipment*, 506(3):250–303, 2003.

[119] D. Bertini. R3BRoot: a ROOT based Simulation and Analysis Framework for R3B. Technical report, GSI, 2009.

[120] A. S. Goldhaber. Statistical models of fragmentation processes. *Physics Letters B*, 53(4):306–308, 1974.

[121] P. Van Isacker, G. Auger, and C. Grosjean. Quantal versions of Goldhaber's fragmentation model. Technical report, GANIL, CAEN, 2002.

[122] G. Van Der Steenhoven, H. P. Blok, E. Jans, M. De Jong, L. Lapikás, E. N. M. Quint, and P. K. A. De Witt Huberts. Knockout of 1p protons from ^{12}C induced by the $(e, e'p)$ reaction. *Nuclear Physics A*, 480:547–572, 1988.

[123] H. Alvarez-Pol, J. Benlliure, E. Casarejos, D. Cortina, I. Durán, and M. Gascón. Design studies and first crystal tests for the R3B calorimeter. *Nuclear Instruments and Methods in Physics Research Section B: Beam Interactions with Materials and Atoms*, 266(19-20):4616–4620, 2008.

[124] Y. Yasuda, H. Sakaguchi, S. Asaji, K. Fujita, Y. Hagihara, K. Hatanaka, T. Ishida, M. Itoh, T. Kawabata, S. Kishi, T. Noro, Y. Sakemi, Y. Shimizu, H. Takeda, Y. Tameshige, S. Terashima, M. Uchida, T. Wakasa, T. Yonemura, H. P. Yoshida, M. Yosoi, and J. Zenihiro. Spectroscopic factors and strength distributions for the deeply bound orbitals in ^{40}Ca obtained from the $(p, 2p)$ reaction at 392 MeV. *Phys. Rev. C 81*, 81:044315, January 2010.

[125] M. Yosoi. *Structures and fragmentations of the deep-hole states in ^{11}B and ^{15}N*. PhD thesis, Kyoto University, 2003.

[126] Y. Shimizu, T. Kobayashi, T. Kubo, N. Chiga, T. Isobe, T. Kawabata, Y. Kondo, K. Kusaka, Y. Matsuda, T. Motobayashi, T. Murakami, T. Nakamura, J. Ohnishi, T. Ohnishi, H. Okuno, H. Otsu, H. Sakurai, H. Sato, Y. Satou, K. Sekiguchi, Y. Togano, and K. Yoneda. SAMURAI Project at RIBF. *Journal of Physics: Conference Series*, 312(5):052022, September 2011.

[127] J. Mougey, M. Bernheim, A. Bussière, A. Gillebert, Phan Xuan Hô, M. Priou, D. Royer, I. Sick, and G. J. Wagner. Quasi-free $(e, e'p)$ scattering on ^{12}C, ^{28}Si, ^{40}Ca and ^{58}Ni. *Nuclear Physics A*, 262(3):461–492, 1976.

[128] T. Noro, T. Baba, K. Hatanaka, M. Ito, M. Kawabata, N. Matsuoka, Y. Mizuno, S. Morinobu, M. Nakamura, A. Okihana, K. Sagara, H. Sakaguchi, K. Takahisa, H. Takeda, A. Tamii, K. Tamura, M. Tanaka, S. Toyama, H. Yamazaki, Y. Yuasa, and Et Al. A study of nucleon properties in nuclei through $(p, 2p)$ reactions. *Nuclear Physics A*, 629:324–333, 1998.

[129] A. N. James, W. J. McDonald, J. M. Cameron, C. A. Miller, D. A. Hutcheon, P. Kitching, G. C. Neilson, G. M. Stinson, and E. D. Earle. Quasi-free collisions of 400 MeV protons in deuterium and carbon. *Nuclear Physics A*, 324:253–265, 1979.

[130] G. Van Der Steenhoven, H. P. Blok, E. Jans, L. Lapikás, E. N. M. Quint, and P. K. A. De Witt Huberts. Weak transitions in the quasi-elastic reaction $^{12}C(e, e'p)^{11}B$. *Nuclear Physics A*, 484:445–475, 1988.

[131] J. M. Kidd, P. J. Lindstrom, H. J. Crawford, and G. Woods. Fragmentation of carbon ions at 250 MeV/nucleon. *Physical Review C*, 37(6):2613, 1988.

[132] T. Aumann and A. Kelic-Heil. Private Communication, 2011.

[133] K. Hencken, G. Bertsch, and H. Esbensen. Breakup reactions of the halo nuclei ^{11}Be and ^{8}B. *Physical Review C*, 54(6):3043, 1996.

[134] G.F. Bertsch, K. Hencken, and H. Esbensen. Nuclear breakup of Borromean nuclei. *Physical Review C*, 57(3):1366, 1998.

[135] B. Brown, P. Hansen, B. Sherrill, and J. Tostevin. Absolute spectroscopic factors from nuclear knockout reactions. *Physical Review C*, 65(6):061601, May 2002.

[136] T. J. Gooding and H. G. Pugh. Quasi-elastic scattering of 153 MeV protons by p-state protons in C^{12}. *Nuclear Physics*, 18:46–64, 1960.